UNIVERSITY OF CALIFORNIA

Santa Barbara

Molecular Beam Epitaxy for New Generation Nitride Devices

A dissertation submitted in partial satisfaction of the

requirements for the degree of

Doctor of Philosophy

in

Electrical and Computer Engineering

By

Christian D. Wurm

Committee in charge:

Professor Umesh K. Mishra, Chair

Professor Steven P. DenBaars

Professor Shuji Nakamura

Professor James S. Speck

Dr. Stacia Keller

June 2022

This thesis of Christian D. Wurm is approved:

Dr. Stacia Keller

Prof. James S. Speck

Prof. Shuji Nakamura

Prof. Steven P. DenBaars

Prof. Umesh K. Mishra, chair

June 2022

Molecular Beam Epitaxy for New Generation Nitride Devices

By

Christian D. Wurm

“ ….I can offer you nothing except hunger, thirst, privation…..”

Subhas Chandra Bose, 1943

Acknowledgments

First and foremost, I would like to thank my loving wife, Aidee Sarabia Wurm, and my daughter Fredell Wurm, who's love and support made this work possible. I would also like to thank my parents, Mike and Sandy Wurm and other members of my family for supporting me on this journey.

I am especially grateful to my PhD advisor Prof. Umesh K. Mishra for giving me the opportunity to join his group and for all that I have learned from him. I am also grateful to Dr. Paul Maki from the Office of Naval Research for funding my research at UCSB. The people of the Mishra group at UCSB have been an invaluable source of information for all things related to GaN growth and technology. I would like to thank Prof. Elaheh Ahmadi for having the time and patience to teach me PAMBE growth; Dr. Stacia Keller for being an invaluable source of information on all things related to epitaxial growth of nitride semiconductors; and all the other people in the Mishra group including and not limited to Dr. Brian Romanczyk, Dr. Nirupam Hatui, Dr. Wenjian Liu, Dr. Xun Zheng, Dr. Cory Lund, Dr. Anchal Agarwal, Dr. Mathew Guidry, Dr. Onur Koksaldi, Dr. Steven Wienecke, Prof. Chirag Gupta, Prof. Shubhra Pasayat, Athith Krishna, Dr. Pawana Shrestha, Weiyi Li, Aditya Raj, Robert Hamwey, Boyu Wang, Christopher Claymore, Emre Akso, Henry Collins and Vineeta Mithuraj.

I would also like to thank those I have worked with in the MBE lab at UCSB: Dr. Kelsey Jorgensen, Ashley Wissel, Zach Biegler, Clayton Kwah, Wan Ying Ho, Dr. Richard Cramer, John English, Dr. Erin Young, Dr. Christian Robertson, Dr. Jianfeng Wang, and Kurt Olson. I am also indebted to my collaborators at the University of Michigan including Kai Sun, for all his help and knowledge on TEM analysis, and of course Kamruzzaman Khan.

The world class laboratories at UCSB have been an essential element to my success and therefor I must express my gratitude for Brian Thibeault and all of the other member of the UCSB Nanofab. I am also thankful to the staff at the California Nano Systems Institute (CNSI) and especially Dr. Tom Mates. I am also grateful for Dr. Youli li and Miguel Zepeda for running the UCSB X-ray diffraction laboratory.

I am also indebted to my former colleagues and professors as UC San Diego who helped prepare me for UCSB. I am extremely grateful for Prof. Shaya Fainman for employing me in his group; Prof. Yuan Taur and Prof. Shadi Dayeh, for always taking the time to talk to me outside of class and for teaching me so much. I am especially grateful for Prof. S. S. Lau

for all that he taught me and for pushing me to better understand semiconductor physics. I am also grateful for my fellow colleagues at UC San Diego including Dr. Hung-His Lin, Dr. Felipe Vallini, Dr. Rajat Sharma, Dr. Abdelkrim Al Amili, Dr. Shiva Shahin, Dr. Jordan Davis, Dr. Suruj Deka, Dr. Atsunori Tanaka and Dr. Namseok Park.

Finally, I would like to express my sincere gratitude for the remaining members of my committee: Prof. James Speck, Prof. Shuji Nakamura, and Prof. Steve DenBaars for being a source of knowledge and inspiration, and for helping shape the nitride semiconductor field into what it is today.

Curriculum Vitae

Christian D. Wurm

Education

- **University of California Santa Barbara** (2019-2022)
  PhD in Electrical and Computer Engineering with an emphasis on electronics and photonics

- **University of California Santa Barbara** (2017-2019)
  Master of Science Degree in Electrical and Computer Engineering with an emphasis on electronics and photonics

- **University of California San Diego** (2014-2017)
  Bachelors Degree in Electrical and Computer Engineering with an emphasis on devices and materials

Professional Experience

- **University of California Santa Barbara** (2017-2022)
  Advisor: Umesh K. Mishra

  Graduate student researcher

- **Ultrafast and Nanoscale Optics group at UC San Diego** (2014-2017)
  Advisor: Prof. Shaya Fainman

  Student researcher

- **San Diego Mesa Community College** (2012-2014)
  Math, physics, chemistry, and Chinese tutor

- **FieldLogix** (2008-2012)
  Field Service Specialist, operations representative, technical Support Representative

- **Syndicate Automotive Concepts** (2005-2007)
  Installer/Fabricator: Car audio, security, navigation and video installation, custom interior fabrication

- **Al and Ed's Autosound** (2004-2005)
  Installer, Install Bay Manager

Journal publications

C. Wurm, H. Collins, N. Hatui, W. Li, S. Pasayat, R. Hamwey, K. Sun, I. Sayed, K. Khan, E. Ahmadi, S. Keller, U. K. Mishra, "Demonstration of device-quality 60% relaxed $In_{0.2}Ga_{0.8}N$ on porous GaN pseudo-substrates grown by PAMBE," J. Appl. Phys., vol. 131, no. 1, p. 015701, (2022)

C. Wurm, E. Ahmadi, F. Wu, N. Hatui, S. Keller, J. Speck, U. Mishra. "Growth of high-quality N-polar GaN on bulk GaN by plasma-assisted molecular beam epitaxy," Jour. Solid State Comm., (2020)

C. Wurm, Growth of high-quality N-polar (000-1) "GaN on bulk GaN by plasma-assisted molecular beam epitaxy," Master's Thesis (2019)

K. Khan, S. Diez, K. Sun, **C. Wurm**, U. K. Mishra, and E. Ahmadi, "Observation of self-assembled InGaN/GaN superlattice structure grown on N-polar GaN by plasma-assisted molecular beam epitaxy," APL Mater., vol. 9, no. 12, p. 121114, (2021)

Wenjian Liu, Brian Romanczyk, Matthew Guidry, Nirupam Hatui, **Christian Wurm**, Weiyi Li, Pawana Shrestha, Xun Zheng, Stacia Keller, Umesh K Mishra. "6.2 W/mm and Record 33.8% PAE at 94 GHz from N-polar GaN Deep Recess MIS-HEMTs with ALD Ru Gates," IEEE Microwave and Wireless Components Letters (2021)

Brian Romanczyk, Weiyi Li, Matthew Guidry, Nirupam Hatui, Athith Krishna, **Christian Wurm**, Stacia Keller, Umesh K Mishra. "N-polar GaN-on-Sapphire Deep Recess HEMTs With High W-Band Power Density," IEEE Electron Device Letters (2020)

P. Shrestha, M. Guidry, B. Romanczyk, N. Hatui, **C. Wurm**, A. Krishna, S. S. Pasayat, R. R. Karnaty, S. Keller, J. F. Buckwalter, U. K Mishra. "High Linearity and High Gain Performance of N-Polar GaN MIS-HEMT at 30 GHz," IEEE Electron Device Letters (2020)

B. Romanczyk, X. Zheng, M. Guidry, H. Li, N. Hatui, **C. Wurm**, A. Krishna, E. Ahmadi, S. Keller, U. K. Mishra. "W-Band Power Performance of SiN-Passivated N-Polar GaN Deep Recess HEMTs," IEEE Electron Device Letters (2020)

C. Lund, M. Catalano, L. Wang, **C. Wurm**, T. Mates, M. Kim, S. Nakamura, S. DenBaars, U. Mishra, S. Keller. "Metal-organic chemical vapor deposition of N-polar InN quantum dots and thin films on vicinal GaN," Applied Physics Letters (2018)

S. S. Pasayat, E. Ahmadi, B. Romanczyk, O. Koksaldi, A. Agarwal, M. Guidry, C. Gupta, **C. Wurm**, S. Keller and U.K. Mishra. "First demonstration of RF N-polar GaN HEMTs grown on Bulk GaN using PAMBE," Semiconductor Science and Technology (2018)

H.H. Lin, F. Vallini, M.H. Yang, R. Sharma, M. Puckett, S. Montoya, **C. Wurm**, E. Fullerton

& Y. Fainman. “Electronic Metamaterials with Tunable Second-order Optical Nonlinearities,” Scientific Reports, (2017)

H.H. Lin, M.H. Yang, R. Sharma, M. Puckett, S. Montoya, **C. Wurm**, F. Vallini, E. Fullerton, Y. Fainman. “Synthesis of Second-order Nonlinearities in Dielectric-Semiconductor-Dielectric Metamaterials,” Applied Physics Letters, (2016)

Conference Presentations

C. Wurm, H. Collins, N. Hatui, W. Li, S. Pasayat, R. Hamwey, K. Sun, I. Sayed, K. Khan, E. Ahmadi, S. Keller, U. K. Mishra, “Demonstration of device-quality InGaN grown on porous GaN tiles by MBE with an in-plane lattice constant equivalent to fully relaxed $In_{0.12}Ga_{0.88}N$,” Compound Semiconductor Week (2022)

C. Wurm, E. Ahmadi, F. Wu, N. Hatui, S. Keller, J. Speck, U. Mishra. “Growth of high-quality N-polar GaN on bulk GaN by plasma-assisted molecular beam epitaxy,” Int. Conf. of Nitride Semic., (2019)

Pawana Shrestha, Matthew Guidry, Brian Romanczyk, Rohit R Karnaty, Nirupam Hatui, **Christian Wurm**, Athith Krishna, Shubhra S Pasayat, Stacia Keller, James F Buckwalter, Umesh K Mishra. “A Novel Concept using derivative superposition at the device-level to reduce linearity sensitivity to bias in N-polar GaN MISHEMT” 2020 Device Research Conference (2020)

R. R. Karnaty, M. Guidry, P. Shrestha, B. Romanczyk, N. Hatui, X. Zheng, **C. Wurm**, H. Li, S. Keller, U. K. Mishra, J. F. Buckwalter. “Virtual-Source Modeling of N-polar GaN MISHEMTS” IEEE BiCMOS and Compound semiconductor Integrated Circuits and Technology Symposium (BCICTS) (2020)

H.H. Lin, R. Sharma, M.H. Yang, M. Puckett, **C. Wurm**, F. Vallini, and Y. Fainman “Enhanced Effective Second-order Nonlinearities in Si-rich SiNx Thin Films” CLEO Conference, (2017)

H.H. Lin, M.H. Yang, R. Sharma, M.Puckett, S. Montoya, **C. Wurm**, F. Vallini, E. Fullerton, Y. Fainman. “Engineering of Second-Order Nonlinearity in Silicon-dielectric Multilayers” CLEO Conference, (2016)

Abstract

Molecular Beam Epitaxy for New Generation Nitride Devices

by

Christian D. Wurm

Although MOCVD is regarded as the preferred growth method for commercial grade nitride-based semiconductor devices, there are still certain applications for which MBE may be utilized. Current record-performing N-polar HEMTs are grown by MOCVD which must use miscut SiC and sapphire substrates. The growth conditions employed by MBE, however, enable growth of N-polar GaN on non-vicinal substrates. MOCVD grown GaN-on-SiC N-polar HEMTs typically have a threading dislocation density on the order of 10^8 cm^{-2}.

Amplifiers biased in class-A mode operate at a high source-to-drain quiescent current. High current in a material with a high density of scattering centers (such as dislocations) may lead to power dissipation in the form of heat which can impede device efficiency. MBE grown N-polar HEMT epi-structures on low dislocation density bulk GaN substrates may improve this efficiency. Furthermore, the low temperature growth used by

MBE enables thicker coherently strained AlN interlayers, or back-barriers, which can mitigate the effects of alloy scattering in the 2DEG channel. Although N-polar GaN grown on bulk GaN by MBE typically results in a surface riddled with V-defects, this work demonstrates suppression of V-defects by initiating growth with just 2 nm of AlN. It was shown that the generation of these pits may be attributed to impurities on the regrowth interface.

InGaN grown by MBE has the advantage of growing thick layers without generating V-defects on the surface. Furthermore, the lower growth temperatures employed by MBE enable extremely high In-mole fraction InGaN. This is advantageous for growing thick, relaxed InGaN on compliant substrates for long-wavelength nitride-based optoelectronics. The simplicity of MBE, which does not use any metal-organic precursors or carrier gases, makes it suitable for proof-of-concept next generation devices.

Composition pulling and Quantum Confined Stark Effect (QCSE) has severely limited nitride-based red LEDs to achieve the efficiencies shared by their blue and green counterparts. MOCVD grown elastically relaxed InGaN on porous GaN tiles have shown significant progress however they are limited due to the high density of V-defects on the surface. This work demonstrates MBE grown InGaN on porous GaN tiles with a surface free of V-defects which had an in-plane lattice constant equivalent to fully relaxed $In_{0.12}Ga_{0.88}N$. STEM analysis revealed no new dislocations in the InGaN layer demonstrating the compliant nature of the porous tile. This is a significant improvement from previous work by MOCVD. These MBE grown tiled pseudo-substrates may be a compelling technology for micro-LED displays.

Table of Contents

NC)Acknowledgments ..... *v*

Curriculum Vitae ..... *vii*

Abstract ..... *x*

Table of Contents ..... *xii*

List of Figures ..... *xv*

List of Tables ..... *xx*

List of Symbols and Acronyms ..... *xxi*

1 Introduction *1*

1.1 Gallium Nitride and Polarization Doping 3

1.2 Strained Heterostructures 4

1.3 High Electron Mobility Transistors (HEMTs) 5

1.4 PAMBE GaN Growth 6

1.5 Dislocation Mediated Spiral Growth 8

1.6 V-Defects 10

1.7 Conclusion 11

2 Growth of High-Quality N-polar GaN on Bulk GaN by PAMBE *13*

2.1 Motivation for Bulk GaN Substrates 14

2.2 Motivation for MBE 17

2.3 Past Work of PAMBE grown N-polar GaN on Bulk GaN 17

2.4 Summary of Study 18

2.5 Experimental Procedure 18

2.6 Effects of UV ozone clean (NA) 21

2.7 AIL: AlN initiation layer (NB) 23

2.8 AIL Thickness Study (NC) 28

2.9 Carbon Doping (ND) 31

2.10 Conclusion 33
3 Introduction to PAMBE Grown InGaN 34
3.1 Low Temperature Growth 35
3.2 Phase Separation 36
3.3 Plastic Relaxation 40
3.4 PAMBE Growth of InGaN 46
3.5 Growth Temperature and In-Composition 48
3.6 Conclusion 49
4 PAMBE InGaN Growth on Planar GaN 51
4.1 Introduction 51
4.2 Experimental Details 52
4.3 In-Flux Study (IA) 53
4.4 Ga-Flux Study (IB) 57
4.5 Temperature Controlled In-composition (IC) 61
4.6 Film quality and Relaxation (ID/IE) 66
4.7 Cross Hatching 71
4.8 Conclusion 73
5 Relaxed InGaN Substrates for Longer Wavelength micro-LEDs 75
5.1 Introduction 75
5.2 Red LED Literature Survey 76
5.3 Composition Pulling Effect 77
5.4 Quantum Confined Stark Effect 77
5.5 Relaxed InGaN Literature Survey 79
5.6 Porous GaN Tiles 81
5.7 Relaxation on Porous GaN tiles 84
5.8 Conclusion 85
6 PAMBE InGaN Growth on Porous GaN Tiles (PS) 87
6.1 Experimental Details 88

6.2 InGaN Grown at T_c = 550 C° (PA) 92
6.3 InGaN Grown at T_c = 530 C° (PB) 97
6.4 In-Composition Step Grade (PC & PD) 103
6.5 16% $x_{In,equiv.}$ Ceiling 117
6.6 Conclusion 119
7 Conclusion & Future Work 120
7.1 PAMBE for High-Frequency Power Amplifiers 121
7.2 PAMBE for Optoelectronics..... 121

Apendices……129

A.1: InGaN Composition Repeatability..... 125
A. 2: Sidewall Growth on PS Using Ultra-Low Growth Temperatures 127
A. 3: AlN Homoepitaxy Study 129
A. 4: N-polar InN Growth on Vicinal GaN-on-Sapphire Templates..... 133
A. 5: Mg doping Using Titan Valved Effusion Cell 134
References……140

List of Figures

Figure 1-1: Projected GaN market in the U.S. spanning from 2020 to 2030 conducted by Grand View Research. Reprinted from [1]. 2
Figure 1-2: Wurtzite GaN unit cell showing polarization charges for N-polar (top) and Ga-polar (bottom). Reprinted with permission from [4]. 4
Figure 2-1: (a) AFM micrograph for sample NA1, (b) AFM micrograph for sample NA2 which was subjected to a UV-ozone clean prior to growth. Surface RMS extracted from these AFMS were found to be 12.2 nm and 1.41 nm for NA1 and NA2 respectively. Reprinted with permission from [59], Copyright Elsevier 2020. 22
Figure 2-2: SIMS results for 400 nm of GaN grown directly on a N-polar free-standing (FS) GaN substrate (a) which was only subjected to a standard solvent clean and (b) one which was subjected to the 3x UV-ozone treatment as described in section 2.6. 23
Figure 2-3: NB-series AFM micrographs with corresponding structures below for (a) NB1, (b) NB2 and (c) NB3. Reprinted with permission from [58], Copyright Elsevier 2020. 25
Figure 2-4: (a) HRTEM image taken for NB1 at the AIL. Cross-section direction is (11-20). (b) TEM images and CBED patterns for NB2 showing both the simulated and experimental patterns for above and below the AIL. TEM analysis done by Dr. Feng Wu of the Jim Speck Group at UCSB. Reprinted with permission from [58], Copyright Elsevier 26
Figure 2-5: AFMs (right) along with corresponding sample structures (left) for (a) Ga-polar MOCVD grown GaN-on-sapphire template, (b) after 5 minutes in KOH, (c) 100 nm N-polar GaN grown by PAMBE on N-polar bulk GaN using the AIL and (d) after 5 minutes in KOH. Reprinted with permission from [8]. 27
Figure 2-6: AFM scans taken for (a) NC1, 2 nm AIL, (b) NC2, 4 nm AIL, (c) NC3, 6 nm AIL, and (d) NC4, 8 nm AIL. RMS values extracted from AFM for ND1, ND2, ND3 and ND4 were found to be 0.50 nm, 0.51 nm, 0.21 nm and 0.56 nm respectively (e) XRD ω-scan FWHM values plotted as a function of AIL thickness with the blue circles representing FWHM values taken from the (0002) reflection and brown squares taken from the 2021 reflection. Reprinted with permission from [59], Copyright Elsevier 2020. 29
Figure 2-7: XRD RSM scan taken near the $\{10\bar{1}5\}$ reflection for sample NC4 which was grown using the 8 nm AIL. Reprinted with permission from [58], Copyright Elsevier 2020. 30
Figure 2-8: AFM scans taken for 200 nm GaN:C with carbon concentrations of (a) 5.3×10^{19} cm^{-3} for ND1 (b) 2.5×10^{20} cm^{-3} for ND2 and (c) $8.3 \times 1020\ \mathrm{cm} - 3$ for ND3. Reprinted with permission from [59], Copyright Elsevier 2020. 32
Figure 3-1: Temperature vs. In-composition phase diagram of ternary c-plane InGaN compounds for different values of relaxation. Reprinted with permission from [95], copyright American Physical Society (2011). 38
Figure 3-2: Illustration showing how a pre-existing threading dislocation segment in the substrate will extend along the growth interface (glide) aided by the force from the energy of the strained layer. The Peierls force and line tension of the dislocation oppose this force. 42

Figure 3-3: Punch out effect for InGaN grown on GaN where the secondary slip system $\{11\bar{2}2\}\langle 11\bar{2}3\rangle$ is activated from plastic deformation leading to a displaced section of the InGaN layer. Adapted from reference [125]. 45
Figure 3-4: Al-composition extracted from (0002) ω-2θ XRD scans for approximately 30 nm of AlGaN grown on GaN templates with varying Al flux by PAMBE under typical GaN growth conditions (growth conditions shown in inset). A clear linear trend is observed for Al-composition as a function of Al-flux. 48
Figure 3-5: Surface structure diagram indicating the N-rich, intermediate, and In-droplet growth regimes for InGaN using a constant Ga and active N-flux. In-flux is given by the solid curved line, active N-flux is given by the dotted black line and Ga-flux is given by the solid thin black line. This plot is adapted from Poblenz, (2005) [127]..... 48
Figure 4-1: Plot of In-composition as a function of In-flux for four growths. Top left inset shows (0002) ω-2θ XRD scans for each sample where InGaN composition was extracted. Bottom right inset displays the substrate temp and Ga-flux (BEP_{Ga}) which were kept constant across the four growths. 54
Figure 4-2: AFM micrographs taken for samples (a) IA1, BEP_{In} = 7.25e-7 torr leading to $In_{0.072}Ga_{0.0928}N$ grown in the In-rich regime. The white dots on the surface are likely to be In-droplets. (b) IA2, BEP_{In} = 6.16e-7 torr leading to $In_{0.047}Ga_{0.0953}N$ grown under slightly N-rich conditions leading to a pitted surface. (c) IA3, BEP_{In} = 4.63e-7 torr leading to low temperature GaN grown under N-rich conditions with excess In on the surface acting as a surfactant. (d) IA4, BEP_{In} = 2.87e-7 torr leading to N-rich GaN growth with rough surface morphology. 55
Figure 4-3: Surface structure diagram showing the estimated location of IA(1-4)..... 57
Figure 4-4: Plot of experimental data for the IB1-5 series showing growth rate (left vertical axis in red) and In-composition (right vertical axis in blue) as a function of Ga-flux. 59
Figure 4-5: AFM height scans for (a) IB1, where BEP_{Ga} = 2.86e-8 torr, t_{InGaN} ~ 88 nm, GR ~ 0.49 nm/min, (b) IB3, where BEP_{Ga} = 4.76e-8 torr, t_{InGaN} ~ 36 nm and GR ~ 0.9 nm/min, and (c) IB5, where BEP_{Ga} =7.12e-8 torr, t_{InGaN} = 58 nm, GR~1.45 nm/min. RMS vales extracted from these scans were found to be 0.253 nm, 0.55 nm and 1.05 nm for IA1, IA3 and IA5 respectively. 60
Figure 4-6: AFM scans for (a) IC1 grown at 540 ℃, (b) IC2 grown at 550 ℃, (c) IC3 grown at 560 ℃, (d) IC4 grown at 570 ℃. RMS values for samples IC1-4 were 0.6 nm, 0.7 nm, 0.58 nm and 0.57 nm respectively. 63
Figure 4-7: Plot of In-composition as a function of substrate temperature for the IC1-4 series along with other InGaN calibration growths done under different N-equivalent growth rates. The bottom left inset shows the (0002) $\omega - 2\theta$ XRD scans for the IC growth series for which In-composition was extracted from. 65
Figure 4-8: $(1\bar{1}\bar{1}24)$ XRD RSM scans for (a) ID1, 45 nm InGaN grown at 530 ℃, (b) ID2, 180 nm InGaN grown at 530 ℃, (c) ID3, 225 nm InGaN grown at 530 ℃, (d) IE1, 45 nm InGaN grown at 550 ℃, (e) IE2, 180 nm InGaN grown at 550 ℃ and (f) IE3, 225 nm InGaN grown at 550 ℃. The vertical dotted line segment running from the center of the GaN peak (top peak) down, is the fully strained line. The angled dotted line segment running from the GaN peak is the fully relaxed line. 68

Figure 4-9: AFM micrographs for (a) ID1, 45 nm InGaN grown at 530 ℃, (b) ID3, 225 nm InGaN grown at 530 ℃, (c) IE1, 45 nm InGaN grown at 550 $℃$, (d) IE3, 225 nm InGaN grown at 550 $℃$. RMS values extracted from AFMs were found to be 1.1 nm, 1.56 nm, 1.13 nm, and 2.03 nm for ID1, ID3, IE1, and IE3 respectively. 69
Figure 4-10: Plot of (a) (0002) $\omega - scan$ FWHM of the InGaN (in arcseconds) as a function of film thickness for the ID series (growth at 530 ℃) and IE series (growth at 550 $℃$) and (b) relaxation as a function of film thickness extracted from RSMs in Fig. 4-8. For both plots red diamond data points represent ID series (growth at 530 $℃$) and the dark blue circle data points represent the IE series (growth at 550 $℃$). 69
Figure 4-11: (a) AFM image of IF1 which had an RMS value of approximately 1 nm. (b) ($\bar{1}\bar{1}24$) XRD RSM scan for IF1 which showed approximately 6% relaxation. 72
Figure 5-1: Illustration of the quantum confined stark effect (QCSE). Band bending in the InGaN quantum well due to the large strain-induced piezoelectric charge at the two heterointerfaces leads to separation of the electron-hole wave function which reduces radiative recombination. 78
Figure 5-2: Maximum IQE as a function of emission wavelength showing the effects of alloy fluctuations and QCSE. Reprinted with permission from [147] with data also taken from Schiavon et al., [148]. Copyright American Physical Society. 79
Figure 5-3: Process flow for obtaining high-quality relaxed InGaN on PS. Starting from top left, MOCVD growth of 800 nm GaN:Si/100 nm GaN:UID on GaN-on-sapphire templates; top right, patterning and etching of 10x10 $\mu m2$ tiles; bottom right, porosification of tiles by electro-chemical (EC) etch; and bottom left, MBE regrowth of UID GaN and InGaN resulting in bi-axial relaxation. Reprinted with permission from [165]. Copyright AIP Publishing. 82
Figure 5-4: Diagram illustrating the EC etch setup used for Porosification. (b) band diagram showing the generation of holes at the GaN:Si/electrolyte interface which leads to oxidation at the surface and subsequent etching of the oxide by the electrolyte. 83
Figure 5-5: (a) FIB SEM cross-section showing the tile after Porosification, (b) close up of tile edge showing fingerlike pores and (c) a schematic showing the proposed EC etching of a nanopore which results in the observed finger-like pore, also described in reference [173]. 84
Figure 6-1: 1124 XRD RSM scans taken for InGaN growth at Tc = 550 ℃ for (a) PA1A (80 nm InGaN grown on planar GaN), (b) PA1 (80 nm InGaN on PS), (c) IE3 (225 nm InGaN on planar GaN) and (d) PA2 (225 nm InGaN on PS). Cooresponding sample structures are shown to the left of the RSMs and the substrate is indicated above the top two RSMs. Extracted In-compositions for PA1, PA1A, PA2 and IE3 were found to be 13.5%, 7.8%, 19.8% and 9.2% respectively. Extracted relaxation values for PA1A, PA1, IE3 and PA2 were found to be 7%, 36.4%, 8% and 80% respectively. 94
Figure 6-2: AFM micrographs taken for InGaN growth at Tc = 550 ℃ for (a) PA1A (80 nm InGaN grown on planar GaN),(b) PA1 (80 nm InGaN on PS), (c) IE3 (225 nm InGaN on planar GaN) and (d) PA2 (225 nm InGaN on PS). Cooresponding sample structures are shown to the left of the AFMs and the substrate is indicated above the top two AFMs. Surface RMS values for PA1A, PA1, IE3 and PA2 were found to be 1.46, 1.05, 2.03 and 5 nm respectively. 96

Figure 6-3: $11\bar{2}4$ XRD RSM scans taken for (a) PB1A (60 nm InGaN grown on planar GaN), (b) PB1 (60 nm InGaN on PS), (c) PB2 (120 nm InGaN grown on PS) and (d) PB3 (60 nm InGaN grown on PB1 with a GaN IL). RSM color scale bar is shown on the far right. Corresponding sample structures are shown to the left of each RSM. In-composition extracted from these RSMs were found to be 11.6%, 17%, 20.3% and 18.3% for PB1A, PB1, PB2 and PB3 respectively. Extracted relaxation values for PB1A, PB1, PB2 and PB3 were found to be 0 (fully strained), 13%, 60% and 50% respectively. 99
Figure 6-4: AFM micrographs for (a) PB1A, 60 nm InGaN grown on planar GaN, (b) PB1, 60 nm InGaN on PS, (c) PB2, 120 nm InGaN on PS and (d) PB3, 60 nm InGaN grown on PB1 (net InGaN thickness of 120 nm with GaN IL). Cooresponding sample structures are shown to the left of each AFM image. RMS values extracted from these AFMs were fround to be 0.796 nm, 1.167 nm, 2.038 nm and 1.515 nm for PB1A, PB1, PB2 and PB3 respectively. 100
Figure 6-5: RT PL spectras using a 325 nm laser showing (a) PB2, 120 nm InGaN on PS (solid black curve); PB3, 60 nm InGaN grown on PB1 with a GaN IL (120 nm InGaN total – dotted black curve); and the peak from a standard MOCVD grown GaN template (blue curve). (b) close up of the PB2 and PB3 peaks. The PB2 peak is at approximatly 415 nm and the PB3 peak is at approximatly 405 nm..... 101
Figure 6-6: cross-section dark-field STEM images take one the $[11\bar{2}0]$ zone axis for (a) sample PB3 (60 nm InGaN on PB1) and (b) sample PB2 (120 nm InGaN on PS) with corresponding sample structures to the left of each STEM image. STEM analysis done by Dr. Kai Sun at the University of Michigan. 102
Figure 6-7: $11\bar{2}4$ XRD RSM scans taken for (a) PC1A (planar) (b) PC1 (PS), (c) PC2A (planar) (d) PC2 (PS), (e) PC3A (planar) and (f) PC3 (PS). RSM color scale baris shown on the far right. Cooresponding sample structures are shown on the left. Extracted relaxation and In-composition values are shown in table 6-1. 107
Figure 6-8: AFM micrographs for the temperature controlled In-composition step-grade on (a) PC3A (planar GaN), (b) PC3 (PS). RMS vales extracted from these scans were found to be 1.55 nm and 1.43 nm for PC3A and PC3 respectively. 108
Figure 6-9: AFM micrographs for PC3 (temp controlled In-composition step-grade on PS) showing two V-defects in the bottom region of the image, and (b) 5000x magnification SEM image taken of the tiles showing multiple V-defects across multiple tiles. 109
Figure 6-10: $11\bar{2}4$ XRD RSM scans taken for (a) PD1A (step grade on planar) (b) PD1 (step grade on PS). RSM color scale bar is shown on the far right. Sample structures shown on the left. Extracted relaxation and In-composition values are shown in table 6-1. 111
Figure 6-11: AFM micrographs for the temperature controlled In-composition step-grade grown in a single run for (a) PD1A (step-grade on planar) and (b) PD1 (step-grade on PS). RMS values extracted from these scans were found to be 1.84 nm and 2.48 nm for PD1A and PD1 respectively. 112
Figure 6-12: Surface RMS values extracted from AFMs as a function of (a) x_{In} (red diamond data points) and relaxation (blue circle data points), (b) $x_{In,equiv.}$ and (c) InGaN net thickness. 112
Figure 6-13: 8000x magnification SEM image of a tile from sample PD1 showing no V-defects on the surface. SEM imaging done by Boyu Wang. 113
Figure 6-14: RT PL for the PD series: 4-step composition grade on planar GaN (PD1A - shown at the dotted grey curve) and on PS (PD1 - shown as the solid black curve). GaN peak from a standard

MOCVD grown template is shown in solid blue. The yellow arrow indicates the approximate location of where the YL defect peak would be. Peak wavelegths for PD1 and PD1A are approximatly 497 nm and 482 nm respectively. 114
Figure 6-15: Cross-section STEM image taken one the $11\bar{2}0$ zone axis for sample PD1 (4-step grade grown on PS). (a) STEM Bright-field (BF) image which shows a dislocation generated in the InGaN and (b) STEM HAADF image which shows the different layers more clearly and also shows the pure-edge component dislocations in the UID GaN layer under the tiles. STEM analysis done by Dr. Kai Sun at the University of Michigan. 115
Figure 6-16: Plane-view STEM BF images using a ~200 nm foil thickness for (a) sample PB2 (120 nm $In_{0.2}Ga_{0.8}N$ on PS) and (b) sample PD1 (4-step grade on PS). From this, PD1 is highly dislocated compared to PB2. STEM analysis done by Dr. Kai Sun at the University of Michigan. 116
Figure 6-17: $x_{In,equiv.}$ as a function of InGaN thickness for growth on PS (represented as diamonds) and planar GaN (represented as x's). The black dotted line shows the overall $x_{In,equiv.}$ trend of the InGaN grown on PS which appears to have an approximate ceiling of 16% $x_{In,equiv.}$ under the explored experimental conditions. 118
Figure 7-1: Proposed process flow for obtaining RGB monolithic integration using a single MOCVD MQW growth on tiles with varying sizes. 123

List of Tables

Table 4-1: Data for In-BEP study IA1-4 showing In-composition and surface RMS values extracted from the AFMs in Fig. 4-2 for four In-fluxes 54
Table 4-2: Data summary for the IB1-4 58
Table 4-3: Experimental data for IC1-4 showing substrate temperature, In-composition extracted from (0002) ω-2θ XRD scans and surface RMS extracted from AFM. 62
Table 4-4: experimental data for the ID and IE series. In-composition (x_{In}) and relaxation (R) were extracted from ($1\bar{1}\bar{1}24$) XRD RSM scans shown in Fig. 4-8. 68
Table 6-1: summary of experimental results from every study in this chapter on both PS and planar GaN. t_{InGaN} refers to the total InGaN thickness of the sample, including InGaN layers from previous runs as in the case of PB3, PC2, PC2A, PC3 and PC3A which were InGaN regrowths on previously grown InGaN layers. PB2 which had the highest $x_{In,equiv.}$ and was free of new dislocations in the InGaN is in bold. 117
Table A-1: Growth conditions and experimental results for AI1-3 130

List of Symbols and Acronyms

GaN: Gallium Nitride

CAGR: Compounded annual growth rate

MOCVD: Metal organic chemical vapor deposition

HVPE: Hydride vapor phase epitaxy

MBE: Molecular beam epitaxy

PAMBE: Plasma-assisted molecular beam epitaxy

n_π: Spontaneous polarization sheet charge density n_π $[cm^{-2}]$

e_{ij}: Strain-moduli tensor components in position (i,j)

c_{ij}: Elastic tensor component in position (I,j)

$P_{pz,[0001]}$: Piezoelectric polarization in the (0002) plane

ϵ_1 : In-plane strain component [unitless]

a_i: In-plane lattice constant of some film (Å)

a_{GaN}: in-plane lattice constant of GaN (Å)

P_{PE}: Piezoelectric polarization [cm^{-2}]

P_{SP}: The spontaneous polarization [cm^{-2}]

2DEG: Two-dimensional electron gas

HEMT: High electron mobility transistor

L_g: Gate length

L_{gs}: Gate-to-source length

V_{gs}: Gate-to-source voltage

V_{sd}: Source-to-drain voltage

AELD: Adlayer enhanced lateral diffusion

RT: Room-temperature

PL: Photoluminescence

YL: Yellow luminescence

AFM: Atomic force microscopy

ρ_c: Critical radius of curvature

γ: Step-energy per molecule

a: Monolayer height,

P: Actual vapor pressure

P_o: equilibrium vapor pressure

T: temperature

k: Boltzmann constant

TD: Threading dislocation

TDD: Threading dislocation density

C-AFM: Conductive atomic force microscopy

DCXRD: Non-destructive double crystal x-ray diffraction

RHEED: Reflection high energy diffraction

AIL: AlN initiation layer

BEP: Beam equivalent pressure

XRD: X-ray diffraction

HRTEM: High-resolution transmission electron microscopy

CBr_4: Carbon tetra-bromide

CBED: Convergent-beam electron diffraction

SIMS: Secondary ion mass spectrometry

HF: Hydrofluoric acid

FS: Free-standing

IL: Interlayer

LED: light emitting diode

FM: Frank-van der Merwe

E_h: Strain energy per unit area

σ_x: In-plane misfit stress

h: Thickness of a layer

G: Shear Modulus

υ: Poisson ratio

h_c: Critical thickness for deformation

MD: Misfit dislocation

F_ϵ: Misfit strain

F_l: Line tension

b: Burgers vector

λ: Angle between the slip direction and the direction in the film plane that is perpendicular to the line of intersection of the slip plane

α: Angle between the dislocation line and the Burgers vector

ϵ_{max}: Maximum value of strain that a layer can have before relaxation

a(x): Bulk lattice constant of the pseudomorphically grown film as a function of alloy composition x

ϕ_{Ga}: Incident Ga-flux

ϕ_N: Incident N-flux

ϕ_{In}: Incident In-flux

T_c: Car temperature (substrate temperature measured from thermocouple)

$FWHM_{(0002),InGaN}$: XRD (0002) $\omega - scan$ FWHM value for InGaN

AR: Augmented reality

VR: Virtual reality

IR: Infrared

CPE: Composition pulling effect

QW: Quantum well

QCSE: Quantum confined stark effect

IQE: Internal quantum efficiency

AlInGaP: Aluminum gallium indium phosphide

WPE: Wall-plug efficiency

MQW: Multi-quantum well

SCAM: $ScAlMgO_4$

EQE: External quantum efficiency

PS: Porous GaN tiled pseudo-substrates

RIE: Reactive ion etching

EC: electro-chemical

$x_{In,equiv.}$: Equivalently relaxed In-composition

a_{new}: New in-plane lattice constant

STEM: Scanning transmission electron microscopy

MCMC: Michigan Center for Materials Characterization

HAADF: High-angle annular dark-field

LAADF: Low angular annular dark-field

BF: Bright field

GRC: Growth rate calibrations

$FWHM_{(0002),AlN}$: FWHM values from the (0002) $\omega - scan$ for the AlN peak

1 Introduction

Gallium nitride (GaN) is arguably the most versatile semiconductor since Si. Commercial applications of GaN include, and are not limited to, power management, RF communications and optoelectronics. A market research report from Grand View Research on the global GaN semiconductor market estimates the GaN market size to be approximately $1.88 billion in 2021 with an expected compounded annual growth rate (CAGR) of 24.6% from 2022 to 2030 [1]. Fig. 1-1 below shows the projected U.S. GaN device market up to 2030 conducted by Grand View Research [1]. Nitride semiconductor films are grown by a variety of techniques including metal organic chemical vapor deposition (MOCVD) which is the preferred method for commercial applications; hydride vapor phase epitaxy (HVPE) which is one of the dominant growth techniques for bulk GaN substrates; and molecular beam epitaxy (MBE) which has historically been utilized more for low-volume and research-level nitride growth. The work presented in this thesis highlights certain

applications where MBE may be utilized over traditional, more scalable growth technologies such as MOCVD.

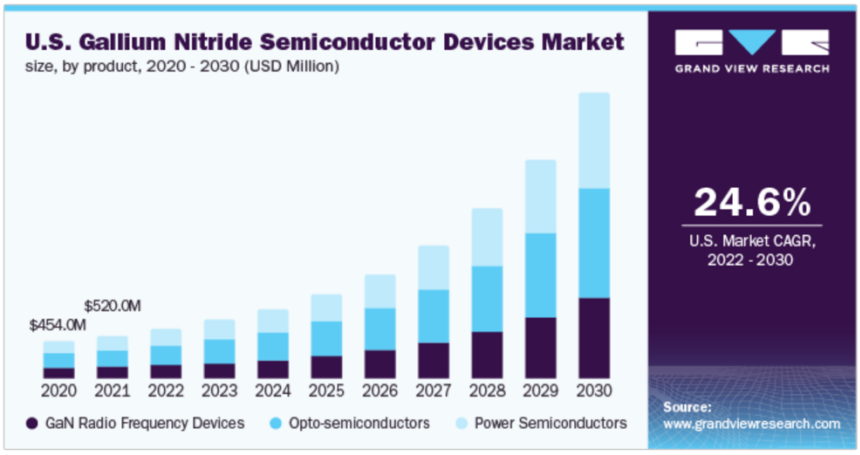

Figure 1-1: Projected GaN market in the U.S. spanning from 2020 to 2030 conducted by Grand View Research. Reprinted from [1].

This introductory chapter is meant to serve as a brief primer on GaN and plasma-assisted MBE (PAMBE) nitride growth. An introduction to the GaN crystal structure with an emphasis on polarization and how it is utilized for electronic applications will be given followed by an introduction to PAMBE nitride growth. To understand the motivation for PAMBE an in-depth discussion on MBE GaN vs. MOCVD GaN growth will be given. A significant amount of the content in this thesis will be devoted to surface morphology and the mechanisms which govern it, therefore it was necessary to devote a portion of this introductory chapter to understanding how growth conditions dictate surface morphology. Although there will be limited discussion on III-nitride based optoelectronics in this chapter, chapter 5 will give an overview of III-nitride based optoelectronics which is the chief motivation for the work presented in the second half of this thesis.

1.1 Gallium Nitride and Polarization Doping

Unlike traditional semiconductors such as Si, III-arsenides and phosphides, III-nitrides possess material qualities that make it especially advantageous for some electronic and optoelectronic applications. Although GaN and most III-nitrides can be grown in the zinc-blend phase, the wurtzite phase is the more stable of the two. This results in a non-centrosymmetric crystal structure with alternating polarization sheet charges along the c-axis (000+/-1 direction) which is illustrated in Fig. 1-2. Each of these internal polarization-induced sheet charges are effectively screened by the oppositely charged sheet charge preceding it. Figure 1-2 below shows the crystal structure of GaN and how the net polarization charges reside at each end of the crystal. The spontaneous polarization charge in GaN is approximately -0.029 C/m^2 [2] or a corresponding spontaneous polarization sheet charge density $n_\pi \sim 10^{13} cm^{-2}$ [3]. By simply rotating the GaN crystal structure 180 degrees leads to a change in polarity as is shown in Fig. 1-2.

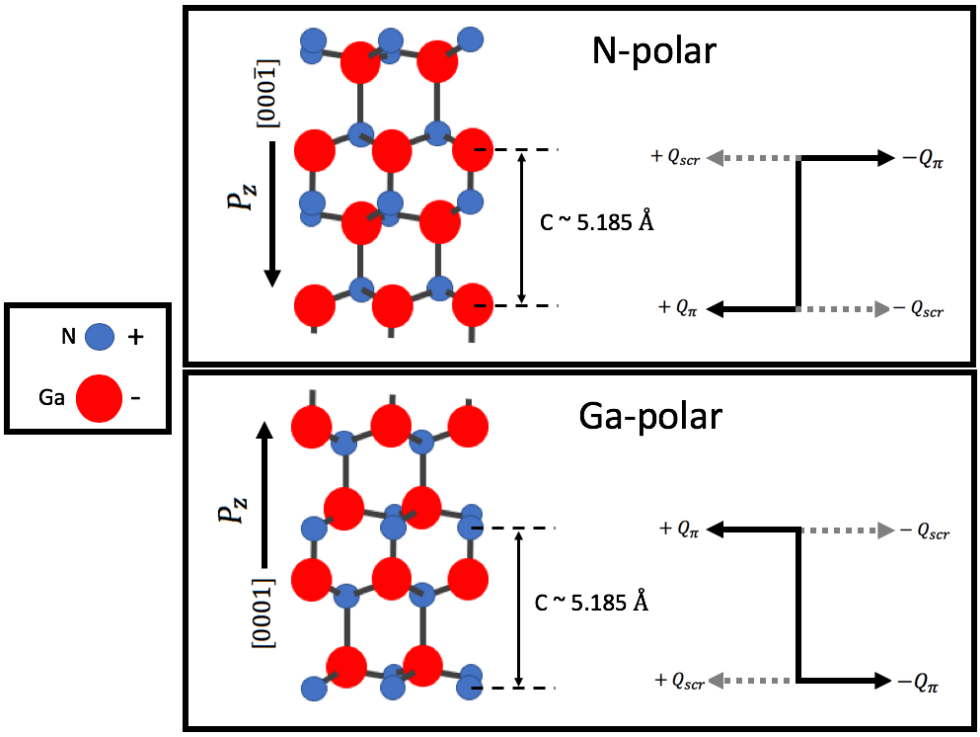

Figure 1-2: Wurtzite GaN unit cell showing polarization charges for N-polar (top) and Ga-polar (bottom). Reprinted with permission from [4].

1.2 Strained Heterostructures

In addition to the spontaneous polarization inherent in III-nitride films, there is also a piezoelectric polarization component which occurs in strained heterostructures such as GaN/AlGaN or GaN/InGaN. The piezoelectric tensor of wurtzite GaN has three non-vanishing independent components making wurtzite GaN highly piezoelectric [4]. In-plane strain adds additional polarization charge. In III-nitrides, assuming a heterostructure that is fully strained to GaN, this strain leads to a piezoelectric sheet charge at the heterointerface which is dependent on the strain-moduli components (e_{33} and e_{31}), the elastic coefficients (c_{13} and c_{33}) and the lattice constant of both materials given by:

$$P_{pz,[0001]} = 2\left(e_{31} - e_{33}\frac{c_{13}}{c_{33}}\right)\epsilon_1 \qquad 1.1$$

where the in-plane strain ϵ_1 arising from the lattice mismatch of the heterostructure is given by:

$$\epsilon_1 = \frac{a_i - a_{GaN}}{a_{GaN}} \quad \textbf{1.2}$$

Where a_i is the lattice constant of the material strained to GaN and can be found by Vegard's law [5]. The total polarization charge at a hetero-interface is the sum of the spontaneous polarization and the lattice mismatch dependent piezoelectric polarization charge. Hence the net polarization induced sheet charge at a hetero-interface is a strong function of the lattice mismatch between the GaN and the material strained to GaN. Although this can be advantageous for electronic devices, it is problematic for optoelectronic devices due to reduced electron-hole wavefunction overlap which will be shown in chapter 5. The increase in Al-composition leads to higher piezoelectric polarization (P_{PE}) strain at the GaN/AlGaN interface which becomes the dominate source of polarization only for Al-compositions above 90%. The spontaneous polarization (P_{SP}) is generally less dependent on Al-composition.

1.3 High Electron Mobility Transistors (HEMTs)

Polarization doping in III-nitrides has been utilized for high-power, high frequency transistors used for power amplifiers. When an AlGaN layer in an AlGaN/GaN heterostructure is sufficiently large, it will induce an electron sheet charge near the heterointerface. These polarization-induced electron sheet charges, which are generated without any doping, possess electron mobilities which exceed that of the bulk electron mobility. These electron sheet charges, known more commonly as a 2-dimentional electron

gas (2DEG), have been utilized as channels for HEMTs. The high mobility matched with the wide bandgap of GaN (~3.2 eV) make GaN HEMTs ideal for high-power, high-frequency amplifiers used in telecommunications and high power conversion. Fig. 1-3 below shows a basic Ga-polar and N-polar HEMT and indicates where the 2DEG channel is for each case. L_g is the gate width which corresponds to the width of the 2DEG channel under the gate that is modulated during switching. L_{sd} is the source-to-drain distance and L_{gd} is the gate-to-drain spacing which is typically longer than the distance from the gate-to-source to prevent breakdown at high drain biases. V_{gs} is the gate-to-source voltage and V_{sd} is the source-to-drain voltage. The first reported GaN HEMT was demonstrated by Khan et al., in 1993 [6]. In 2018, Romanczyk et al., demonstrated a record-high 8 watts/mm at 94 GHz GaN HEMT using an N-polar deep-recess design [7]. A more in-depth understanding on N-polar deep recess technology, and how it has evolved until 2018, can be found in reference [8].

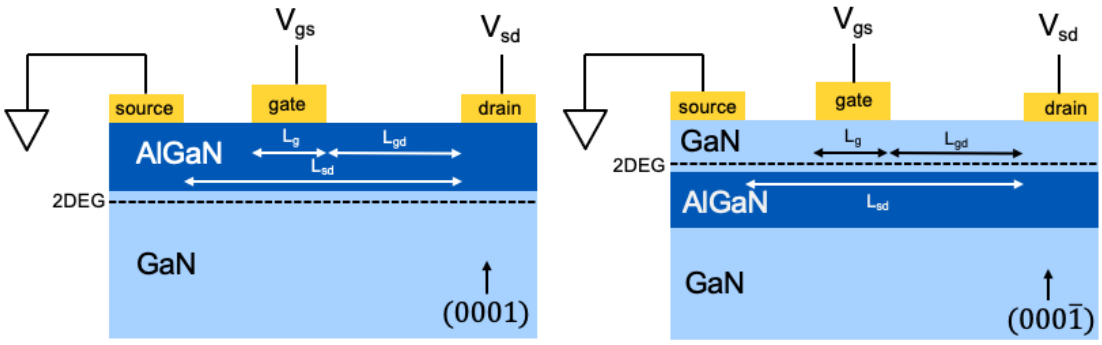

Figure 1-3: illustration of a simplified GaN-based (a) Ga-polar HEMT and (b) N-polar HEMT.

1.4 PAMBE GaN Growth

PAMBE nitride growth takes place in an ultra-high vacuum chamber with molten Ga, Al and In as the group III-sources. In a high vacuum environment, the sources, which are

contained in effusion cells, act as beams which travel directly to the sample stage. Active nitrogen is supplied by cracking N_2 gas with a high-vacuum based plasma source. During growth, the flow of N_2 gas (ranging from 0.5-several sccm) gives a background chamber pressure ranging from 5e-6 torr to 2e-5 torr.

The growth mechanisms behind high-quality GaN growth by PAMBE is significantly different than that of MOCVD. MOCVD nitride thin films are typically grown at temperatures of 1000^o C. or higher. At these temperatures, a high surface concentration of active nitrogen (0.2-1 barr) is needed to prevent GaN decomposition [9]. The high adatom mobilities facilitated by high temperature MOCVD growth reduce the probability of island-nucleation and promotes step-flow growth. PAMBE growth of nitrides, on the other hand, is typically done at a substrate temperature ranging from 500^o to 800^o C [10]–[13]. Growing at these low temperatures under N-rich conditions greatly reduces the adatom mobility leading to rough 3D surfaces such as what was studied by Tarsa et al., which resulted in films with columnar structures initiated by the formation of stacking faults [12]. The chief cause of poor surface morphology in N-rich MBE grown GaN has been traced to the high diffusion barrier for N (1.3 eV) [14]. Because of this N-adatoms are orders of magnitude less mobile with respect to Ga-adatoms on the GaN surface [14]. Growing in a Ga-rich regime, however, has been shown to improve adatom mobility at the lower temperatures employed by MBE leading to smooth surface morphology [12], [14]–[18]. In the case of Ga-rich growth, excess Ga floats on the surface lowering the adatom diffusion barrier for the N adatoms under the Ga-adlayer. Thus, the Ga-adlayer acts as an auto-surfactant leading to adlayer enhanced lateral diffusion (AELD) [17]. Both Köblmuller et al.,

and Tarsa et al., demonstrated that by increasing the Ga-flux for a series of growths led to a dramatic improvement in surface morphology [12], [19]. Furthermore, room-temperature (RT) photoluminescence (PL) measurements showed a suppression in the yellow luminescence (YL) peak, which is at approximately 2.2 eV, by increasing Ga-flux [20]. Although the YL peak has been associated with carbon in MOCVD GaN [21], it can be speculated that growth under Ga-rich conditions suppresses the Ga-vacancies which were associated with the YL peak. Although too high a Ga-flux to N-flux ratio can lead to Ga-droplets on the surface, it has been shown that at least two monolayers of Ga is needed on the surface to promote step-flow growth of Ga-face GaN by PAMBE [18]. Thus growing GaN in the Ga-rich regime by PAMBE improves both surface morphology and film quality and enables growth at significantly lower temperatures compared to MOCVD.

1.5 Dislocation Mediated Spiral Growth

In contrast to MOCVD, which is a mass-transport limited growth technique utilizing 'near-equilibrium' conditions, PAMBE is considered a highly 'non-equilibrium' growth technique [22], [23]. Metal-rich PAMBE growth results in spiral island like structures which form around dislocations or groups of dislocations. Fig. 1-5 below shows 2x2 μm^2 atomic force microscopy (AFM) micrographs of PAMBE grown GaN (Fig. 1-5.a) and MOCVD grown GaN (Fig. 1-4.b). From Fig. 1-4.a the step-terraces on the surface of the PAMBE grown GaN have significant curvature while some even spiral around small-pinholes on the surface. This is in contrast to Fig. 1-4.b (MOCVD grown GaN) which has straighter step-terraces.

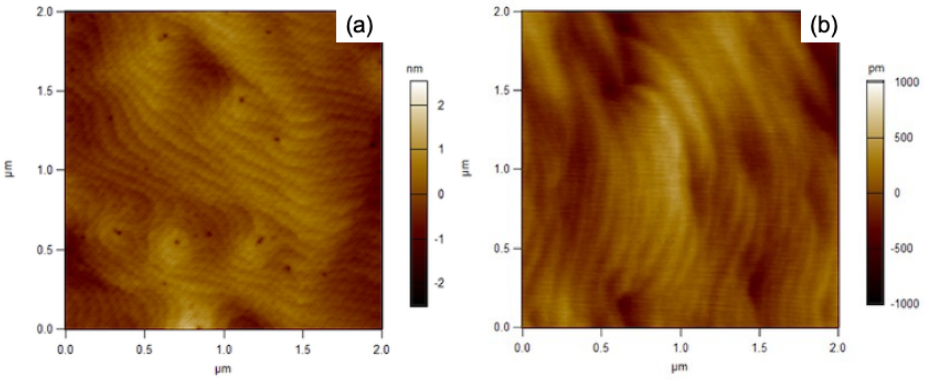

Figure 1-4: (a) atomic force microscopy (AFM) micrographs of PAMBE grown GaN and a (b) MOCVD grown GaN-on-sapphire template.

The spiral surface morphology exhibited in the PAMBE grown GaN seen in Fig. 1-4 has been well described by Burton, Cabrera and Frank [24]–[26]. When growth occurs on a surface terminated with mixed-type dislocations, step-terraces bow out around dislocations leading to a corresponding increase in energy of the system. The curvature of the bowing is governed by supersaturation [27] which is the driving force behind all crystal growth. For the case of a pinned step-terrace, the critical radius of curvature (ρ_c) of a step-terrace bowing out from a dislocation can expressed by the following relation [22][27]:

$$\boldsymbol{\rho_c = \frac{\gamma a}{kTln\left(\frac{P}{P_o}\right)}} \qquad 1.3$$

Where γ is the step-energy per molecule, a is the monolayer height, P is the actual vapor pressure, P_o is the equilibrium vapor pressure, T is the temperature and k is the Boltzmann constant. $kTln(P/P_o)$ is the driving force for growth. For $P \gg P_o$ (positive driving force), ρ_c becomes small and therefor the curvature becomes tight leading to defined spiral growth. For $P \sim P_o$, ρ_c becomes long and the steps become straighter. Actual spiral growth, such as what is observed in Fig. 1-4.a, occurs when a pinned step with a small ρ_c winds into a spiral around a mixed dislocation. The tightness of the spiral is determined by the advance

of the pinned step around the dislocation before reaching the critical curvature ($1/\rho_c$) at the center of the spiral [22]. Heying et al., demonstrated experimentally a decrease in spiral tightness by decreasing the III/V ratio for PAMBE grown GaN [22]. Thus, higher metal-rich conditions used by PAMBE results in a smaller ρ_c and thus spiral hillocks. As will be shown in chapter 4, lower temperature growth employed in PAMBE InGaN growth, leads to taller and tighter spiral hillocks. This dislocation-induced spiral morphology inherent in PAMBE growth will limit the flatness of a surface.

1.6 V-Defects

Another surface morphology feature which separates PAMBE from MOCVD is the formation of V-defects. Thick, MOCVD-grown InGaN and InGaN MQWs have often exhibited a high density of faceted pits on the surface. The formation of these pits, or V-defects as they are more commonly known, has been modeled [28],[29], [30] and studied experimentally in both InGaN and GaN [31],[32]. Hetero-epitaxially grown GaN, grown in the presence of indium by MOCVD, at temperatures lower than 1000 °C, can lead to elastic relaxation through the formation of V-defects. These V-defects nucleate around mixed-type threading dislocations (TDs) forming six equivalent $\{10\bar{1}1\}$ facets [32]. The growth rate on these facets is lower than that of c-plane GaN leading to an increase in V-defect diameter and depth with increasing film thickness [32]. While the elastic nature in which these V-defects alleviate local strain has been taken advantage of by some researchers for making longer wavelength LEDs [33], they create issues with scalability and can result in current leakage. In contrast, PAMBE-grown InGaN, performed under metal-rich conditions at growth temperatures between 500 °C and 600 °C, typically produces spiral step-flow

morphology free of V-defects. Mentioned previously, the metal adlayer acts as a surfactant lowering the adatom diffusion barrier of adsorbed species enabling step-flow growth at temperatures significantly lower than those used by MOCVD [17], [19], [34], [35], [36]. As will be shown in chapter 4, lower temperature growth can enhance lateral growth which suppresses V-defects. A smooth, well controlled growth surface is a prerequisite for regrowth of subsequent high-quality layers whether by MBE or MOCVD.

V-defects have also been observed in N-polar PAMBE grown GaN on bulk GaN [37],[38],[37]. V-defects which were observed in PAMBE grown N-polar films by Turski et al., and Chéze et al., on bulk GaN, in [39] and [37] respectively, were attributed to slow growing parts of a step meander when two adjacent meanders connect [39]. It was shown that these V-defects could be suppressed by using miscut substrates which reduced the terrace widths on the surface thereby making the steps more periodic - small periodic terraces reduce the effects of unusual step-meandering [39] [37]. The following chapters will confront and address the problem of V-defects in both PAMBE grown N-polar GaN and Ga-polar InGaN.

1.7 Conclusion

This introductory chapter was meant to provide a high-level understanding of the nitride material system with an emphasis on polarization. The non-centrosymmetric nature of wurtzite GaN leads to internal polarization-induced electric fields which induces band-bending without any doping. Because of this 2DEG channels can be realized without any doping. PAMBE nitride growth is carried out at lower growth temperatures than those

employed by MOCVD. Unlike MOCVD, the surface morphology of metal-rich PAMBE grown nitrides results in a dislocation mediated surface morphology where spiral hillocks radiate from mixed-type dislocations which terminate on the surface. This spiral step-flow morphology limits how flat the surface morphology can be for a substrate with a given dislocation density. V-defects are common in thick MOCVD grown InGaN whereas the growth conditions employed by PAMBE suppresses V-defects. However, N-polar GaN grown by PAMBE on non-vicinal bulk GaN can also lead to V-defects. The emphasis on surface morphology is made to support and understand the work presented in the following chapters. The first part of this thesis describes how V-defects were eliminated in N-polar GaN grown by PAMBE on non-vicinal GaN substrates. Equally important to how V-defects were eliminated is how and where they were generated. The second part of this thesis focuses on Ga-polar InGaN grown by PAMBE on planar and porous tiles to enhance elastic relaxation. Although the applications of the two topics presented in this work are very different they both show a clear advantage PAMBE has over the more commercially-acceptable MOCVD.

2 Growth of High-Quality N-polar GaN on Bulk GaN by PAMBE

High-quality $(000\bar{1})$ GaN, or N-polar GaN, grown on bulk GaN may have potential in high-frequency, high power electronics. N-polar HEMTs have demonstrated superior performance when matched against their Ga-polar counterparts in terms of operating frequency, power output and scalability [7],[40]. Growing GaN on foreign substrates such as SiC, for example, where an in-plane 3.4% lattice mismatch [41] is present, results in vertically propagating threading dislocations (TDs). Typical threading dislocation density (TDD) for GaN grown on sapphire and SiC by MOCVD are on the order of $10^8\ cm^{-2}$ [42]. High quality N-polar GaN grown by MOCVD on vicinal sapphire and SiC has already been used extensively to make high performance HEMTs [43]. At high concentrations, threading dislocations can act as scattering centers which can degrade device performance [44]. Therefore it is necessary to investigate growth of GaN devices on low TDD bulk GaN

substrates. This chapter begins with a brief primer on dislocation related scattering and the motivation behind growth on bulk GaN, followed by past work done by other groups doing N-polar GaN homoepitaxy. Experimental work will be presented showing how N-polar GaN-on-GaN grown by PAMBE with smooth surface morphology was achieved on non-vicinal substrates.

2.1 Motivation for Bulk GaN Substrates

The N-polar HEMT mentioned in chapter 1 which demonstrated record high output power at 94 GHz (Romanczyk et al.) was grown on SiC by MOCVD and possessed a TDD on the order of 10^8 cm^{-2} [7]. This being known, there is interest in whether device performance could be greatly improved by growing HEMT epi on native substrates with two or more orders of magnitude lower TDD. To better understand the motivation for switching to bulk-GaN substrates, which are expensive and far less abundant compared to SiC and sapphire, it is necessary to understand how dislocations arising from lattice mismatch can negatively affect device performance.

GaN and sapphire have a 14% in-plane lattice mismatch and a 34% thermal mismatch (mismatch between thermal expansion coefficients of GaN and sapphire), which, when grown by MOCVD, leads to a TDD of approximately 10^{10} cm^{-2} in the GaN immediately following the heterointerface [45]. GaN and Si have an in-plane lattice mismatch of 17%, the thermal mismatch is 115% [46]. In contrast, GaN and SiC have an in-plane lattice mismatch of just 3.4% [47] and very similar thermal expansion coefficients ($\alpha_{GaN} = 5.6 \times 10^{-6}/K, \alpha_{AlN} = 4.2 \times 10^{-6}/K, \alpha_{SiC} = 3.2 \times 10^{-6}/K$) [48]. In all cases a high

density of screw dislocations and edge dislocations exist near the heterointerface due to lattice mismatch. These dislocations tend to propagate in the growth direction and terminate on the surface [49]. Thick MOCVD GaN buffer layers have been utilized to suppress TDDs by almost two orders of magnitude. When growing thick GaN buffers at high temperature, typically around 3 μm, TDs tend to intersect as they travel in the growth direction resulting in the annihilation of one or both TDs [50]. This thick MOCVD buffer technique has led to TDD values on the order of 10^8 cm^{-2} for growing GaN on sapphire and SiC - nearly two orders of magnitude reduction in TDD compared to conventionally grown thin heteroepitaxially grown layers [19].

The amount of work showing how dislocations affect carrier transport in GaN is extensive. A model developed by Weinman et al., which was verified experimentally, showed that filled traps along the TD line act as coulombic scattering centers impeding bulk mobility [51]. Using the Boltzmann transport equation, Look et al., developed a model for charged-dislocation-line scattering showing how edge dislocations are electrically active [45]. Later, in 2003, it was shown experimentally by conductive atomic force microscopy (C-AFM) imaging and scanning kelvin probe microscopy, that potential variations on the GaN surface arose from negatively charged TDs and localized leakage paths associated with dislocations. Using this method it was determined that edge dislocations near the surface were negatively charged [52]. Using non-destructive double crystal x-ray diffraction (DCXRD) and temperature-dependent Hall, Zhao et al. demonstrated bulk electron mobility and carrier concentration were both effected by TDD; higher dislocation density led to lower mobility and higher background carrier concentrations [53]. Kyle et al. measured a

reduction in bulk mobility for GaN with high TDD grown by NH_3 MBE and postulated that dangling bonds associated with edge dislocations act as acceptor states which trap electrons thereby becoming negatively charged [10].

Ga-polar HEMTs grown on bulk GaN substrates display higher Hall mobilities and lower sheet resistances [54], [55]. Kyle et al., modeled dislocation-dependent mobility assuming an acceptor-like trap exists at every c-lattice translation along an edge-type dislocation, and that this trap state is ionized (negatively charged) thereby causing an electric field around the dislocation [10]. This model was successfully demonstrated experimentally by analyzing temperature dependent bulk mobility by growing a series of samples on substrates with varying TDD [10]. When dislocations become charged they can act as scattering centers in the 2DEG channel of a HEMT. Scattering in the channel creates heat which lowers the overall efficiency. Therefore, if the primary objective of designing a device or an amplifier is to have ultra-high efficiency, reducing the dislocation density would be advantageous.

As discussed in chapter 1, surface-terminated dislocations in MBE grown GaN can lead to tall spirals around dislocations [12], [37], [49] [19]. The poor surface morphology resulting from these dislocations can make it difficult to process devices with ultra-small features and can lead to defects on the surface which may potentially affect RF performance.

PAMBE involves metal-rich growth which often results in metal decorated TDs that become vertically conductive paths. These metal-decorated TDs lead to high reverse-bias

leakage in GaN Schottky contacts and vertical devices [54]. This type of leakage is not so detrimental to lateral conducting devices such as HEMTs, however for optoelectronic devices such as LEDs and vertical cavity surface emitting lasers (VCSELS) they can be catastrophic. This is one reason why MOCVD is the preferred method for optoelectronic devices.

2.2 Motivation for MBE

By MOCVD, growth of N-polar GaN is particularly challenging due to the nature of the N-polar surface. Theoretical calculations done by Zywietz et al., predict a much higher diffusion barrier for N compared to Ga - 1.4 eV and 0.4 eV, respectively [56]. Initial MOCVD grown N-polar GaN on planar substrates resulted in a high density of hillocks on the surface however, this was mitigated by growing at temperatures above 1000^{o} C on miscut substrates [43]. Unlike MOCVD, MBE N-polar GaN grown on bulk GaN and SiC has been achieved without the use of vicinal substrates [57], [43],[58]. Furthermore, PAMBE yields films with highly abrupt interfaces and offers in-situ growth monitoring by refection high-energy diffraction (RHEED) making it ideal for proof-of-concept devices.

2.3 Past Work of PAMBE grown N-polar GaN on Bulk GaN

Before high quality N-polar devices can be grown and processed on bulk GaN substrates growth conditions must be optimized to ensure smooth surface morphology and high-quality films. As mentioned in chapter 1, N-polar GaN grown on bulk GaN yielded surfaces which had a high density of V-defects [37], [39][38]. These V-defects have also been observed in MBE-grown Ga-polar films by Heying et al., and Tarsa et al., in references

[22] and [12] respectively. Heying et al., attributed surface V-defects, or surface depressions, to different types of surface terminated dislocations [22]. Past N-polar GaN HEMTs grown on bulk GaN by PAMBE displayed inferior electrical data compared to other N-polar HEMT devices grown by MOCVD. This was attributed to the high density of V-defects on the surface [38].

2.4 Summary of Study

In the following study a 2-step approach is employed to eliminate surface-V-defects on N-polar GaN grown on non-vicinal bulk GaN. First, the substrates were subjected to an ex-situ UV-ozone clean. Next, the growth was initiated with a 2 nm thick AlN layer grown under Ga-rich conditions which we call the AlN initiation layer (AIL). Growing thicker AILs (up to 8 nm) showed to improve film quality further while still maintaining smooth surface morphology. It was postulated that these V-defects generate at the regrowth interface due to impurities. This theory was later confirmed when surface V-defects were re-generated at ultra-high C-concentrations following the surface treatment described above.

2.5 Experimental Procedure

Four sets of experiments were carried out to observe the effects of the UV-ozone clean (NA1-NA2), the effects of the 2nm AIL (NB1-NB3), AIL thickness (NC1-NC4) and the effect of carbon doping on surface morphology (ND1-ND3). The details of this study are also given in references [8], [59].

For every sample in this study semi-insulating (SI) N-face epi-ready bulk GaN substrates provided by NGK Insulators were used. Except for sample NA1, every sample

underwent a 15-minute ultra-violet (UV) ozone clean followed by a one-minute dip in hydrofluoric (HF) acid. The UV-ozone treatment and the HF dip were repeated two more times before 500 nm of Ti was deposited on the back of the wafers using an electron-beam evaporator. Prior to loading into the growth system, the samples were cleaned in acetone, methanol, and isopropyl alcohol. All samples were mounted using molten indium to 3" Si substrates.

All growths in this study were carried out using a Varian Gen II MBE system with conventional Al, Si and Ga effusion cells. A Riber rf-plasma source was used to supply active nitrogen for growth. For active nitrogen, ultra-high purity N_2 (99.9995% purity) was used. 3 sccm of N_2 at a plasma power of 250 watts was used which resulted in a growth rate of approximately 8 nm/min. To maintain Ga-rich conditions the Ga-flux used for both the GaN and AlN growth was kept constant at a beam equivalent pressure (BEP) of 4.4×10^{-7} torr while Al-flux for AlN growth was 1.4×10^{-7} torr. All AlN layers were grown in the presence of a Ga-flux to maintain a Ga-adlayer during growth. Chamber pressure during growth was approximately 3×10^{-5} Torr. Substrate temperature was monitored during growth by an optical pyrometer calibrated to the melting point of Al. Growth temperature for every growth in this study was measured at 740 ℃. Prior to growth, the substrates were brought up to the growth temperature and exposed to Ga-flux (same Ga BEP used for GaN) for 10 seconds followed by a thermal desorb of the excess Ga on the surface to remove any impurities still on the substrate surface. To ensure good surface morphology all samples were grown under Ga-rich conditions such that a Ga-adlayer was present on the surface throughout the entire growth. The Ga-adlayer was monitored by observing the intensity

from reflection high energy electron diffraction (RHEED). Growths were interrupted approximately every ten minutes to desorb excess Ga on the surface preventing the formation of droplets. Carbon doping was carried out using a carbon tetra-bromide (CBr_4) solid source bubbler. CBr_4 was introduced to the system via an automated control valve to throttle the vapor pressure from the CBr_4 bubbler to a foreline and into the system [60].

Surface morphology for each sample was characterized by atomic force microscopy (AFM). Samples NB3 and NC1-NC4 were characterized by x-ray diffraction (XRD) rocking-curve scans near the (0002) and $(\bar{2}021)$ reflection. High-resolution transmission electron microscopy (HRTEM) imaging was also carried out on sample NB2 along with convergent-beam electron diffraction (CBED) to rule out any possibility of polarity inversion due to the AIL. HRTEM and CBED analysis was performed by Dr. Feng Wu of the Speck group at the UC Santa Barbara Materials Department. Film thickness for all samples, except NA1-NA2, were verified by measuring interference fringe spacing from XRD (0002) ω-2θ scans, a technique which is explained in more detail in reference [61]. To verify that the thickest AIL was strained to the GaN, a reciprocal space map (RSM) near the $\{10\bar{1}5\}$ reflection was generated by XRD on sample NC4.

Secondary ion mass spectrometry (SIMS) using a Cameca IMS 7f Auto SIMS system was carried out to observe impurities in the epitaxially grown films with an emphasis on the regrowth interface. SIMS characterization was done with the help of Dr. Tom Mates of the California Nano-Systems Institute (CNSI).

2.6 Effects of UV ozone clean (NA)

Regrowth interfaces are well known to have a high surface concentration of impurities. The cause of these impurities have been attributed to contaminates accumulating on the surface prior to growth, residual impurities left as a result of the chemical mechanical polishing of the substrate by the manufacture, or from impurity gettering inside the MBE chamber [60]. Given the reactivity of the N-polar surface, subjecting the substrate to an ex-situ cleaning process before growth is of interest for subsequent epitaxial regrowth of N-polar GaN. UV-ozone treatments had been used by Gupta et al., to remove Si particulates from a post RIE-etched surface of Si-doped GaN [62] [30]. It is believed that exposing the GaN surface to O_3 and UV light converts the GaN surface into a thin gallium oxide layer. By submerging the substrate in HF the oxide on the surface, along with any impurities which is absorbed, would be stripped away leaving behind an ultra-clean surface. Repeating this process several times can help to reduce surface impurities even further.

For this study, sample NA1 was subjected to the standard solvent clean and in-situ Ga-polishing described above before regrowth of 250 nm of GaN. Sample NA2 was subjected to a 3x UV-ozone clean (3 consecutive 15-minute UV-ozone cleans with 2-minute HF dips in between each UV-ozone clean) prior to growth of 250 nm of GaN. The AFM micrographs shown in Fig. 2-1 show a decrease in pit density for the UV-ozone treated sample (NA2) with a corresponding surface RMS of 12.2 nm and 1.41 nm for NA1 and NA2 respectively. Although the UV-ozone treatment greatly reduced the pit density, resulting in more than an order of magnitude lower surface RMS value, it did not eliminate them

completely. More impurities could have been introduced after the UV-ozone clean either from the atmosphere or gettering in the chamber.

SIMS analysis was carried out to observe O, Si and C concentration in two 400 nm thick N-polar GaN samples grown on bulk GaN. As with NA1 and NA2, the first sample underwent the standard cleaning process while the second sample was subjected to the 3x UV-ozone treatment described above. The SIMS depth profiles for these two samples are shown in Fig. 2-2. From Fig. 2-2, O and Si concentration at the regrowth interface were nearly unchanged, however, the C-concentration reduced by an order of magnitude in the UV-ozone treated sample. These SIMS results, along with the AFM results from NA1-2, give the first piece of evidence to suggest that impurities on the surface play some role in the generation of V-defects.

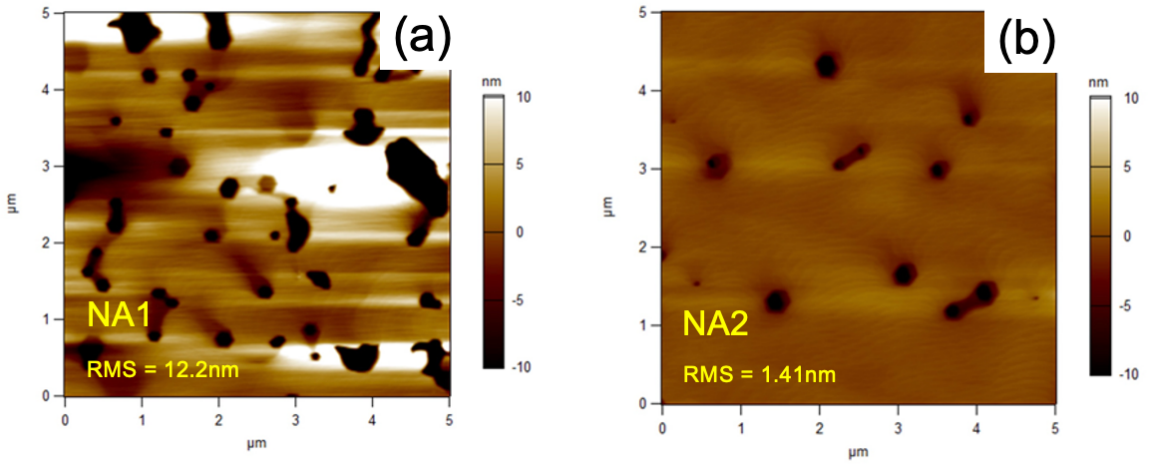

Figure 2-1: (a) AFM micrograph for sample NA1, (b) AFM micrograph for sample NA2 which was subjected to a UV-ozone clean prior to growth. Surface RMS extracted from these AFMS were found to be 12.2 nm and 1.41 nm for NA1 and NA2 respectively. Reprinted with permission from [59], Copyright Elsevier 2020.

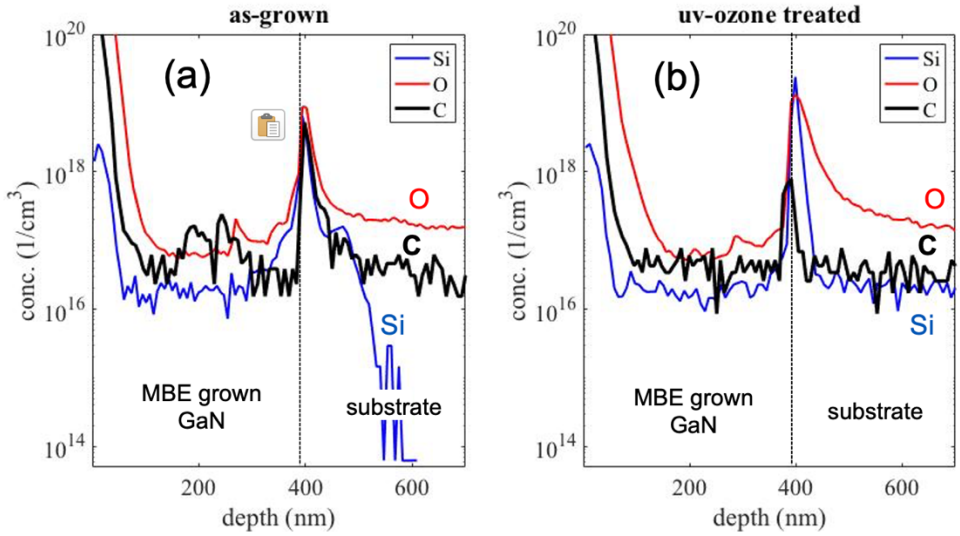

Figure 2-2: SIMS results for 400 nm of GaN grown directly on a N-polar free-standing (FS) GaN substrate (a) which was only subjected to a standard solvent clean and (b) one which was subjected to the 3x UV-ozone treatment as described in section 2.6.

2.7 AIL: AlN initiation layer (NB)

Al-containing materials have been used as nucleation layers and as diffusion barriers for impurities during epitaxial growth. A 20 nm AlAs layer, for example, had been used by Ibbetson et al., as a diffusion barrier between doped GaAs and low temperature grown undoped GaAs [63]. 70 nm AlN nucleation layers grown under nitrogen-rich conditions have also been used in GaN/SiC heteroepitaxy to block impurities from the SiC substrate from diffusing into the MBE-grown GaN [64],[65],[44]. AlN has also been utilized as a buffer layer for GaN grown on Si(111) [66], [67]. Given AlN's success as a nucleation layer for heteroepitaxy and as an impurity diffusion barrier there is an interest in seeing if it would be advantageous for homoepitaxy as well.

For the NB series, three samples were grown using different structures to observe the effects of using a thin AlN initiation layer. In this study, all samples were subjected to the 3x UV-ozone treatment described above. Sample NB1 was initiated with 2 nm of AlN

followed by 250 nm of GaN. Sample NB2 was initiated with 3 nm of GaN followed by 2 nm of AlN before the subsequent 250 nm of GaN was grown. Finally, for sample NB3, 250 nm of GaN was grown directly on the GaN substrate. As stated above, growth conditions for the AlN layers did not differ from that of the GaN layers, that is, the AlN layers were also grown at 740 ℃ using the same Ga-flux but with an Al-flux of 1.4×10^{-7} torr. These epi-structures with their corresponding AFM images are shown in Fig. 2-3 below.

From the 5x5 μm^2 AFM images in Fig. 2-3, initiating growth with just 2 nm of AlN appears to eliminate the V-defects on the surface completely. Only when growth is initiated with AlN, the surface V-defects disappeared, while inserting AlN after only 3 nm of GaN growth (NB2 -Fig. 2-3.b) results in V-defects on the surface just like the as-growth GaN with no AlN (NB3 – Fig. 2-3.c). The AFM micrographs for NA1 and NA2 shown in Fig. 2-1, are a compelling piece of evidence suggesting the nucleation of V-defects occurs at the substrate interface and not later in the growth. Looking at Fig. 2-3.b where AlN was grown after initiating with a thin layer of GaN, V-defects were still observed suggesting that once the V-defect is generated at the regrowth interface it cannot be suppressed by the AlN.

SIMS results, not shown in this work, have confirmed a spike in impurity concentration in AlN interlayers used in GaN which is typically larger than what is seen at the regrowth interface. Given the higher bond energy Al has with other species, with respect to Ga and In, it is thought that these AlN interlayers getter impurities from inside the growth chamber [25].

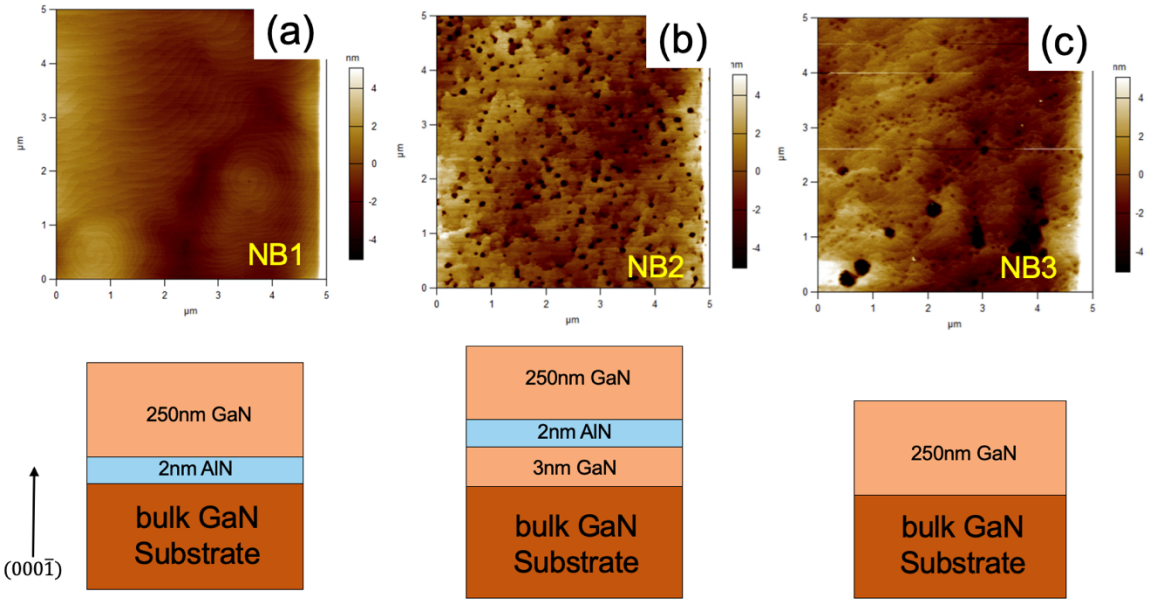

Figure 2-3: NB-series AFM micrographs with corresponding structures below for (a) NB1, (b) NB2 and (c) NB3. Reprinted with permission from [58], Copyright Elsevier 2020.

Cross-section HRTEM imaging was carried out on sample NB1 to observe the heterointerface which is shown in Fig. 2-4. From Fig. 2-4.a, the top AlN/MBE GaN interface appears atomically flat. Because of the higher bond energy of Al with respect to Ga and N [68], it is likely that the incoming Al-flux more readily bonds with impurities on the surface compared to Ga. It can be speculated that as the AlN continues to grow the surface smoothens as is seen in the top AlN/ GaN interface in Fig. 2-4.a. It is on this abrupt, impurity free, AlN surface that smooth GaN can grow in step-flow mode without generating V-defects. Provided the AlN is thin enough such that it is fully strained to the GaN, no new dislocations will be generated due to lattice mismatch between AlN and GaN. Results from the UV-ozone treatment also support this theory as we see a reduction in V-defects from performing the UV-ozone treatment of the substrate surface (see Fig. 2-1). Furthermore, the HRTEM image shown in Fig. 2-4.b reveals a large number of defects in the substrate. V-defects may also be generated where these defects intersect with the surface. Given that

AlN buffers and nucleation layers have shown to produce smooth GaN when grown on non-native substrates [44], [64], [65],[67] it is likely that AlN is less sensitive to generating V-defects around defects and impurities compared to GaN.

The elimination of pits in the N-polar GaN grown by MBE using the AIL is significant and novel. Therefore, any possible change in the film which cannot be seen by AFM needs to be analyzed. Initiating growth with AlN has been known to invert polarity (i.e. converting N-polar films to Ga-polar). It has been demonstrated that AlN buffer layers used to grow GaN by PAMBE on (111) Si inverted the polarity of the AlN from N- to Al-polar by using highly Al-rich conditions [67]. Therefore CBED imaging was carried out on sample NB1 to check for polarity inversion. CBED patterns shown in Fig. 2-4.b for the substrate and the PAMBE grown film (NB1), compared with simulated results, revealed that no polarity inversion took place due to the AIL and both the substrate and the epi are indeed N-polar.

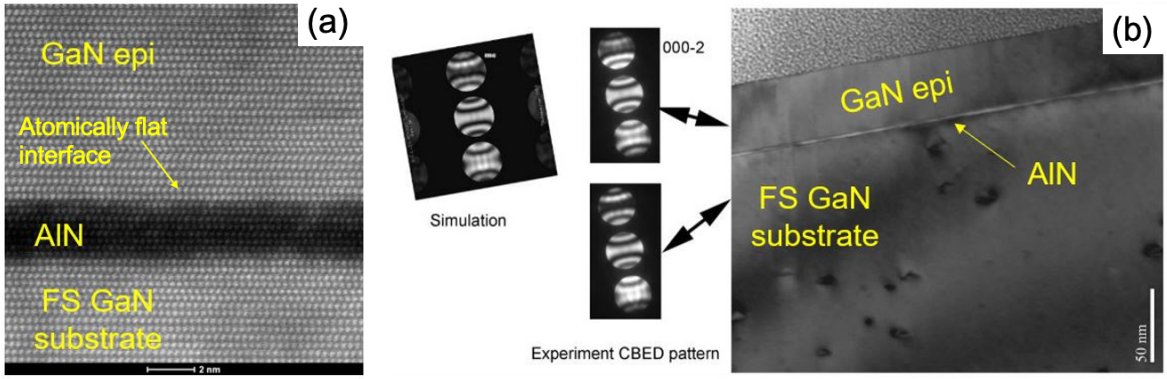

Figure 2-4: (a) HRTEM image taken for NB1 at the AIL. Cross-section direction is (11-20). (b) TEM images and CBED patterns for NB2 showing both the simulated and experimental patterns for above and below the AIL. TEM analysis done by Dr. Feng Wu of the Jim Speck Group at UCSB. Reprinted with permission from [58], Copyright Elsevier

Due to the reactive nature of the N-polar surface, many common chemicals used in semiconductor device processing will roughen or etch the N-polar surface. This includes

hydrochloric acid (HCl), potassium hydroxide (KOH) and many types of photoresist developers. Therefore, these chemicals can be a valuable and inexpensive tool for checking polarity inversion especially compared to CBED. A 100 nm N-polar GaN layer was grown on the N-polar substrate and was initiated with the AIL. As in the case of NB1, AFM scans showed that there were no visible V-defects on the surface as a result of using the AIL (Fig. 2-3.c). This sample was subjected to potassium hydroxide (KOH) for 5 minutes along with a standard Ga-polar MOCVD grown GaN-on-sapphire template. For both samples AFM was performed before and after the KOH dip to observe changes in the surface morphology. Fig. 2-5 shows the AFMs of the N-polar sample along with a standard MOCVD grown Ga-polar GaN-on-sapphire template before and after the KOH dip.

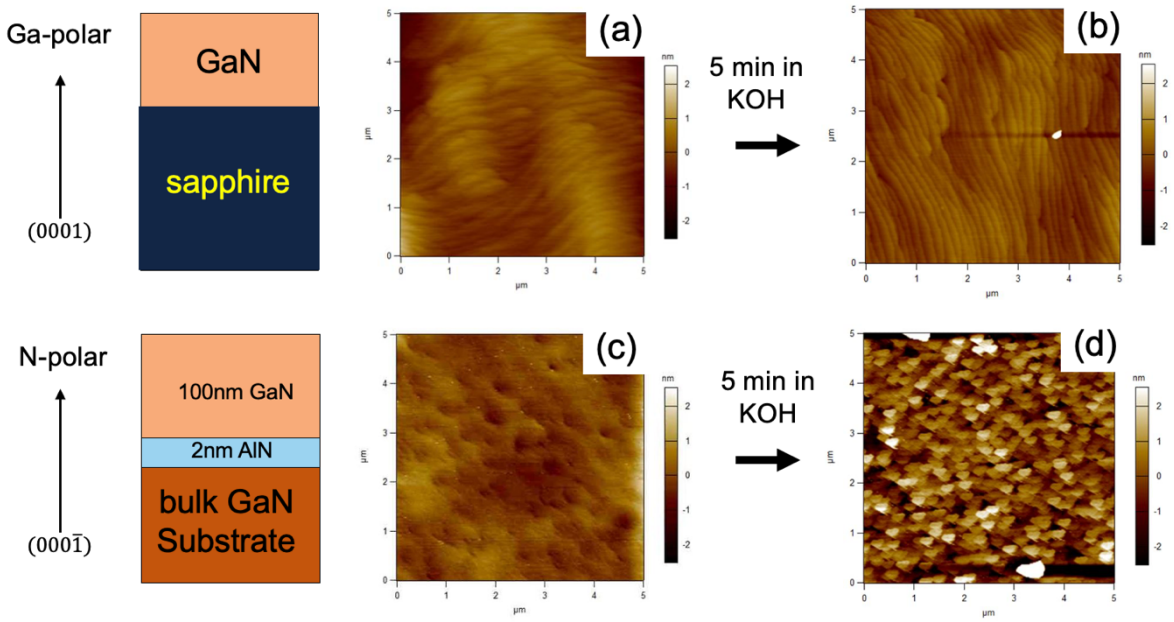

Figure 2-5: AFMs (right) along with corresponding sample structures (left) for (a) Ga-polar MOCVD grown GaN-on-sapphire template, (b) after 5 minutes in KOH, (c) 100 nm N-polar GaN grown by PAMBE on N-polar bulk GaN using the AIL and (d) after 5 minutes in KOH. Reprinted with permission from [8].

From Fig. 2-5.a and 2-5.b, clearly the surface morphology of the Ga-polar template is not affected by the KOH as would be expected. From Fig. 2-5.c and 2-5.c however, 5

minutes in KOH clearly roughens the surface. This along with the CBED analysis shown in Fig. 2-5, confirms that polarity inversion did not take place when using the AIL. This work presents a novel approach for obtaining high-quality, V-defect free, N-polar GaN grown on bulk GaN by PAMBE using the AIL.

2.8 AIL Thickness Study (NC)

With the dramatic improvement in surface morphology which came about by using the 2 nm AIL there is interest in seeing how thicker AILs would affect film quality and surface morphology. Samples NC1, NC2, NC3 and NC4 were each initiated with 2 nm, 4 nm, 6 nm, and 8 nm of AlN respectively followed by approximately 250 nm of GaN. Following growth, each sample was characterized by AFM and (0002) XRD $\omega - scan$s. The resulting AFM images and XRD rocking curve data are given in Fig. 2-6 below. Looking at Fig. 2-6.a we see that although the surfaces of NC1 and NC2 are free of V-defects, the steps appear more random compared to those in NC3 and NC4 where thicker AILs were used. The steps are not as straight in NC4 compared to that of NC3, which appears more characteristic of GaN grown on a miscut substrate. This surface morphology way be caused by unintentional miscut of the GaN substrate. Both NC4 and NC3 appear smoother compared to NC1 and NC2 where thinner AILs were used. The surface RMS values extracted from the AFMs in Fig. 2-6 were found to be 0.50 nm, 0.51 nm, 0.21 nm and 0.56 nm for NC1, NC2, NC3 and NC4 respectively. From Fig. 2-6.e there appears to be a decrease in on-axis and off-axis $\omega - scan$ FWHM values indicating the thicker AILs may have also improved film quality.

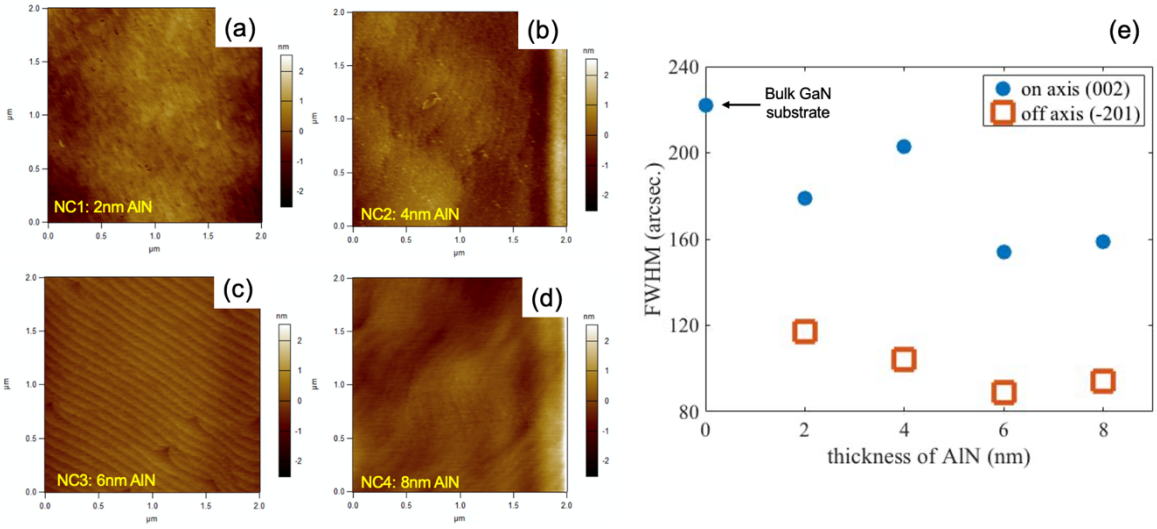

Figure 2-6: AFM scans taken for (a) NC1, 2 nm AIL, (b) NC2, 4 nm AIL, (c) NC3, 6 nm AIL, and (d) NC4, 8 nm AIL. RMS values extracted from AFM for ND1, ND2, ND3 and ND4 were found to be 0.50 nm, 0.51 nm, 0.21 nm and 0.56 nm respectively (e) XRD $\boldsymbol{\omega}$-scan FWHM values plotted as a function of AIL thickness with the blue circles representing FWHM values taken from the (0002) reflection and brown squares taken from the $\{\bar{\mathbf{2}}\mathbf{021}\}$ reflection. Reprinted with permission from [59], Copyright Elsevier 2020.

The lower temperature growth employed by MBE offers another benefit over MOCVD in its ability to grow thicker AlN interlayers coherently strained to GaN [69][70]. Mentioned previously, if the AIL remains coherently strained to the GaN, no dislocations will be generated due to the GaN/AlN lattice mismatch. The fact that there are no cracks observed on the surface of NC4 suggests that the 8 nm AIL is coherently strained GaN, however this needed to be confirmed by off-axis XRD RSM analysis. An XRD RSM scan taken near the $\{10\bar{1}5\}$ reflection for sample NC4 was performed which is shown in Fig. 2-7. The 8 nm AlN peak in Fig. 2-7 which sits directly above the GaN peak in reciprocal space confirms the 8 nm AIL is indeed coherently strained to GaN. The critical thickness for relaxation for AlN on GaN has been reported to be less than 5 nm [71], however, in this case the AlN interlayer (IL) is tensile strained from two different heterointerfaces (double heterostructure) thereby increasing the critical thickness. H. Li also demonstrated 8 nm AlN

ILs could be grown coherently strained to N-polar GaN by MOCVD [72]. It was also shown that AlN ILs, up to 15 nm thick, could also be grown coherently strained to GaN by MBE [70]. For future work it would be helpful determine the AlN thickness such that maximum film-quality and surface morphology is achieved without relaxation.

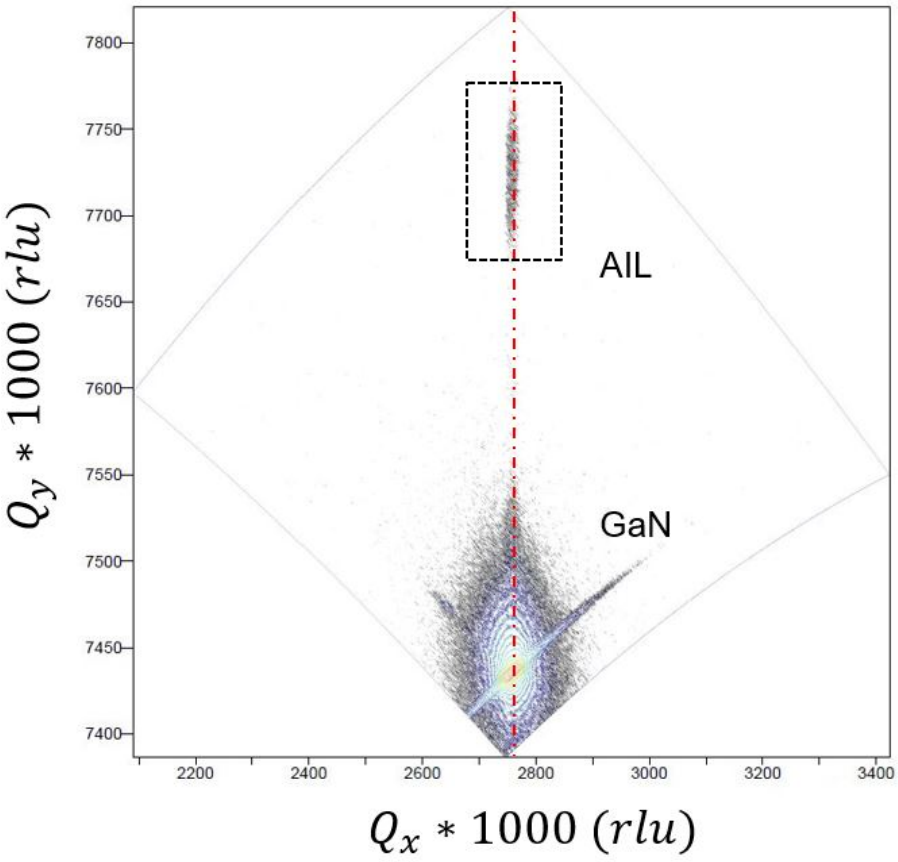

Figure 2-7: XRD RSM scan taken near the {10$\bar{1}$5} reflection for sample NC4 which was grown using the 8 nm AlL. Reprinted with permission from [58], Copyright Elsevier 2020.

From the results observed in Fig. 2-6 it can be concluded that using a thicker AlL will improve film quality and surface morphology. When GaN growth is initiated on the thicker AlL without interruption, there is less likelihood of generating V-defects or depressions resulting in higher quality N-polar GaN. The AlL effectively decouples the MBE grown GaN

from impurities and defects on the substrate surface. Fig. 2-6 demonstrates how this decoupling effect is enhanced when going to a thicker AIL.

2.9 Carbon Doping (ND)

CBr_4 is a common source for C-doping in MBE grown GaN to produce semi-insulating GaN buffer layers [73]. C-atoms occupy N-sites acting as deep level acceptors pulling the Fermi level away from the conduction band making the film more insulating [74] [60]. This has enabled the fabrication of semi-insulating GaN for transistor applications. Furthermore, the AIL described above could induce a parasitic channel near the regrowth interface which could potentially be mitigated by doping with some deep acceptor such as C. Knowing this, it was necessary to see how C-doping effected the surface morphology for N-polar GaN grown on bulk GaN.

For this study samples ND1-ND3 were each initiated with a 2 nm AIL followed by 200 nm of GaN:C. Samples ND1, ND2 and ND3 used a CBr_4 foreline pressure of 20, 40 and 60 mTorr, corresponding to a C-doping concentration of approximately $5.3 \times 10^{19}, 2.5 \times 10^{20}\ and\ 8.3 \times 10^{20}\ cm^{-3}$ respectively. A multi-layered C-doping SIMS stack was grown and analyzed by SIMS in a separate study to determine C-concentration as a function of CBr_4 foreline pressure. AFM micrographs showing the surface morphology of ND1-ND3 are depicted in Fig. 2-8 below.

The AFM micrographs in Fig. 2-8 revealed that the surface V-defects return for high C-concentrations. Sample ND1, where C-doping was $5.3 \times 10^{19}\ cm^{-3}$, exhibited almost no V-defects however it can be seen that in certain regions, particularly where two adjacent

step meanders meet, there exists depressions which could potentially lead to the formation of V-defects had the GaN growth continued. It can be concluded that V-defects return for C-doping concentration in the range of $5.3 \times 10^{19} - 2.5 \times 10^{20}\ cm^{-3}$.

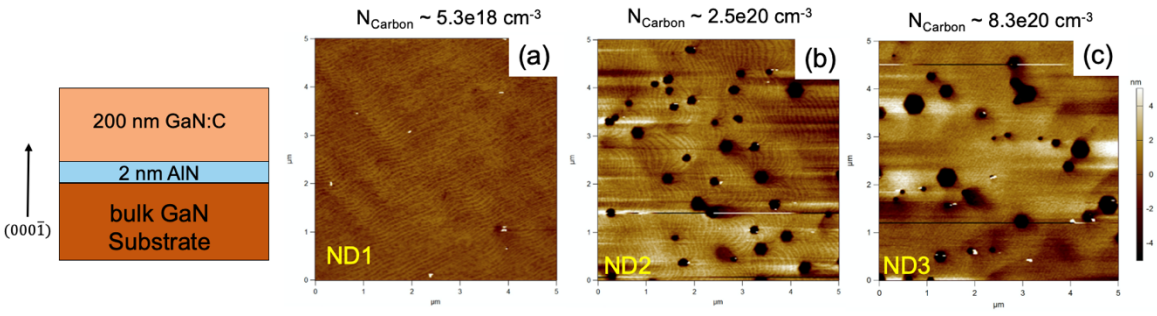

Figure 2-8: AFM scans taken for 200 nm GaN:C with carbon concentrations of (a) 5.3×10^{19} cm^{-3} for ND1 (b) 2.5×10^{20} cm^{-3} for ND2 and (c) $\mathbf{8.3 \times 10^{20}\ cm^{-3}}$ for ND3. Reprinted with permission from [59], Copyright Elsevier 2020.

The resurgence of V-defects at these high C-concentrations despite using the 2nm AIL provides an additional piece of evidence suggesting impurities play a role in the generation of V-defects. It may be speculated that impurities, or perhaps large clusters of impurities on the surface somehow induce a lower deformation potential leading to a strain field around the impurity (or impurity cluster) which result in the formation of a dislocation. As discussed in chapter 1, V-defects usually generate from dislocations. However, surface V-defects on N-polar GaN films can also be generated by other factors including surface defects, pre-existing dislocations, and slow-moving step meanders. However, given surface concentration of these V-defects was as high as 10^8 cm^{-2} (based on AFMs) and the underlying substrate had a TDD of 10^6 cm^{-2}, pre-existing dislocations cannot be the sole source of these V-defects. Deeper analysis of these V-defects and how the AIL suppresses them will require more in-depth characterization and analysis which was outside the scope of this work.

2.10 Conclusion

This work demonstrated smooth PAMBE-grown FS N-polar GaN, free of V-defects, by PAMBE using the AlN initiation layer or AIL. AlN's long history of being a reliable nucleation layer for heteroepitaxially matched with Al's higher bond energy with N over Ga suggests the AIL grows over defects and impurities on the substrate surface thereby creating a smooth surface for which subsequent N-polar GaN can be grown on. Thus, the AIL effectively decouples the epitaxially grown GaN from the substrate surface. High carbon doped films ($5.3 \times 10^{19} - 2.5 \times 10^{20}\ cm^{-3}$) grown on GaN with the AIL saw a resurgence of V-defects further supporting the hypothesis of impurities being responsible for V-defect generation. It was shown that thicker AILs, up to 6 nm, further improve film quality and surface morphology. It was also shown that an 8 nm AIL could be grown coherently strained to the GaN. Following the work presented in this study, Diez et al., demonstrated record high RT Hall mobility for an N-polar HEMT grown by PAMBE that utilized a 2 nm AIL [75]. The author hopes that the findings in this study will pave the way for PAMBE grown high-performance N-polar HEMTs on bulk GaN which will yield record high efficiencies.

3 Introduction to PAMBE Grown InGaN

For more than three decades Indium containing III-nitrides have been the subject of extensive study and have been proven commercially as an essential material for blue and white light emitting diodes (LEDs) and lasers [76]–[80]. The wide bandgap tunability of InGaN (0.7-3.4 eV) allows it to cover nearly the entire visible spectrum and deep into the infrared spectrum. Because of this there is interest in exploring longer wavelength (beyond blue and green) InGaN-based optoelectronics. Higher In-composition InGaN growth, however, presents several challenges which include, and are not limited to: high in-plane lattice mismatch (~11% for GaN and InN) [81], [82]; random alloy fluctuations due to the low miscibility of indium (In) in InGaN [81], [83]; high vapor pressure of indium [82]; and a lower decomposition temperature than what is traditionally used for GaN growth [84], [85]. This chapter is meant to address these issues and will serve as a primer on PAMBE growth of InGaN on planar GaN substrates. Much of what is covered in this chapter, such as phase

separation and critical thickness for relaxation, may apply to both MOCVD and MBE InGaN growth, however, the focus of this chapter is to better understand PAMBE InGaN growth. This will serve as a baseline for the following chapters which will focus on experimental results of InGaN grown on planar GaN and porous GaN tiles.

3.1 Low Temperature Growth

Unlike other alloys in the III-nitride system, InGaN growth is highly temperature sensitive. Typical GaN growth temperatures are approximately 1100 ℃ and 700 ℃ for MOCVD and PAMBE respectively. AlGaN can be grown at similar temperatures, or slightly higher, enabling the growth of high-quality AlGaN/GaN heterostructures as it is not necessary to interrupt growth to heat or cool the sample thereby simplifying the growth recipe. At these ideal growth temperatures however, In has a sticking coefficient of almost zero and will desorb from the surface before bonding with N adatoms. Furthermore, at higher temperature growth, InGaN may decompose due to the weaker In-N bond [86], [87] which has been shown to decompose at 630 ℃ under vacuum; GaN, on the other hand, will not start to decompose under vacuum until temperatures reach 850 ℃ or higher [88], [89]. A study conducted by G.T. Thaler et al., demonstrated thermal decomposition of 200 nm thick $In_{0.18}Ga_{0.82}N$ by post-situ thermal annealing at 950 ℃ for 15 minutes [87]. Comparing (0002) $\omega - 2\theta$ XRD scans for as-grown and annealed samples, it was found that the $In_{0.18}Ga_{0.82}N$ XRD peak for the annealed sample had significantly lower intensity compared to the as-grown sample (attributed to InN decomposition). Furthermore, both an In-droplet peak and Ga-droplet was observed in the (0002) $\omega - 2\theta$ XRD scan for the annealed sample indicating phase separation via thermal decomposition [87]. Therefore, unlike AlGaN and

GaN, InGaN must be grown at lower, less ideal, growth temperatures to avoid thermal phase separation and desorption.

Lower temperature PAMBE growth, which in this work we define to be 650 ℃ or lower, presents other challenges. Growing III-nitrides at lower temperatures reduces adatom mobilities on the film surface leading to subsequent issues such as step-bunching and 2D island growth [90]. Thermal energy is needed to increase adatom mobility such that adatoms may bond to optimum sites on the film surface. Without this thermal energy the surface will roughen [86], [91]. Furthermore, lower growth temperatures can lead to higher impurity incorporation from species such as oxygen which acts as a shallow donor in GaN [92]. As explained in chapter 1 growing under metal-rich conditions will help to alleviate some of these issues.

3.2 Phase Separation

A major issue with InGaN growth is the formation of microstructures or alloy de-mixing which arises from different types of phase separation. In this work we define phase separation as the occurrence of a non-uniform alloy composition in a single InGaN layer grown under constant growth conditions. Phase separation in III-nitrides takes three common forms: thermal decomposition (discussed above), spinodal decomposition, and indium surface segregation.

Spinodal decomposition occurs when one thermodynamic phase spontaneously separates into two phases due to fluctuations which reduces the free energy in the system [93]. For the case of InGaN growth, this translates to the spontaneous decomposition into

GaN and InN clusters. Spinodal decomposition is kinetically limited occurring primarily on the surface as bulk diffusion is usually low [83], [86]. Spinodal decomposition in InGaN growth has largely been attributed to the large miscibility gap of InGaN [81], [83] which itself is directly related to the large lattice mismatch between GaN and InN [81], [89]. While the standard phase diagrams for InGaN has been derived assuming a relaxed film, InGaN is typically grown coherently strained to GaN. S. Yu. Karpov used Valence Force Field approximation to model temperature vs. In-composition phase diagrams under different strain which showed a dramatic shift in the miscibility gap into the area of higher InN concentration for strained InGaN layers [94]. Furthermore, the characteristic symmetrical phase diagram for InGaN becomes asymmetrical (see figure 3-1 below) when taking strain into account [94][95]. This was also modeled by C. Tessarek et al., using thermodynamic analysis which showed that increasing strain of the InGaN layer, the critical temperature of spinodal decomposition decreases and shifts toward a higher In-composition [95]. Thus, the strain due to the lattice mismatch between GaN and InN suppresses spinodal decomposition due to composition pulling [83].

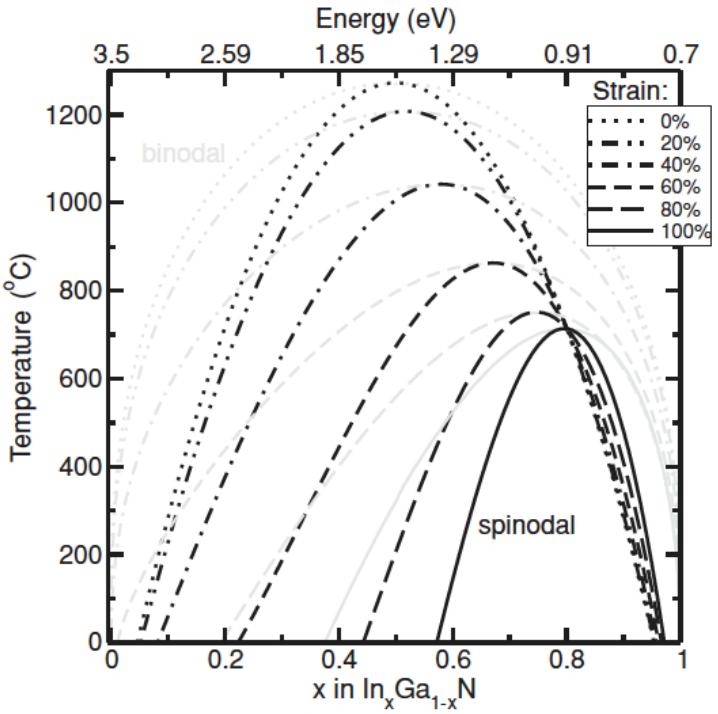

Figure 3-1: Temperature vs. In-composition phase diagram of ternary c-plane InGaN compounds for different values of relaxation. Reprinted with permission from [95], copyright American Physical Society (2011).

Indium surface segregation can be grouped into two categories: vertical indium surface segregation and lateral segregation of indium.

Vertical indium surface segregation is perhaps one of the more detrimental issues when trying to produce highly abrupt heterointerfaces. Because it is energetically favorable for Ga to occupy surface sites compared to In [96] a decrease in In incorporation can occur in the InGaN layers of an InGaN/GaN heterostructures. In InGaN/GaN MQW structures, delayed In incorporation from vertical indium surface segregation has been observed leading to "tailing" of In into the GaN and subsequent broadening of the photoluminescence peak [97], [98]. It has been shown that this effect can be mitigated by growing at higher growth temperatures, however, growing strained layers at higher

temperatures also leads to an increase in the Gibbs free energy leading to In desorption from the surface [98].

lateral segregation of indium occurs when In clusters form on the surface during growth. This can be explained by the higher stability of In-In bonds compared to In-Ga bonds [86], [99]. However, in extreme cases, these In-rich clusters can form quantum dots (QDs) on the surface thus becoming highly efficient radiative recombination centers [86], [100]. Unlike vertical In surface segregation which leads to a degradation in photoluminescence, lateral segregation of In can increase radiative recombination. Although lateral segregation of indium can be utilized for making QDs it can be problematic for other applications because of the composition non-uniformity on the surface. An accumulation of In on the surface due to the large miscibility gap between InN and GaN may also cause surface roughening [101]. This may be problematic in PAMBE growth which utilizes extremely high In-rich conditions. To mitigate this, metal-modulated epitaxy (MME) has been demonstrated as a feasible method to suppress In surface segregation by limiting how much of and how long the In-adlayer is on the surface [86], [102], [103]. L. Zhou et al., observed lateral phase separation for $In_{0.175}Al_{0.825}N$ grown on GaN in the form of honeycomb-like features with AlN-rich cores and InN-rich intercolumn boundaries [104]. It was found later by E. Ahmadi that these columnar structures in PAMBE-grown InAlN could be suppressed by growing at higher temperatures and higher In-flux [105].

3.3 Plastic Relaxation

For an epitaxial film grown on a rigid substrate in which there is an in-plane lattice mismatch between the film and the substrate, there exists a maximum thickness for which the film will remain 100% coherently strained to the substrate. When such a pseuodomorphic layer is grown in the Frank-van der Merwe (FM) or layer-by-layer growth mode, the in-plane lattice constant is initially the same as that of the substrate and the out-of-plane lattice constant changes due to in-plane deformation ('Poisson' effect). The strain energy per unit area E_h of the strained film can be expressed from elastic continuum theory [106]–[108]:

$$\boldsymbol{E_h = \sigma_x \epsilon h} \tag{3.1}$$

Where ϵ is the in-plane strain from the lattice mismatch, h is the layer thickness, and σ_x is the in-plane misfit stress given by:

$$\boldsymbol{\sigma_x = 2G(1+\upsilon)\epsilon/(1-\upsilon)} \tag{3.2}$$

Where G is the shear modulus, and υ is the Poisson ratio. From equations 3-1, as the film thickness h increases there is a corresponding buildup of strain energy. At some critical thickness (h_c) strain energy is released through deformation. The deformation which occurs as a result of this release in strain energy manifests as misfit dislocations (MD) which are local regions of lattice misregistry [109]. h_c is dependent on a variety of factors such as crystal structure, growth conditions, and the presence of pre-existing dislocations.

Methods for determining h_c

Consider Fig. 3-2 where a pre-existing TD terminated at the interface of the substrate and the pseudomorphic layer glides along the growth interface via the force from the strain energy of the top layer. The glide of the TD segment is opposed by both the Peierls Force and the line tension of the TD. As the thickness of the pseudomorphic layer increases so does the strain energy (as predicted by equation 3.1). h_c is defined as the thickness for which the force from the strain energy of the pseudomorphic layer is equal to the sum of the force from the line tension and Peierls Force of the TD and a MD is generated [109]. One of the early theoretical models for obtaining h_c of a semiconductor epitaxial film is the Matthews-Blakeslee model [110]. For Matthews-Blakeslee h_c is calculated by equating the force exerted by the misfit strain F_ϵ to double the force from the line tension F_l ($F_\epsilon = 2F_l$) where:

$$\boldsymbol{F_\epsilon = \frac{2G(1+v)}{(1-v)} bh\epsilon cos\lambda} \quad 3.3$$

$$\boldsymbol{F_l = \frac{Gb^2(1+v)}{4\pi(1-v)}((1 - vcos^2\alpha)(ln\frac{h}{b} + 1))} \quad 3.4$$

Where λ is the angle between the slip direction and the direction in the film plane that is perpendicular to the line of intersection of the slip plane. α is the angle between the dislocation line and the Burgers vector b. Setting $F_\epsilon = 2F_l$ using equations 3.3:

$$\boldsymbol{h_c = \frac{b}{2\pi f}\frac{(1-vcos^2\alpha)}{(1+v)cos\lambda}(ln\frac{h_c}{b} + 1)} \quad 3.5$$

Where f is defined as $2\epsilon_{max}$ or twice the maximum value of strain that a layer can have before relaxation. Another model by R. People and J.C. Bean proposes MDs will be generated when the real strain energy density of the film exceeds the energy density

associated with the formation of a screw dislocation at a distance from the free surface equal to the film thickness [111] and is given by:

$$\boldsymbol{h_c \simeq \left(\frac{1-v}{1+v}\right)\left(\frac{1}{16\pi\sqrt{2}}\right)\frac{b^2}{a(x)}\left[\left(\frac{1}{f^2}\right)ln\left(\frac{h_c}{b}\right)\right]} \quad 3.6$$

Where a(x) is the bulk lattice constant of the pseudomorphically grown film where 'x' denotes the alloy composition. This model was found to be accurate [111] for $Si/Si_{1-x}Ge_x$ films grown by MBE in reference [112]. A. Fischer et al., proposed a method for calculating h_c by satisfying free surface boundary conditions by placing an "image dislocation" outside the crystal in such a manner that its stress field cancels that of the real misfit dislocation at the surface. This creates an equilibrium theory which correctly predicts h_c for $Si/Si_{1-x}Ge_x$ structures [113]. The 'image dislocation' model proposed by Fischer et al., was modeled for InGaN on GaN and found to be quite accurate when compared to actual MOCVD grown InGaN on low TDD GaN substrates for In-compositions ranging from 5-16% [114].

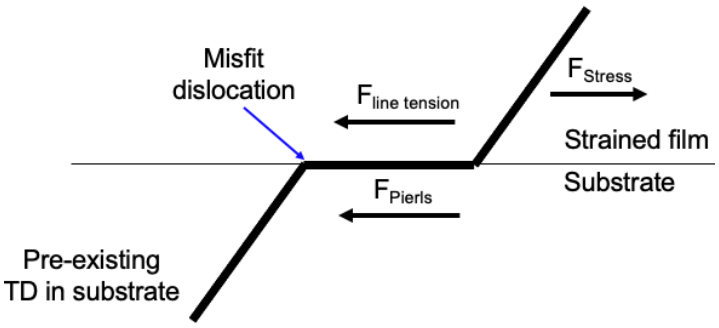

Figure 3-2: Illustration showing how a pre-existing threading dislocation segment in the substrate will extend along the growth interface (glide) aided by the force from the energy of the strained layer. The Peierls force and line tension of the dislocation oppose this force.

The Matthews-Blakeslee Model [110], People and Bean Model [111], and the Image Model proposed by A. Fischer [113] all work well for diamond or zincblende semiconductors such as the GaAs/AlGaAs or Si/SiGe systems where the crystal structure is isotropic and it

can be assumed that all of the components of the elastic tensors are equal. Because these models assume a centrosymmetric crystal structure, utilizing them in wurtzite $In_xGa_{1-x}N$/GaN (non-centrosymmetric structure) usually results in an h_c as a function of In-composition which is larger than what is found experimentally [114]. Furthermore, the primary slip system in wurtzite is $\langle 11\bar{2}0\rangle\{0002\}$ which inactive since it lies perpendicular to the growth direction [115]. Freund and Suresh proposed the Energy Balance Model to calculate h_c which takes into account the hexagonal symmetry of the wurtzite system [116]. D. Holec et al., used this method to calculate $h_c(x_{In})$ for InGaN grown on GaN [114] which was slightly lower compared to experimental work done in another study where InGaN was grown on low TDD GaN-on-sapphire substrates by MOCVD [117], however it was significantly lower than what had been calculated by People and Bean [111].

It is important to note that h_c has a major dependence on growth temperature. At low temperatures growth, where impinging atoms are unable to move in a correlated manner to reach the free-energy minimum surface, the in-plane lattice constant of the pseudomorphic film will remain matched to the substrate for much higher thicknesses and In-compositions [118]. This makes low-temperature PAMBE growth desirable for growing thick strained InGaN on GaN. E. A. Clinton et al., demonstrated strained $In_{0.2}Ga_{0.8}N$ on GaN with thicknesses well beyond the predicted theoretical predictions for h_c by growing at ultra-low temperatures under N-rich conditions by PAMBE. It was assumed that this delay in relaxation was related to dislocations not being able to move because of ultra-low temperatures [102].

Relaxation mechanisms and how they affect surface morphology and film quality is, like h_c, dependent on growth conditions. As mentioned previously, V-defects tend to form for relaxed InGaN grown at high temperatures by MOCVD [119] and MBE [120]. No matter the growth conditions, relaxation of InGaN on planar GaN is usually accompanied by some type of surface roughening. A study conducted by H. Wang et al., involved growing three samples at different $In_{0.1}Ga_{0.9}N$ thicknesses (50 nm, 100 nm and 450 nm) by MOCVD and characterizing surface morphology and film quality [121]. 100 nm of $In_{0.1}Ga_{0.9}N$ has been shown experimentally to be close to or slightly above the h_c [114]. In the study by Wang et al., the surface morphology of the 50 nm layer showed spiral step-flow morphology and an XRD (0002) rocking curve FWHM comparable to the GaN substrate (3.2 arcminutes). The 100 nm layer resulted in a slightly higher XRD (0002) rocking curve FWHM (6.2 arcminutes) with some V-defects on the surface, however TEM results showed that the V-defects formed around pre-existing TDs and there were no new dislocations at the InGaN/GaN interface. The 450 nm layer, which was found to be 100% relaxed, had an XRD (0002) rocking curve FWHM of 14.7 arcminutes (almost 4x that of the 50 nm layer) and a surface morphology covered in very large V-defects and a high density of dislocations from the growth interface seen by TEM [121]. In the case of the 100 nm InGaN layer in that study ([121]) elastic relaxation via V-defect formation occurred which alleviated strain – an effect which has been observed in other cases [119], [122]. V-defects are an easy way to monitor whether relaxation has occurred for MOCVD grown InGaN layers, however, for low temperature MBE growth this is not necessary the case. Hestroffer et al., grew thick relaxed compositional graded $In_{0.1}Ga_{0.9}N$ layers on planar GaN which exhibited the same spiral

surface morphology observed for thin strained films [123], [124] even though TEM results revealed a high density of dislocations generated from relaxation of the InGaN layer [124]. For InGaN layers grown at thicknesses close to h_c other surface features, such as cross-hatching have been observed by AFM [125], [126]. S. Srinivasan et al., demonstrated that for InGaN grown on low TDD substrates with thickness above h_c calculated from the Matthews-Blakeslee model, the generation of MD activated the secondary slip system $\{11\bar{2}2\}\langle 11\bar{2}3\rangle$ which caused dislocations to glide to the surface resulting in line segments on the surface parallel to the $\langle 1\bar{1}00\rangle$ direction [117]. This was also observed in another study by TEM for 100 nm layers of $In_xGa_{1-x}N$ on low TDD GaN for In-compositions x_{In} > 11% [115]. This 'punch out' theory arising from the activation of these secondary slip systems is illustrated in Fig. 3-3.

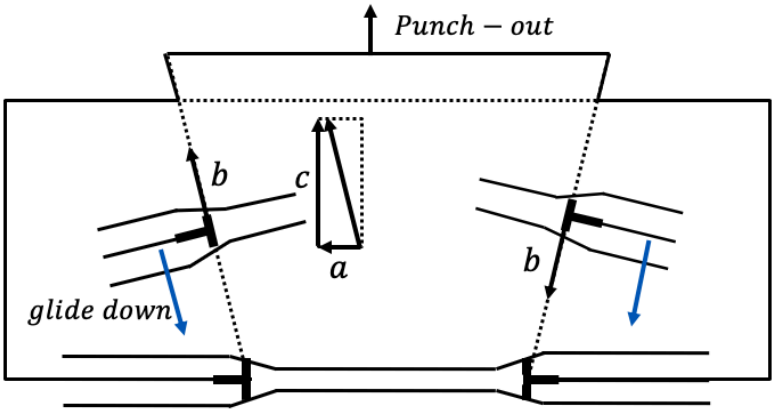

Figure 3-3: Punch out effect for InGaN grown on GaN where the secondary slip system $\{11\bar{2}2\}\langle 11\bar{2}3\rangle$ is activated from plastic deformation leading to a displaced section of the InGaN layer. Adapted from reference [125].

3.4 PAMBE Growth of InGaN

Before going into a detailed experimental study of MBE InGaN grown on planar GaN, such as what will be presented in the following chapter, it is necessary to understand the basics of PAMBE InGaN growth and how it differs to the more conventional MOCVD growth technique.

Cell flux:

With respect to other alloys, different cell fluxes play different, but equally important roles in InGaN growth by PAMBE. For growing thin layers of AlGaN by PAMBE, for example, one can use the same growth conditions used for GaN growth and simply vary Al-flux to get the desired Al-composition. This is because the Al-N bond has a higher bond energy compared to the Ga-N bond. Thus all the Al adatoms absorbed on the surface will bond to N sites before any of the Ga adatoms incorporate [68]. Ga, therefore, becomes a surfactant (explained in chapter 1) in that is modifies the surface energy such that step-flow growth can occur while also incorporating into the film. This is demonstrated experimentally in figure 3-4 where an increase in Al-flux leads to a linear increase in Al-composition. For InGaN growth by PAMBE, however, this is not the case. There are two fundamental issues which impede InGaN growth under the same conditions as GaN: firstly, explained above, In will not incorporate at the typical growth conditions used for GaN (~700 °C); secondly, Ga atoms have a higher affinity to bond with N compared to In. In will not incorporate when growing in the presence of excess Ga [85]. Thus, for InGaN growth by PAMBE the following conditions must be satisfied:

$$\boldsymbol{\phi_{Ga} < \phi_N < \phi_{In}} \quad 3.7$$

Where $\phi_{Ga}, \phi_N, and\ \phi_{In}$ are defined as the incident fluxes impinging on the surface during growth for Ga, N and In respectively. From equation 3.7 Ga is the limiting reactant and thus has the greatest effect on growth rate, and to a lesser extent In-incorporation. Active N-flux determines the In-composition whereas incident In-flux acts as an auto-surfactant providing a source of In for incorporation while simultaneously acting as an adlayer to promote step-flow growth [9]. Therefore In-flux in InGaN growth plays the same role as Ga-flux in GaN and AlGaN growth. InGaN growth by PAMBE involves growing N-rich GaN with excess In on the surface. Fig. 3-5 below shows a surface structure diagram adapted from reference [127] showing In-flux as a function growth temperature indicating the N-rich regime, the intermediate regime and the In-droplet regime for InGaN growth by PAMBE. Clearly from Fig. 3-5 at lower growth temperatures the intermediate regime shrinks and it becomes easier to go straight from the N-rich regime to the In-droplet regime. The curve separating the In-droplet regime from the intermediate regime is exponential because desorption of In as a function of surface temperature is exponential. As you go higher and higher in temperature an exponential increase in In-flux will be needed to stay in the In-droplet regime.

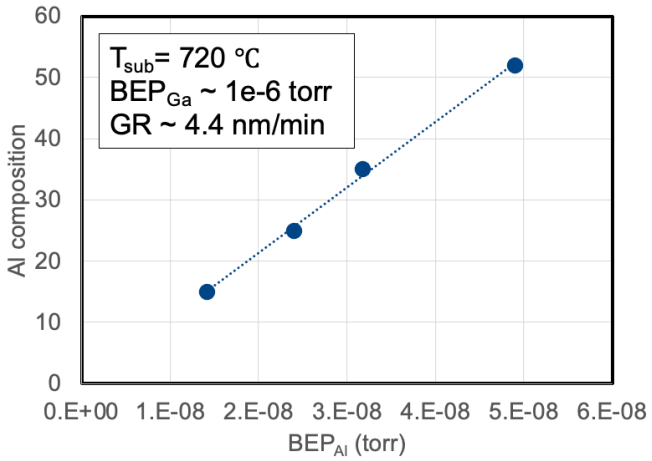

Figure 3-4: Al-composition extracted from (0002) ω-2θ XRD scans for approximately 30 nm of AlGaN grown on GaN templates with varying Al flux by PAMBE under typical GaN growth conditions (growth conditions shown in inset). A clear linear trend is observed for Al-composition as a function of Al-flux.

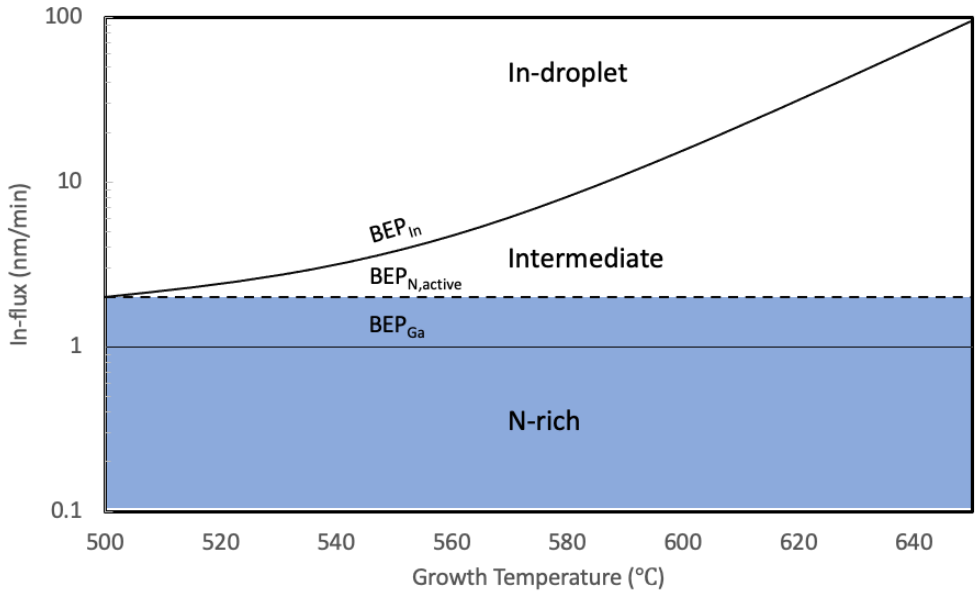

Figure 3-5: Surface structure diagram indicating the N-rich, intermediate, and In-droplet growth regimes for InGaN using a constant Ga and active N-flux. In-flux is given by the solid curved line, active N-flux is given by the dotted black line and Ga-flux is given by the solid thin black line. This plot is adapted from Poblenz, (2005) [127]

3.5 Growth Temperature and In-Composition

Like MOCVD, PAMBE grown InGaN composition is highly temperature dependent due to the decomposition of In-N bonds. Unlike MOCVD growth, however, which occurs close to atmospheric conditions, MBE growth is performed in an ultra-high vacuum

environment. As mentioned earlier, In-N bonds will fully decompose at 650 ℃ under vacuum, however, some In-N bonds will be begin to decompose, or not form at all, at approximately 565 ℃ under vacuum [128]. In-N will continue to decompose as the temperature is raised until there is no In-incorporation at all resulting in GaN grown in excess In. C. Adelmann et al., demonstrated this early on by showing a clear linear decrease in In-composition for temperatures ranging from 565 ℃ to 620 ℃ [128]. This was also demonstrated by C. Skierbiszewski et al., where temperature was varied from 520 ℃ to approximately 580 ℃, without changing any other conditions to go from $In_{0.28}Ga_{0.72}N$ to $In_{0.2}Ga_{0.8}N$ [9]. It is possible to control In-composition by adjusting Ga-flux, however from Eq. 3.7 this will also affect growth rate (Ga is the limiting reactant). Controlling active N-species can also control In-composition, however, in PAMBE it is sometimes not ideal to change active N-flux because it may mean deviating from already well calibrated and ideal plasma conditions. Substrate temperature, on the other hand, can be a means to control In-composition within an acceptable range of In-compositions without necessarily affecting other parameters.

3.6 Conclusion

Whether by MBE or MOCVD InGaN growth possesses many challenges. Issues such as phase separation, degradation of film quality due to low temperature growth and relaxation all need to be addressed when choosing growth conditions for a specific In-composition and thickness. The high vapor pressure of In means InGaN growth must be carried out at lower than ideal temperatures. In-rich PAMBE growth at low temperatures

has the advantage growing thicker films at higher In-compositions without generating V-defects on the surface and even suppresses plastic deformation. For PAMBE growth, In-composition can be effectively controlled via active N-flux or growth temperature whereas Ga-flux, being the limiting reactant, should in theory be used to tune growth rate within a certain range of In-compositions. Experimental results presented for InGaN grown on planar GaN in the following chapter will demonstrate the topics covered in this chapter.

4 PAMBE InGaN Growth on Planar GaN

4.1 Introduction

Given the many challenges associated with InGaN growth discussed in the preceding chapter, an extensive growth campaign is needed to establish the optimum growth conditions for device quality InGaN. In this chapter, several PAMBE InGaN growth studies on planar GaN-on-sapphire substrates are presented to observe how temperature, In-flux, Ga-flux, N-flux and thickness affect In-composition, growth-rate, film quality and surface morphology. Much of the data in this chapter will help support the InGaN growth primer given in the preceding chapter including some observations which were not. The results from this chapter will serve as a baseline for the following chapter which will involve PAMBE InGaN growth on porous GaN tiled substrates which promote elastic relaxation.

4.2 Experimental Details

GaN and InGaN growth by PAMBE in this chapter was carried out in a Varian Gen 2 system with conventional high-flux Ga and In effusion cells. The background pressure of the growth chamber was in the low 10^{-10} torr in the absence of cell-flux and N_2 gas. Active nitrogen was supplied by 1 sccm of 99.9995% pure N_2 via a VEECO Unibulb RF plasma source powered at 300 watts. It should be noted that the plasma source in this study differs from the one used in chapter 2 for the N-polar GaN study which utilized a high-flux plasma source. Background pressure in the chamber during growth was approximately 1×10^{-5} torr. The growth surface was monitored in-situ by RHEED to analyze the surface before, during and at the end of growth. The optical pyrometer used on this system is not suited for the low temperatures used for InGaN growth in this study therefore all temperatures recorded in this study were taken from the thermocouple attached to the back of the substrate heater which will be referred to as the car temperature (T_c). To separate the InGaN from the regrowth interface all growths in this study were initiated with GaN grown at 720 °C under Ga-rich conditions**.** For the initial high-temperature GaN growth, a Ga-flux of approximately 1.7×10^{-6} torr was used. Prior to the start of growth, the samples were brought up to the GaN growth temperature and the surfaces were exposed to Ga flux for 30 seconds followed by thermal desorb as observed by RHEED intensity. Following initial GaN growth, the substrate temperature was lowered for InGaN growth. Following InGaN growth, the sample was capped with a thin layer (1.5-6 nm) of GaN grown at the same temperature as the InGaN layer. There were no growth interruptions during the InGaN growth for desorption of excess metal.

The surface morphology of every sample was characterized post-growth by AFM using an Asylum MFP3D. Off-axis, $\{\bar{1}\bar{1}24\}$ reflection, XRD $(\omega - 2\theta) - \omega$ RSM scans were carried out on certain samples to determine relaxation and In-composition. Other samples were only characterized by (0002) XRD $\omega - 2\theta$ scans to extract In-composition, thickness and rocking curve FWHM values.

4.3 In-Flux Study (IA)

It is necessary to begin any InGaN study by properly dialing in the right In-flux such that growth is occurring under In-rich conditions, i.e satisfying equation 3.7. Alternatively, In-flux must not be too high such that In-droplets accumulate on the surface – an effect which may negatively impact surface morphology. In this study, four growths were carried with varying In-flux and characterized by AFM and XRD (0002) $\omega - 2\theta$ scans to observe surface morphology and In-composition respectively. Substrate temperature and Ga-flux were kept constant at 550 °C and 7e-8 torr respectively. The active N-flux for this study corresponded to a growth rate of approximately 4 nm/min determined from GaN growth rate calibrations carried out in a separate study. The InGaN layers were grown for 1 hour before being capped with 2 nm of low-temperature GaN for thermal desorption of excess In. In-flux for each growth was 7.25e-7 torr, 6.18e-7 torr, 4.63e-7 torr, and 2.87e-7 torr for samples names IA1, IA2, IA3 and IA4 respectively. Table 4-1 below summarizes the data for the In-BEP study. Fig. 4-1 shows In-composition as a function of In-flux. (0002) $\omega - 2\theta$ XRD scans for each run are displayed in the top left inset of the Fig. 4-1 plot. 10x10 μm^2 AFM images taken for each run are shown in Fig. 4-2 below. The surface RMS values extracted

from AFM were found to be 1.76 nm, 1.68 nm, 2.05 nm and 5.64 nm for IA1, IA2, IA3 and IA4 respectively. Data from this study is also shown in table 4-1.

Table 4-1: Data for In-flux study (IA1-4) showing In-composition and surface RMS values extracted from the AFMs in Fig. 4-2.

Sample name	BEP_{In} (torr)	x_{In} (%)	RMS (nm)
IA1	7.25e-7	7.2	1.76
IA2	6.16e-7	4.7	1.68
IA3	4.63e-7	<1	2.05
IA4	2.87e-7	0	5.64

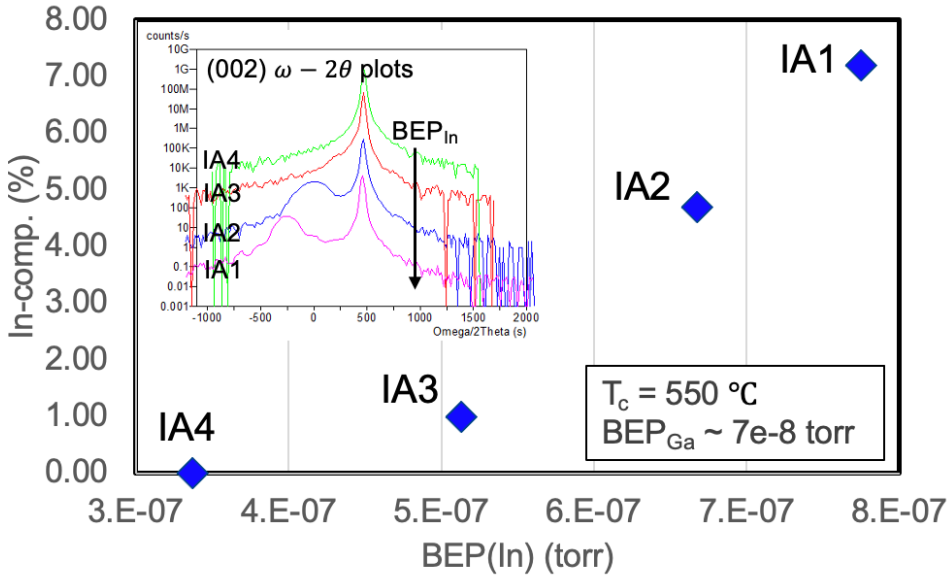

Figure 4-1: Plot of In-composition as a function of In-flux for four growths. Top left inset shows (0002) ω-2θ XRD scans for each sample where InGaN composition was extracted. Bottom right inset displays the substrate temp and Ga-flux (BEP_{Ga}) which were kept constant across the four growths.

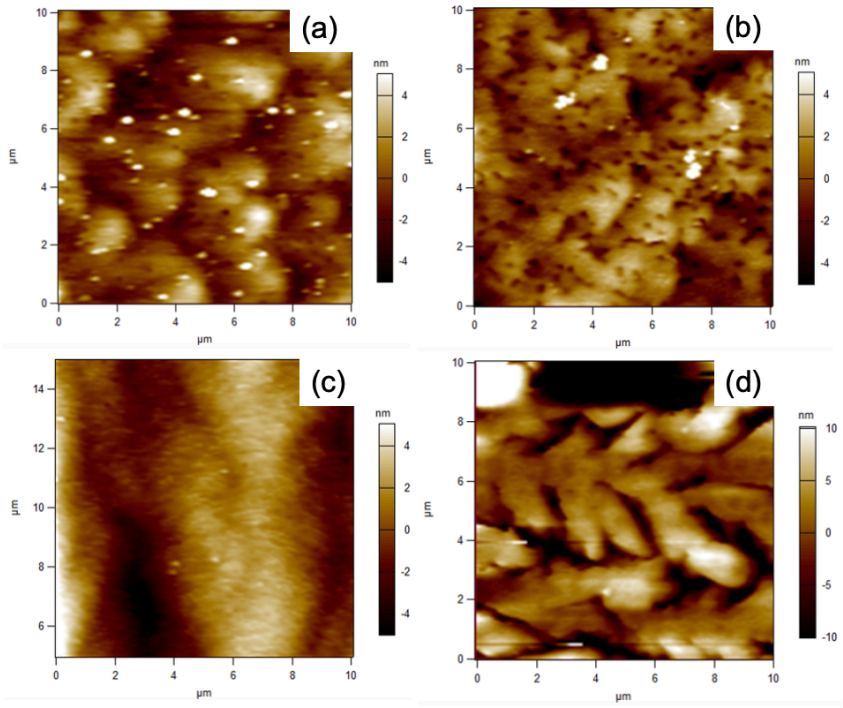

Figure 4-2: AFM micrographs taken for samples (a) IA1, BEP_{In} = 7.25e-7 torr leading to $In_{0.072}Ga_{0.0928}N$ grown in the In-rich regime. The white dots on the surface are likely to be In-droplets. (b) IA2, BEP_{In} = 6.16e-7 torr leading to $In_{0.047}Ga_{0.0953}N$ grown under slightly N-rich conditions leading to a pitted surface. (c) IA3, BEP_{In} = 4.63e-7 torr leading to low temperature GaN grown under N-rich conditions with excess In on the surface acting as a surfactant. (d) IA4, BEP_{In} = 2.87e-7 torr leading to N-rich GaN growth with rough surface morphology.

Considering In-composition vs. BEP_{In} shown in table 4-1 and Fig. 4-1, there is a clear increase in In-composition as a function of In-flux. Comparing the (0002) $\omega - 2\theta$ XRD scans for IA1 and IA2 shown in the inset of Fig. 4-1, IA1 had an In-composition of approximately 7.2% and IA2 had an In-composition approximately of 4.7%. Estimating the thickness from the few visible thickness fringes to the left of the InGaN peak on IA1 from Fig. 4-1, the growth rate was approximately 1.3 nm/min. There were no thickness fringes observed in any of the other (0002) $\omega - 2\theta$ XRD scans shown in Fig. 4-1 and therefore the thickness of the other three samples is unknown. Interestingly, the InGaN peak for IA2 (BEP_{In} = 6.16e-7 torr) is significantly broader than that of IA1 (BEP_{In} = 7.25e-7 torr). A broader alloy peak in a XRD rocking curve scan points to issues with the film quality. This is to be expected as

there is not enough In to induce a proper In-adlayer. The AFM micrographs in Fig. 4-2 give a more thorough understanding of what is happening. The AFM micrograph in Fig. 4-2.a for sample IA1 (BEP_{In} = 7.25e-7 torr) shows spiral surface morphology consistent with low-temperature In-rich InGaN growth and was therefore grown with the ideal InGaN growth conditions satisfying equation 3.7. Fig. 4-2.b for sample IA2 (BEP_{In} = 6.16e-7 torr) has a high density of V-pits on the surface. Judging from this surface morphology and the lower In-composition compared to IA1 (BEP_{In} = 7.25e-7 torr), it can be concluded that IA2 was grown such that $\phi_{Ga} < \phi_{In} < \phi_N$. In this N-rich regime, without a sufficient In-adlayer on the surface, adatom mobility decreases thereby impeding step-flow growth resulting in the pitted surface morphology shown in Fig. 4-2.b. The broad InGaN peak seen in the (0002) $\omega - 2\theta$ XRD scan in the inset of Fig. 4-1 also supports this. Going to even lower In-flux, for sample IA3 (BEP_{In} = 4.63e-7 torr) In-composition is less than 1% (table 4-1) however, the surface morphology shown in Fig. 4-2.c shows clear step-flow morphology. This points toward GaN grown in the presence of an In-surfactant such that $(\phi_{Ga} + \phi_{In}) > \phi_N$. Using In as a surfactant enables the growth of GaN at lower than optimum temperatures [129]. The sample with the lowest In-flux (BEP_{In} = 2.87e-7 torr) IA4 had no In-incorporation (see Fig. 4-1) and significantly poorer surface morphology compared to IA3 (see Fig. 4-2.d). This surface morphology for IA4 suggests N-rich GaN growth such that $(\phi_{Ga} + \phi_{In}) < \phi_N$, that is, there is not sufficient metal to form an adlayer which will promote step-flow growth leading to the finger-like trench features observed in Fig. 4-2.d. Based on these observations, the approximate location of where each growth is in the InGaN structure diagram can be made which is shown in Fig. 4-3.

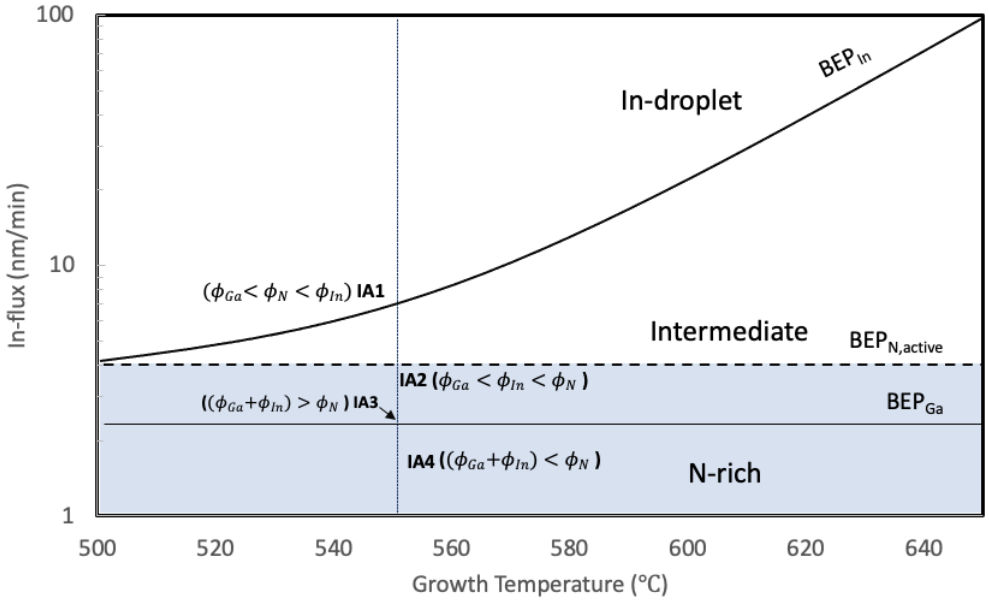

Figure 4-3: Surface structure diagram showing the estimated location of IA(1-4).

This study demonstrates how to determine the appropriate In-flux needed to grow quality InGaN at a set growth temperature, Ga-flux, and active N growth rate. From XRD and AFM analysis it was determined that for $In_{0.072}Ga_{0.0928}N$ growth at 550 °C, a N-flux of ~4 nm/min and a Ga-flux ~ 7e-8 torr, an In-flux of 7.25e-7 torr places the growth in the droplet-regime of the surface structure diagram shown in Fig. 4-3. These growth conditions will serve as a baseline for the subsequent studies shown below.

4.4 Ga-Flux Study (IB)

Under the conditions used in the In-flux study, the InGaN growth rate was only 1.3 nm/min. Explained previously, in the case of PAMBE InGaN growth Ga is the limiting reactant and thus determined the growth rate. This however is only true if the impinging Ga-flux that incorporates is less than the active N-flux ($\phi_{Ga} < \phi_N$). In the following study five growths are carried out with varying Ga-fluxes to observe growth rate, In-composition,

and surface morphology. In-flux was kept constant at approximately 7e-7 torr – slightly lower than what used in the previous study so to suppress In-droplet size and surface density. Substrate temperature was kept constant at 550 ℃. This high temperature limits In-incorporation, however it is necessary when trying to extract thickness from (0002) $\omega - 2\theta$ XRD scans; higher temperature growth yields the best film quality and thus the most defined thickness fringes from XRD. Going to lower temperatures degrades the film quality such that thickness fringes cannot be observed to extract growth rate. Table 4-2 below shows the data from this study.

Table 4-2: Data summary for the IB1-4

Sample name	BEP_{Ga} (torr)	Growth time (hh:mm)	x_{In} (%)	t_{InGaN} (nm)	Growth rate (nm/min)	RMS (nm)
IB1	2.86e-8	03:00	9.3	88	0.49	0.25
IB2	3.34e-8	0:40	10	26	0.65	-
IB3	4.76e-8	0:40	8	36	0.90	0.55
IB4	5.69e-8	0:40	8.8	44	1.10	-
IB5	7.12e-8	0:40	7.9	58	1.45	1.05

Knowing the growth with the lowest Ga-flux would yield an ultra-low growth rate, the first sample, IB1 with the lowest Ga-flux (2.86e-8 torr) was grown for 3 hours while the rest of the samples in this study had only 40-minute growth times.

Fig. 4-4 below shows a plot of growth rate and In-composition as a function of Ga-flux. Clearly there is a linear increase in growth rate as a function Ga-flux (red circle data points) which supports equation 3.7 in that Ga is the limiting reactant. The somewhat less

linear, and unrepeatable decrease in In-composition as a function of Ga-flux (blue diamond data points) points to the fact that increasing Ga-flux also increases Ga-incorporation - Ga will always displace In [85]. However, given the erratic trend of In-composition as a function of Ga-flux, it can also be speculated that at these growth conditions Ga-flux ought not be used to control In-composition, although it is very effective in controlling growth rate. Assuming the In-composition trend in Fig.4-4 is not decreasing but is in fact just run-to-run variation, that would mean the In-composition has a deviation of +/- 1.05 point-% across these different growth rates. This deviation is in-agreement with appendix A.1 which shows In-composition over time.

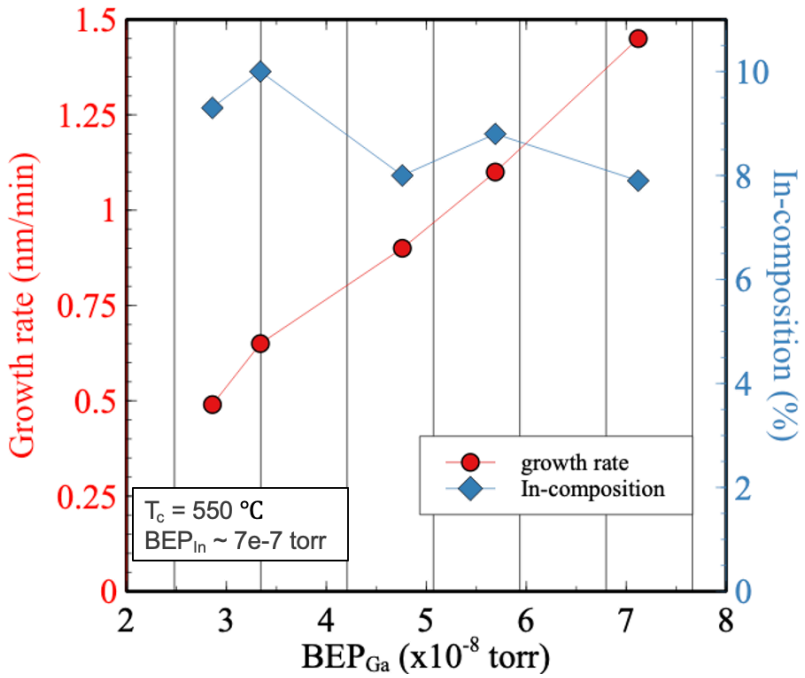

Figure 4-4: Plot of experimental data for the IB1-5 series showing growth rate (left vertical axis in red) and In-composition (right vertical axis in blue) as a function of Ga-flux.

In addition to XRD, AFM was carried out on 3 of the samples from this study: IB1 (2.86e-8 torr, t_{InGaN} ~ 88 nm, GR ~ 0.49 nm/min), IB3 (4.76e-8 torr, t_{InGaN} ~ 36 nm, GR~0.9

nm/min) and IB5 (7.12e-8 torr, t_{InGaN} = 58 nm, GR~1.45 nm/min) to see how growth rate affects surface morphology (see Fig. 4-5). Although the samples vary in thickness some speculation can be made about how growth rate affects surface morphology. RMS values extracted from the AFM scans were found to be 0.253 nm, 0.55 nm and 1.05 nm for IA1, IA3 and IA5 respectively.

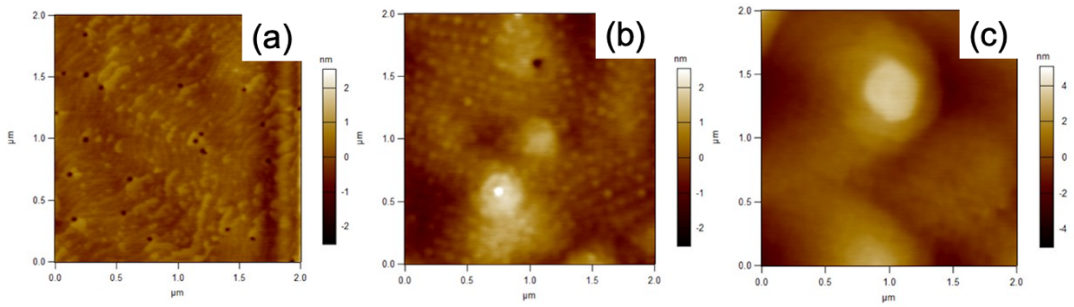

Figure 4-5: AFM height scans for (a) IB1, where BEP_{Ga} = 2.86e-8 torr, t_{InGaN} ~ 88 nm, GR ~ 0.49 nm/min, (b) IB3, where BEP_{Ga} = 4.76e-8 torr, t_{InGaN} ~ 36 nm and GR ~ 0.9 nm/min, and (c) IB5, where BEP_{Ga} =7.12e-8 torr, t_{InGaN} = 58 nm, GR~1.45 nm/min. RMS vales extracted from these scans were found to be 0.253 nm, 0.55 nm and 1.05 nm for IA1, IA3 and IA5 respectively.

Considering the AFM results from Fig. 4-5, there is an obvious increase in RMS roughness due to spiral height as a function of growth rate. The sample that has the lowest growth rate (IB1 which also has the thickest InGaN layer) has the smoothest surface morphology with no sign of spiral growth around dislocations. The AFM scans for IB3 and IB5, on the other hand, have large spirals and thus rougher surface morphology despite having around half the thickness as IA1. Lowering the growth rate for growing any film allows adatoms on the surface longer time to find two-dimensional step edges resulting in better film quality [130]. For this reason it is common for LED MQWs to be grown at lower growth rates than those used for bulk InGaN growth [130].

4.5 Temperature Controlled In-composition (IC)

At the low temperatures employed by PAMBE InGaN growth, In adatom desorption from the surface can be neglected, however, In-N decomposition and restriction of In-N bond generation, both of which are both highly temperature dependent, cannot be neglected. As was explained in chapter 3, in the case of InGaN growth, there is a continuous battle between the impinging In-flux and the decomposition of In-N bonds. The impinging In-flux must be greater than the sum of In thermally desorbing from the surface and the decomposing In-N bonds for In to incorporate. Thus, adjusting substrate temperature can be an effective way to control In-composition within a given composition range. Provided equation 3.7 is satisfied, ϕ_N should also limit how much In incorporates. However, active N-flux is determined by well calibrated plasma conditions which are not always ideal to change between growths. Temperature controlled In-composition has already been used extensively by both MOCVD [131] and MBE [127]. Therefore, it is necessary to conduct a study on how substrate temperature affects In-composition.

Four growths were carried out in this study labeled IC1-4 which were grown at a substrate temperature of 540 ℃, 550 ℃, 560 ℃ and 570 ℃ respectively. Cell fluxes for all samples in this study were grown satisfying the conditions in equation 3.7 (i.e. N-rich GaN grown in In-excess). Ga-flux in this study was kept constant at 9.9e-8 torr corresponding to a growth rate of approximately 2 nm/min. Growth time for each sample was 30 minutes resulting in a film thickness of approximately 60 nm. After capping the samples with 1.5 nm of GaN, excess In was thermally desorbed by bringing the substrate temperature up to

630 ℃ until a saturation in RHEED intensity was observed. Growth temperature, x_{In} extracted from XRD, and surface RMS values extracted from AFM are given in table 4-3. The In-compositions extracted for samples IC1-4 were found to be 14.5%, 11.2%, 8% and 4.5% respectively. The RMS values extracted from AFM for samples IC1-4 were found to be 0.6, 0.7, 0.58 and 0.57 nm respectively.

Table 4-3: Experimental data for IC1-4 showing substrate temperature, In-composition extracted from (0002) ω-2θ XRD scans, and surface RMS extracted from AFM.

Sample name	T_c (℃)	x_{In} (%)	RMS (nm)
IC1	540	14.5	0.6
IC2	550	11.2	0.7
IC3	560	8.0	0.58
IC4	570	4.5	0.57

The AFM scans for the temperature series IC1-4 are shown in Fig. 4-6 below. The AFM image for the sample grown at the highest growth temperature (IC4 grown at 570 ℃) which resulted in 4.5% In-composition, had step-flow surface morphology similar to high-temperature GaN growth. Some small craters were observed on the surface of IC4 (see Fig. 4-6.d) which may be from desorbed In-droplets. As the temperature was decreased to 560 ℃ and 550 ℃ (IC3 and IC2 respectively), resulting in 8% and 11.2% In-composition respectively, the surface morphology became more spiral-like consistent with low-temperature growth. At the lowest growth temperature, IC4 grown at 540 ℃, which resulted in 14.5% In-composition, the spiraling step terraces become grainier. The degradation in surface morphology with lower growth temperature, resulting in higher In-

composition, can be explained by the lower surface adatom mobility which results from growing at lower temperatures. Explained in chapter 3, the droplet craters seen on the sample grown at the highest substrate temperature (IC4) may be the result of surface In-segregation, resulting in clusters of In or In-N which thermally desorb at the end of growth leaving behind the craters seen in Fig. 4-6.d.

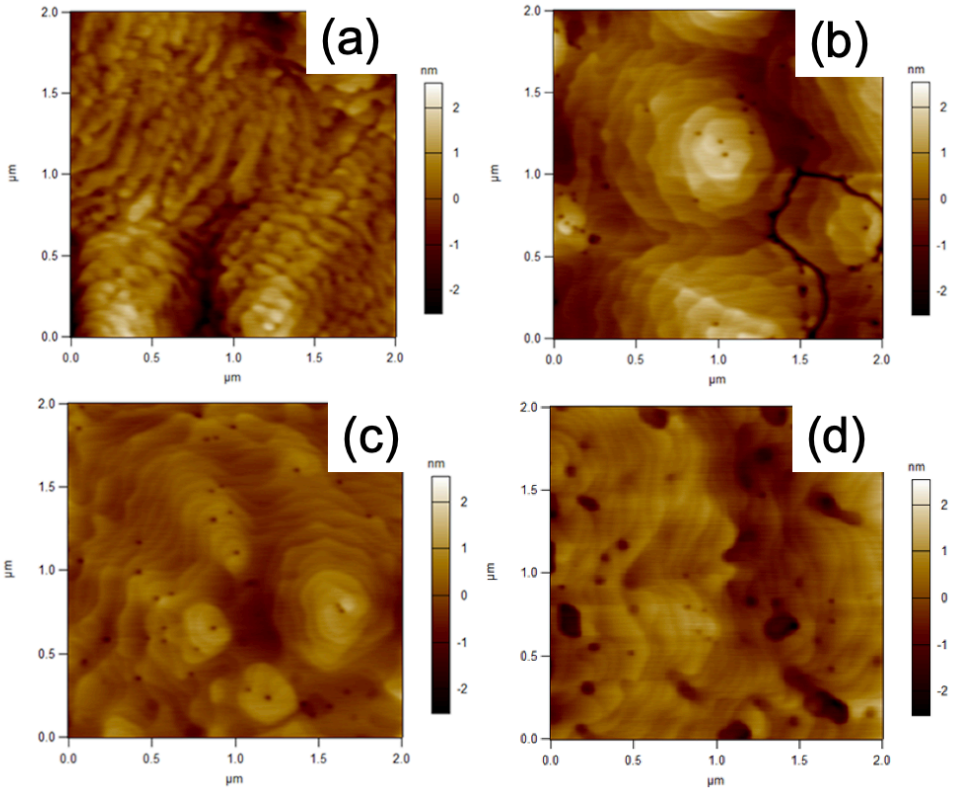

Figure 4-6: AFM scans for (a) IC1 grown at 540 ℃, (b) IC2 grown at 550 ℃, (c) IC3 grown at 560 ℃, (d) IC4 grown at 570 ℃. RMS values for samples IC1-4 were 0.6 nm, 0.7 nm, 0.58 nm and 0.57 nm respectively.

Fig. 4-7 below shows a plot of In-composition as a function of growth temperature for the IC series along with other growths done under slightly different active N-fluxes taken across a year and a half time span. Over time and under extended use, the active N-flux from a plasma source will change. Since the growth rate of GaN grown under Ga-rich condition is determined by the active N-flux, growth rate calibrations need to be carried out

every few months to check for deviations in the growth rate. Since active N-flux impacts InGaN In-composition, InGaN calibrations must also be carried out before any InGaN growth campaign to check for drift in In-composition. The data points in Fig. 4-7 other than the IC series, come from temperature-series calibrations grown under different plasma conditions. Active N-flux equivalent growth rates determined from GaN growth rate calibrations are noted in the plot in Fig. 4-7. All past InGaN calibration samples were growth on planar MOCVD grown GaN-on-sapphire templates.

Although the growth conditions may be slightly different for the other growths in Fig. 4-7 there is an obvious decrease in In-composition with increasing substrate temperature. From Fig. 4-7 it is also obvious that higher active N-equivalent growth rates leads to higher In-composition further supporting equation 3.7. Thus, both temperature and active N-flux can be used to control In-composition.

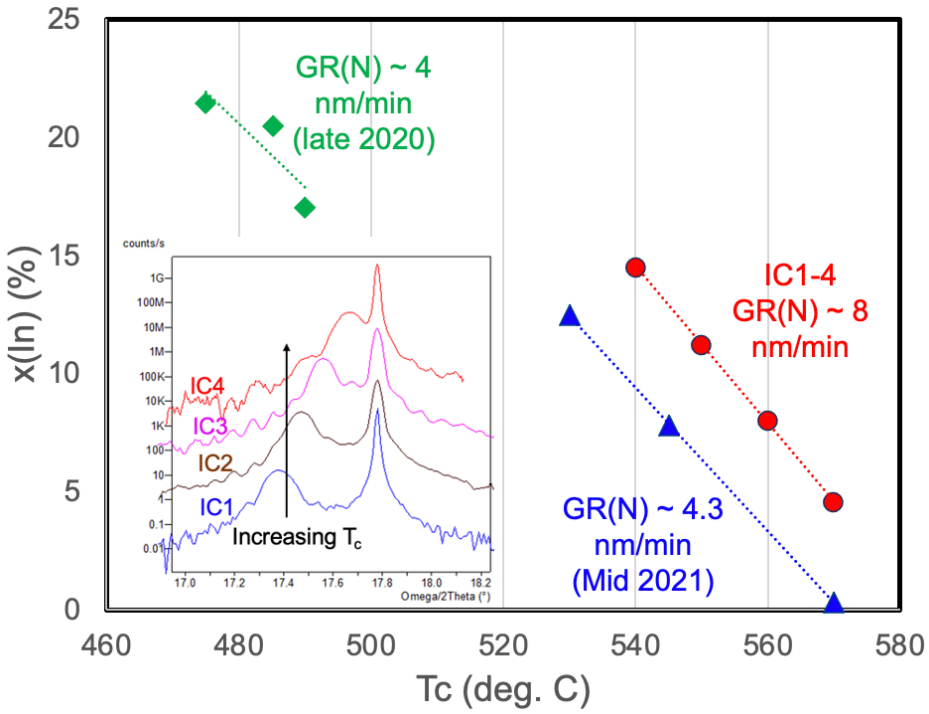

Figure 4-7: Plot of In-composition as a function of substrate temperature for the IC1-4 series along with other InGaN calibration growths done under different N-equivalent growth rates. The bottom left inset shows the (0002) $\boldsymbol{\omega - 2\theta}$ XRD scans for the IC growth series for which In-composition was extracted from.

It can be concluded from this study that growth temperature can be used as an effective means to control In-composition when growing InGaN within a composition range of 4.5% to 14.5% by tuning the substrate temperature from 540 °C up to 570 °C. Although temperature controlled In-composition has been well documented and widely used in MOCVD and MBE [127], this work demonstrates reproducibility by using the UCSB MBE system. Considering the degradation in surface morphology and film quality that accompanies low temperature growth this may not be the most ideal way to attain higher In-compositions. Ideally, to get the best quality InGaN, growth conditions should be adjusted such that the highest possible growth temperature can be used for a given In-composition. However, when growing multiple InGaN layers at different compositions it may be advantageous to only have to change one condition (i.e. temperature) when going

between layers rather than multiple conditions (i.e. temperature, cell-fluxes, plasma conditions ect..) which would require growth interrupts that may lead to an accumulation of impurities on the surface. This work will be helpful for future studies involving growth of multiple InGaN layers of different In-compositions for structures such as composition grades.

4.6 Film quality and Relaxation (ID/IE)

The experimental data presented in this chapter up until now consists only of thin InGaN layers grown coherently strained to planar GaN. Since the following chapters will focus a great deal on differentiating elastically relaxed InGaN layers with those which are plastically relaxed (i.e. through formation of defects) it is necessary to consider what happens to a pseudomorphic InGaN layer as it approached the critical thickness (h_c) for which plastic relaxation occurs. Higher In-composition InGaN will have a higher in-plane lattice mismatch to GaN and thus a smaller h_c. Furthermore, as mentioned in chapter 3, h_c is known to be highly dependent on growth conditions. By analyzing film quality, relaxation, and surface morphology for films grown at different thicknesses and In-compositions (controlled by temperature) we can see how the films start to behave as they approach or surpass h_c.

In the following study, two sets of three InGaN growths each, of varying thickness are carried out at different In-compositions. The N-flux equivalent growth rate, extracted from GaN growth rate calibrations, was approximately 5 nm/min for this series. The first series in this study, labeled as ID1-3 was grown at a 550 ℃ which resulted in an average In-

composition of approximately 9% when grown coherently strained to GaN (see appendix A.1). The second series, labeled as IE1-3 was grown at 530 ℃ which gave an approximate In-composition of 16% (see appendix A.1) when grown coherently strained to GaN. For both ID1, ID2 and ID3, the InGaN thicknesses were 45 nm, 180 nm and 225 nm respectively. The same thicknesses for IE1-3 were also used (45 nm, 180 nm and 225 nm for IE1, IE2 and IE3 respectively). For all six samples AFM, $\{\bar{1}\bar{1}24\}$ XRD RSM and (0002) XRD $\omega - scans$ of the InGaN peaks were performed. Fig. 4-8 shows the XRD RSM scans for ID1-3 and IE1-3. In-composition, extracted from $\{\bar{1}\bar{1}24\}$ XRD RSMs, were found to be 16%, 17% and 15% for samples ID1, ID2 and ID3 respectively and 11%, 10% and 8% for IE1, IE2 and IE3 respectively. Relaxation values, also extracted from RSMs, were found to be 0%, 9.1% and 12.3% for samples ID1, ID2 and ID3 respectively and 0%, 4.9% and 8% for IE1, IE2 and IE3 respectively. The (0002) InGaN $\omega - scan$ FWHM ($FWHM_{(0002),InGaN}$) values for ID1, ID2 and ID3 were found to be 264 arcseconds, 559 arcseconds and 579 arcseconds respectively. $FWHM_{(0002),InGaN}$ values for IE1, IE2 and IE3 were found to be 254 arcseconds, 333 arcseconds and 351 arcseconds respectively. To compare surface morphology of a strained layer with a partially relaxed layer, AFM scans were carried out on the thickest and thinnest samples from each respective growth temperature. Fig. 4-9 shows the 2x2 μm^2 AFM scans for ID1, ID3, IE1 and IE3. RMS values extracted from AFM scans for ID1, and ID3 were found to be 1.10 nm and 1.56 nm respectively. Surface RMS values extracted from AFM scans for IE1 and IE3 were found to be 1.13 nm and 2.03 nm respectively. Table 4-4 below gives the experimental data for this study. Fig. 4-10 gives a plot of $FWHM_{(002),InGaN}$ and relaxation as a function of thickness for the ID series and IE series.

Table 4-4: Experimental data for the ID and IE series. In-composition (x_{In}) and relaxation (R) were extracted from ($1\bar{1}24$) XRD RSM scans shown in Fig. 4-8.

Sample name	Growth temp (°C)	t_{InGaN} (nm)	x_{In} (%)	R (%)	$FWHM_{(002),InGaN}$ (arcsec.)	RMS (nm)
ID1	530	45	16	0	264	1.10
ID2	530	180	17	9.1	559	-
ID3	530	225	15	12.3	579	1.56
IE1	550	45	11	0	254	1.13
IE2	550	180	10	4.9	333	-
IE3	550	225	8	8	351	2.03

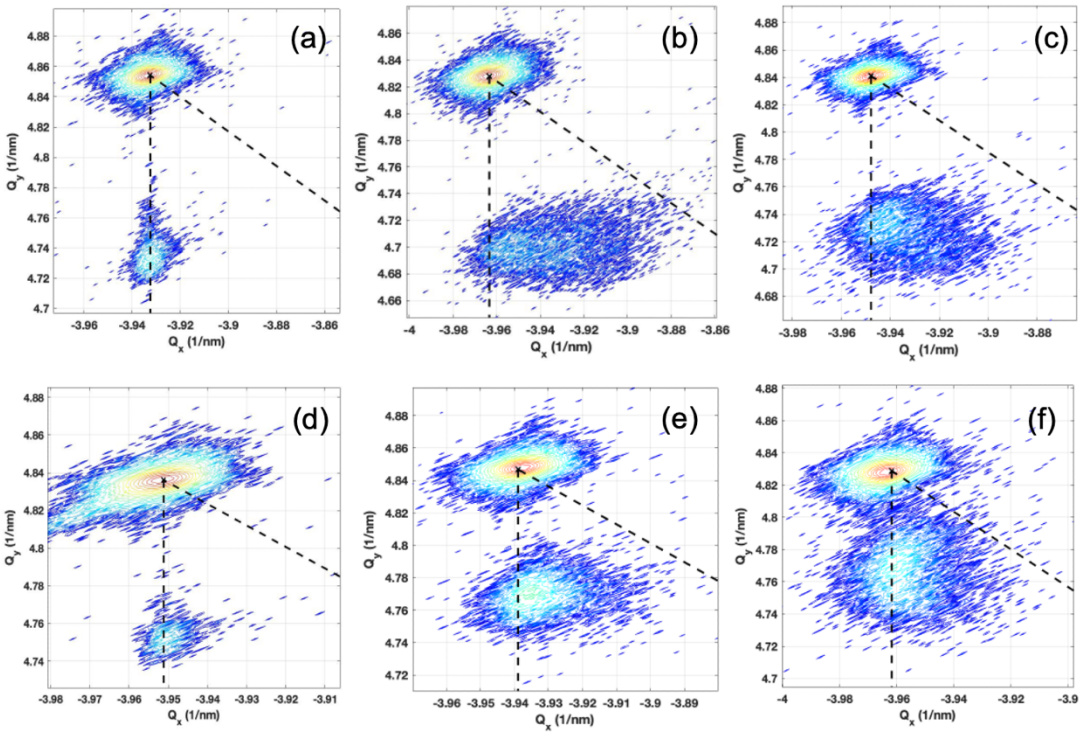

Figure 4-8: ($1\bar{1}24$) XRD RSM scans for (a) ID1, 45 nm InGaN grown at 530 °C, (b) ID2, 180 nm InGaN grown at 530 °C, (c) ID3, 225 nm InGaN grown at 530 °C, (d) IE1, 45 nm InGaN grown at 550 °C, (e) IE2, 180 nm InGaN grown at 550 °C and (f) IE3, 225 nm InGaN grown at 550 °C. The vertical dotted line segment running from the center of the GaN peak (top peak) down, is the fully strained line. The angled dotted line segment running from the GaN peak is the fully relaxed line.

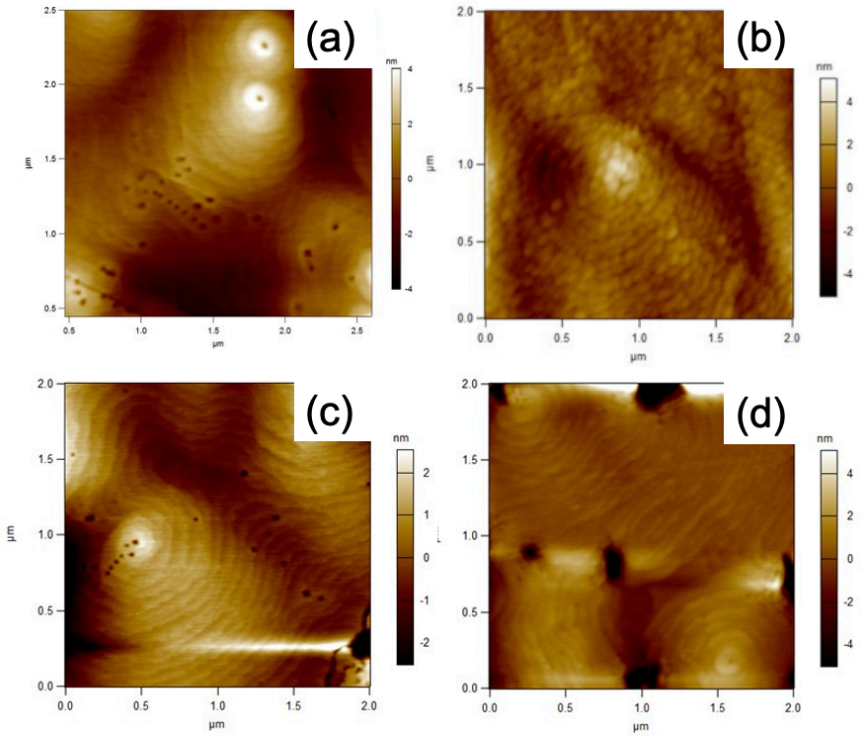

Figure 4-9: AFM micrographs for (a) ID1, 45 nm InGaN grown at 530 ℃, (b) ID3, 225 nm InGaN grown at 530 ℃, (c) IE1, 45 nm InGaN grown at 550 ℃, (d) IE3, 225 nm InGaN grown at 550 ℃. RMS values extracted from AFMs were found to be 1.1 nm, 1.56 nm, 1.13 nm, and 2.03 nm for ID1, ID3, IE1, and IE3 respectively.

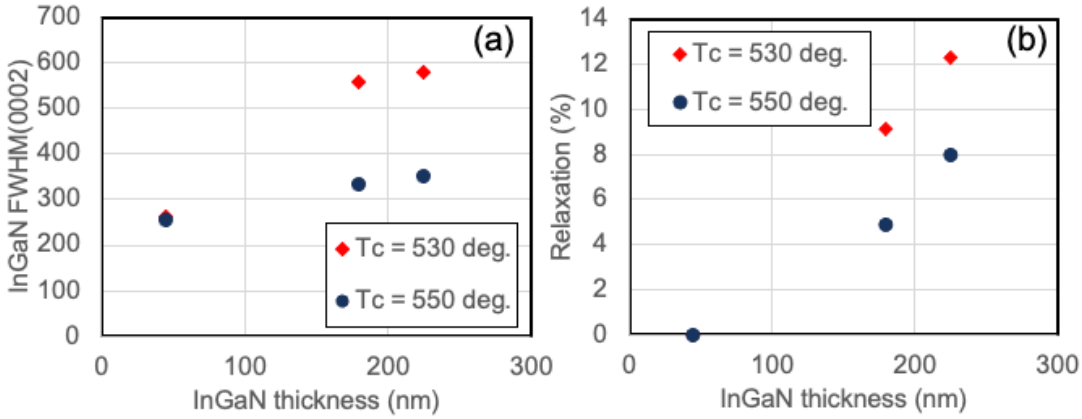

Figure 4-10: Plot of (a) (0002) $\boldsymbol{\omega - scan}$ FWHM of the InGaN (in arcseconds) as a function of film thickness for the ID series (growth at 530 ℃) and IE series (growth at 550 ℃) and (b) relaxation as a function of film thickness extracted from RSMs in Fig. 4-8. For both plots red diamond data points represent ID series (growth at 530 ℃) and the dark blue circle data points represent the IE series (growth at 550 ℃).

Considering relaxation, In-composition, and thickness: an obvious increase in relaxation as a function of thickness in Fig. 4-10 is observed, furthermore, the data in table 4-4 also shows that In-composition fluctuates and even decreases for the thickest layers.

This is particularly true for the InGaN grown at 550 ℃ where In-composition goes from 11% to 8% when the thickness is increased from 45 nm to 225 nm. From the RSMs in Fig. 4-8.d-e (growth at 550 ℃) the InGaN peaks appear to move along the vertical dotted line segment closer to the GaN peak as the layers get thicker. As mentioned earlier, from composition pulling, as InGaN relaxes there should be a corresponding increase in In-uptake. However, this is only true for significant values of relaxation, whereas the 225 nm InGaN layer grown at 550 ℃ is only 8%. The fact that there is slight relaxation in ID2 and IE2 (180 nm InGaN grown at 530 ℃ and 550 ℃ respectively) with a corresponding increase in the (0002) FWHM (see Fig. 4-10.a) suggests the critical thickness is less than 180 nm for these two In-compositions and therefor some form of plastic relaxation is occurring.

The change is surface morphology of these films as they surpass h_c is of particular importance. As can be seen in Fig. 4-9.a and Fig. 4-9.c., the surface morphology of the 45 nm InGaN grown at 530 ℃ and 550 ℃ have nearly identical spiral step-flow morphology. From Fig. 4-9.b and 4-9.d, it can be observed that when the thickness is increased to 225 nm the surface morphology of the two films grown at different temperatures diverges. For the 225 nm InGaN grown at 530 ℃, the surface still possesses spiral surface features, however the spirals become grainier with less defined terraces. For the 225 nm InGaN grown at 550 ℃ the spiral step-flow morphology with well-defined step terraces is still present, however several V-defects are observed on the surface which contributes to the large RMS value of 2.03 nm. The origin of these V-defects may be traced to the growth temperature. Increasing the growth temperature can lead to a decrease in supersaturation and thus a reduction in the lateral growth rate. Mentioned in chapter 1, the nature of V-

defect growth heavily relies upon the slower growth rate of the 6 equivalent $\{10\bar{1}1\}$ facets compared growth on the $\{0001\}$ plane. This leads to an increase in the crater size as a function of growth time. Therefore, It can be speculated that as the InGaN thickness surpasses h_c for the higher temperature growth, V-defects form from pre-existing dislocations to alleviate strain near the surface, which, due to the higher growth temperature and thus lower supersaturation, grow in diameter over time. This trend in growth temperature and V-defect formation was also observed by C. Bazioti et al., where higher temperature growth of InGaN on GaN by PAMBE led to strain relaxation via V-pit formation [120]. Appendix A.2 demonstrates how ultra-low temperature InGaN growth on tiles leads to an increase in lateral growth rate on the tile sidewalls. It should be emphasized the surface pit density is consistent with the TDD of the MOCVD grown GaN template (mid 10^8 cm^{-2} range) and therefore it can be assumed that the V-defects are from pre-existing dislocations in the substrate. In the case of the InGaN layer grown at 530 °C, the grainy and tall spiral growth for the 225 nm thick layer suggests the degradation in step-flow growth may be related to relaxation via roughening such as what has been observed by Snyder et al., [132] and Gao et al., [133], however this is subject to further study.

4.7 Cross Hatching

Some past InGaN growths done on planar GaN revealed cross-hatched surface features. Fig. 4-11 below shows the AFM (Fig. 4-11.a) and XRD RSM scan (Fig. 4-11.b) for sample IF1, 100 nm of $In_{0.12}Ga_{0.88}N$ grown on planar GaN which exhibited cross-hatching on the surface similar to what had been observed by Q. T. Li et al., for 50 nm of $In_{0.18}Ga_{0.82}N$

[125]. This growth was carried out at 530 ℃ with growth conditions identical to sample ID1. The surface RMS value extracted from the AFM in Fig. 4-11.a was found to be approximately 1 nm. The RSM in Fig. 4-11.b showed approximately 6% relaxation. Small pits are also visible on the surface of IF1; some of which run along the cross-hatching lines. These small pits are also indicative of dislocation networks.

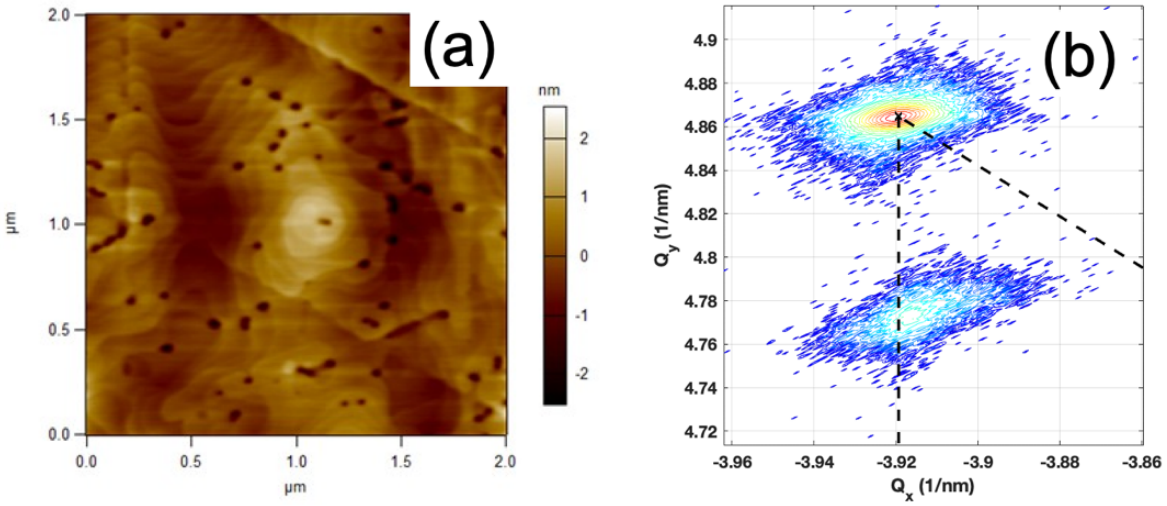

Figure 4-11: (a) AFM image of IF1 which had an RMS value of approximately 1 nm. (b) $(\bar{1}\bar{1}24)$ XRD RSM scan for IF1 which showed approximately 6% relaxation.

Mentioned in chapter 3 (see Fig. 3-3), the observed cross-hatching observed in Fig. 4-11 suggests that beyond the critical thickness of $In_{0.12}Ga_{0.88}N$ grown at these growth conditions, the $\{11\bar{2}2\}\langle 11\bar{2}3\rangle$ secondary slip system gets activated via the formation of misfit dislocations. This effect was not observed in AFMs for ID3 or IE3 which were well beyond the critical thickness for their respective In-compositions. It could be speculated that the punch-out effect (see Fig. 3-3, chapter 3) due to dislocation glide along the $\{11\bar{2}2\}\langle 11\bar{2}3\rangle$ slip-system only occurs during cool down after growth when the thickness is slightly above h_c. For the thicker films such as ID3 and IE3 it can be said that relaxation occurs during the growth by some other mechanism (i.e. formation of new TDs, or

roughening or V-pits). The small pits on the sample surface which do not sit on top of a spiral are known to be from pure-edge dislocations or dislocation networks [49]. It is not the purpose of this experimental study to understand the nature of how and why this type of surface morphology occurs as this is outside the scope of this work.

4.8 Conclusion

To summarize the results from the InGaN growth campaign given in this chapter: In the IA-series, an In-flux was established for growth at 550 ℃ with an active N-flux equal to approximately 4 nm/min. More importantly, this study demonstrated how In-flux effects surface morphology and In-composition when growing below In-rich conditions when equation 3.7 is not satisfied. The IB-study demonstrated how Ga-flux can effectively control growth rate and is less effective in controlling In-composition provided equation 3.7 is satisfied. The IC-study demonstrated how growth temperature can be used to accurately control In-composition. Furthermore, this study showed how active N-flux also impacts In-composition. The ID-study and IE-study shows how surface morphology behavior diverges for growth at different growth temperatures when exceeding the h_c. Higher temperature growth results in V-pits on the surface when the film relaxes which may be attributed to the suppressed lateral growth rate. As shown in the IF-study, some samples which show cross-hatching on the surface when growing slightly past h_c, due to misfit dislocations gliding along secondary slip systems. It was speculated that this 'punch-out' effect occurs during the sample cool down. This work will serve as a baseline for chapter 6 when InGaN

growth by PAMBE is explored on substrates which promote relaxation via a porous compliant underlayer.

5 Relaxed InGaN Substrates for Longer Wavelength micro-LEDs

5.1 Introduction

Micro-LED displays, augmented reality (AR) and virtual reality (VR) are among the most profound emerging technologies of this decade. These technologies require ultra-small (<10 μm) LEDs of all three primary colors (red, green and blue) with ultra-high efficiencies. Large area AlInGaP-based LEDs are commercially available however they suffer from poor efficiency when scaled to the micron-size. Having micro-LEDs of all three primary colors from a single material system would be advantageous in terms of cost. Although the nitride system covers a bandgap stretching from the UV to the deep infrared (IR) regime, achieving emission wavelengths beyond green has been a challenge. While commercial grade blue and green nitride-based LEDs have already been in production for some time, nitride-based red LEDs are still inferior in terms of efficiency for commercial applications.

This is due to the lattice mismatch between GaN and InN which creates significant strain when growing high In-composition InGaN – something which is required for longer wavelengths such as amber and red. In this chapter past results of nitride-based red LEDs will be discussed followed by the two main challenges associated with improving the efficiency of red nitride-based LEDs. The motive for relaxed InGaN substrates and how they have been achieved through different means will be discussed following a more detailed discussion on the technique of using nanoporous GaN tiles for achieving device-quality relaxed InGaN.

5.2 Red LED Literature Survey

Aluminum gallium indium phosphide (AlInGaP) is currently the industry standard material for red LEDs. Although large AlInGaP LEDs have efficiencies above 50%, when shrunk down to the micron-scale the efficiency drops significantly. This is due to the high surface recombination rate inherent in AlInGaP [33], [134]–[136]. Furthermore, AlInGaP suffers from low thermal stability [33], [137] which impedes performance at higher temperatures. Despite the issues associated with red nitride-based LEDs there has been progress in the last 15 years in making red nitride-based optoelectronics. In 2006 M. Funato et al., demonstrated a 320x320 μm^2 amber LED with a peak EQE of 1.6% on semi-polar $\{11\bar{2}2\}$ bulk GaN [138]. In 2014 Hwang et al., of Toshiba Corp. published its demonstration of a 460x460 μm^2 LED with a peak EQE of 1.6% at a wavelength of 629 nm [139]. Two years later, Iida et al., published its work on a 370x370 μm^2 620 nm LED with a peak EQE of 0.6% [140]. Utilizing the V-defects which occur when growing thick InGaN on GaN by MOCVD,

Zhang et al., demonstrated a 621 nm wavelength, 1x1 mm^2 LED on Si(111). Although peak EQE was not reported in this work, Zhang et al., did report a wall-plug efficiency (WPE) of 16.8% [33]. Although these red nitride-based LEDs show promise, they are far too large and possess still too low efficiency to be considered for self-emissive display technology. Most recently, however, P. Li et al., demonstrated a 5x5 μm^2 red LED with emission at 607 nm and a peak EQE greater than 2% by growing on a patterned sapphire substrate (PSS) [141].

5.3 Composition Pulling Effect

The lattice mismatch between GaN and InN is approximately 11%. This is significant considering the lattice mismatch between AlN and GaN is approximately 2.4%. The large in-plane lattice constant of InN is due to the size of the In atom which has an atomic number of 49 compared to Ga which has an atomic number of only 31. This leads to complications when trying to grow high composition InGaN on relaxed GaN substrates. For pseudomorphically strained InGaN grown on GaN, In-composition is limited due to high compressive strain. This rejection of In due to the high biaxial compressive strain is known as the composition pulling effect (CPE) [142]–[144] which significantly limits growth of high In-composition InGaN on GaN.

5.4 Quantum Confined Stark Effect

Previously discussed in chapter 1, the piezoelectric charge from strain at the interfaces in an LED quantum well (QW) creates additional band bending in the LED QW which pushes the electron and hole wavefunctions further away from one another thereby

reducing radiative recombination. This effect, known as the quantum confined stark effect (QCSE) [145] is illustrated in Fig. 5-1.

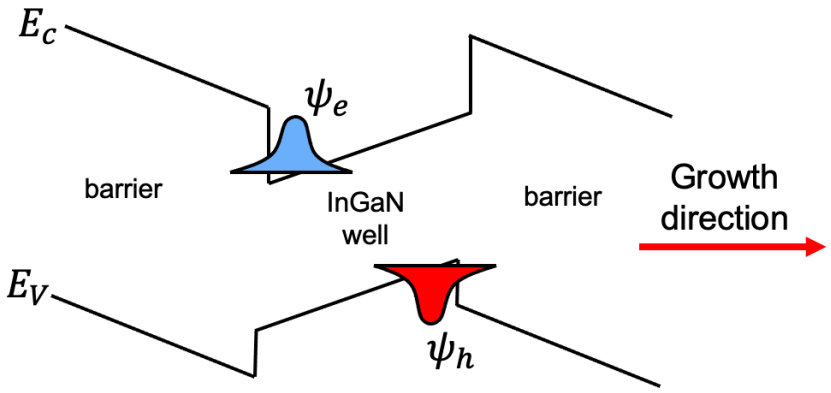

Figure 5-1: Illustration of the quantum confined stark effect (QCSE). Band bending in the InGaN quantum well due to the large strain-induced piezoelectric charge at the two heterointerfaces leads to separation of the electron-hole wave function which reduces radiative recombination.

There is a significant amount of literature related to QCSE in nitride optoelectronics. Using a drift-diffusion model, Park et al. demonstrated, theoretically, that strain compensated InGaN QW structures would yield enhanced internal quantum efficiency (IQE) and improved efficiency droop over conventional strained InGaN structures grown on planar GaN [146]. Matthias Auf der Maur et al., demonstrated the magnitude QCSE has on IQE as a function of emission wavelength using simulation which is shown in the Fig. 5-2 plot below [147]. Fig. 5-2 shows how QCSE is the dominating issue at higher wavelengths severely limiting maximum IQE.

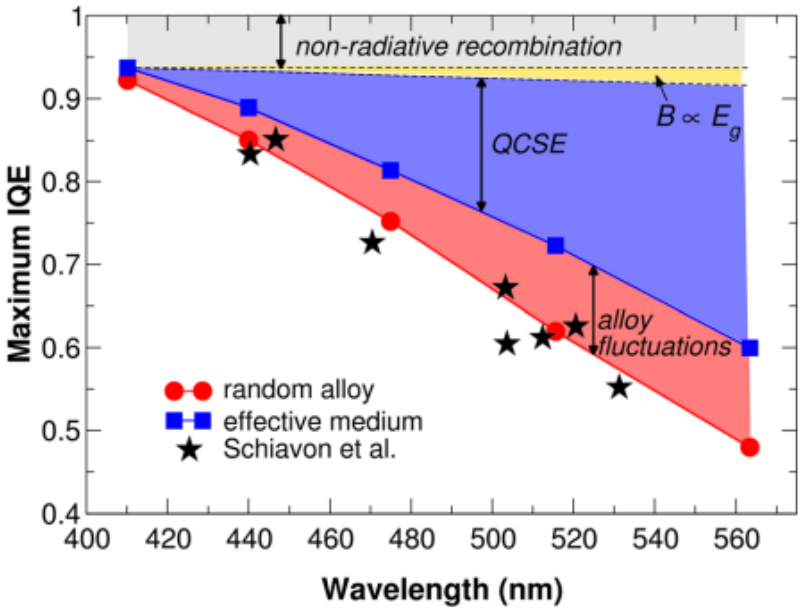

Figure 5-2: Maximum IQE as a function of emission wavelength showing the effects of alloy fluctuations and QCSE. Reprinted with permission from [147] with data also taken from Schiavon et al., [148]. Copyright American Physical Society.

5.5 Relaxed InGaN Literature Survey

Relaxed InGaN substrates, would enable the growth of thicker and higher In-composition InGaN layers while simultaneously reducing the piezoelectric charge at $In_xGa_{1-x}N/In_yGa_{1-y}N$ multi-quantum well (MQW) heterointerfaces thereby reducing efficiency droop. This provokes an interest in the development of high-quality elastically relaxed InGaN substrates. Valdueza et al. demonstrated relaxed $In_{0.2}Ga_{0.8}N$ layers, up to 500 nm thick, grown by plasma-assisted molecular beam epitaxy (PAMBE) which exhibited enhanced In-incorporation, however, a large density of threading dislocations (TDs) and stacking faults were observed in these relaxed films [82]. Islam et al. demonstrated a reduction in edge-type dislocations by employing step-graded interlayers to achieve relaxed InGaN templates [149]. This was demonstrated by, Däubler et al. who, using a linear composition grade, demonstrated relaxed InGaN substrates grown by MBE. These relaxed

InGaN substrates were subsequently used for MOCVD growth of InGaN MQWs which exhibited significantly higher IQE for green light compared to structures grown on planar GaN [150]. Hestroffer et al., also developed compositionally graded relaxed InGaN layers by PAMBE on vicinal N-polar GaN templates grown by MOCVD [123], [151]. These graded InGaN buffers exhibited a higher PL intensity and a red-shift compared to planar GaN substrates [151]. It was shown that although compositionally grading InGaN grown on GaN helped to reduce edge-type dislocation densities, it did not reduce screw-component dislocation densities [149]. To reduce dislocations at the GaN/InGaN interface, Liu et al. employed a glancing angle ion flux treatment prior to InGaN growth on GaN, resulting in the presence of nanoscale surface corrugations. By rotating the sample for continued InGaN growth, these surface corrugations smoothened yielding fully relaxed InGaN with extremely low dislocation density. Unfortunately, when growing MQW layers on these structures the top p-InGaN layer exhibited poor crystal quality due to defects associated with relaxation of the top p-InGaN layer [152]. MOCVD-grown InGaN MQW nanostripe arrays showed uniaxial elastic relaxation perpendicular to the stripe direction [153], [154]. Relaxed $In_{0.17}Ga_{0.83}N$ grown on $ScAlMgO_4$ (SCAM) has also been demonstrated with a 502 nm PL peak, unfortunately the residual oxygen impurity incorporation in these InGaN films was high [155]. InGaN grown on ZnO has also been demonstrated with some success by both MOCVD [156] [157] and pulsed laser deposition [158]. More recently, Bi et al. demonstrated ~1 μm wide platelets of relaxed $In_{0.18}Ga_{0.82}N$ grown by MOCVD which show promise [159]. Soitec has developed relaxed InGaN pseudo-substrates using their Smart Cut™ technology [160] to fabricate blue LEDs with increased In-content and reduced

efficiency droop. For these LEDs, enhanced In-incorporation was observed through a red-shift in the PL spectra with IQE values of 31% and 10% at a wavelength of 536 nm and 566 nm respectively [146]. Later, using this same technology, Dussaigne et al. demonstrated 10 μm diameter circular red micro-LEDs with a peak wavelength of 625 nm and an external quantum efficiency (EQE) of 0.14% [161]. More recently, relaxed $In_{0.04}Ga_{0.96}N$ films were demonstrated using a very thin compliant layer formed via thermal decomposition of an InGaN quantum well [162]. Reducing surface roughness and scalability of these relaxed films with higher In compositions, remains a work in progress [162].

5.6 Porous GaN Tiles

The work in this thesis focuses on utilizing porous GaN substrates to achieve high-quality relaxed InGaN suitable for optoelectronic device fabrication. For simplicity, porous GaN tiled pseudo-substrates will be referred to as 'PS' for the remainder of this thesis. Relaxed metal-polar InGaN tiles on porous GaN are achieved by patterning and reactive ion etching (RIE) of square tiles through a thin unintentionally doped (UID) GaN layer followed by a partial etch through a thick GaN:Si layer. Following a well-calibrated electro-chemical (EC) etch, the mechanical stiffness (elastic modulus) of the GaN:Si underlayer is reduced via porosification enabling the compliant behavior of the tile [163]. The reduced mechanical stiffness of the porous underlayer has been previously reported in porous Si [164]. Subsequent growth of InGaN on these porous GaN tiles results in an elastically relaxed layer of InGaN. Fig. 5-3 offers a high-level overview of this process.

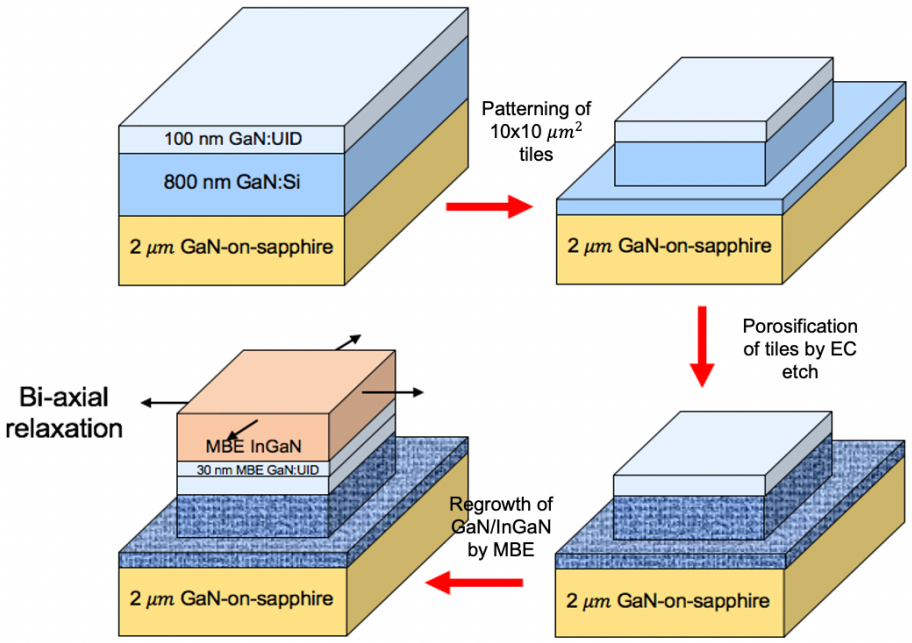

Figure 5-3: Process flow for obtaining high-quality relaxed InGaN on PS. Starting from top left, MOCVD growth of 800 nm GaN:Si/100 nm GaN:UID on GaN-on-sapphire templates; top right, patterning and etching of 10x10 $\boldsymbol{\mu m^2}$ tiles; bottom right, porosification of tiles by electro-chemical (EC) etch; and bottom left, MBE regrowth of UID GaN and InGaN resulting in bi-axial relaxation. Reprinted with permission from [165]. Copyright AIP Publishing.

Porosification of GaN, achieved by the EC etching of GaN:Si [166], has already been employed in a variety of applications, particularly for DBR lasers[167]–[171] and film delamination [172].

Porosification:

Before going into detail on the mechanisms behind elastic relaxation of InGaN on porous tiles it is necessary to understand the mechanisms behind porosification. The EC etching of conducting GaN occurs when the GaN substrate is submerged in an electrolytic solution. Metal deposited on the GaN substrate contacted to the conducting GaN layer acts as the anode while a Pt wire submerged in the solution acts as the cathode (see Fig. 5-4.a below). A bias is applied to the contacts using a voltage controlled current source such as

a power supply. The conductive GaN (usually Si-doped GaN) electrolyte interface acts as a reverse bias Schottky contact pulling the fermi-level below the valence band creating a large concentration of holes near the surface. Hole-assisted oxidation occurs on the surface which is subsequently etched by the electrolyte and transported away from the interface [173]. This is illustrated in the band diagram shown in Fig. 5-4.b.

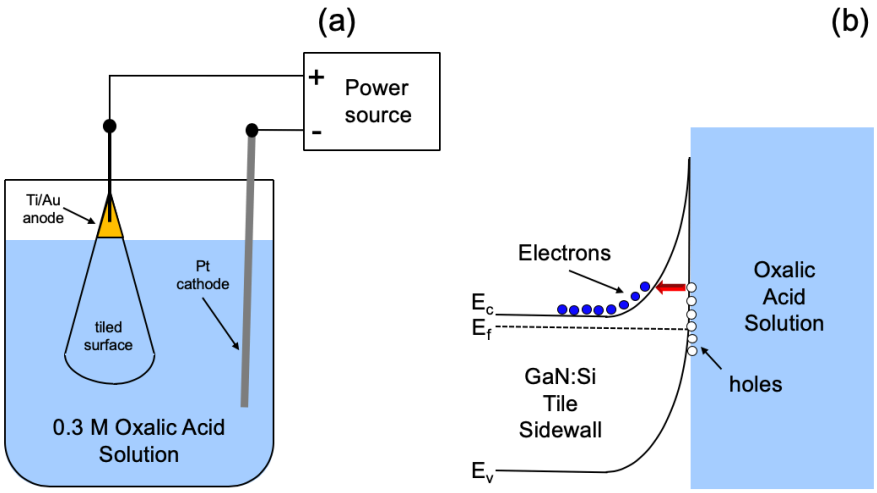

Figure 5-4: Diagram illustrating the EC etch setup used for Porosification. (b) band diagram showing the generation of holes at the GaN:Si/electrolyte interface which leads to oxidation at the surface and subsequent etching of the oxide by the electrolyte.

The reaction that takes place during this process can be broken down as such [174]:

$$\boldsymbol{2GaN + 6h^{+} \rightarrow 2Ga^{3+} + N_2} \quad 5.1$$

$$\boldsymbol{H_2O + 2h^{+} \rightarrow 2H^{+} + O_2} \quad 5.2$$

$$\boldsymbol{2H^{+} + 2e^{-} \rightarrow H_2} \quad 5.3$$

Where the products (right hand side of equations 5.1-3) of these reactions are all transported away from the interface. Near the Pt cathode H_2 also forms via a hydrogen ion reduction reaction [173]. This EC etching of GaN has been demonstrated using a variety of solutions including KOH [174], HBr + Na_2SO_4 (Sigma-Aldrich) [175], HF [176], and oxalic acid [166], [167], [169]. With the exception of oxalic acid, nearly all of the other EC etch

solutions mentioned required illumination to assist in hole generation. Etching tiles with a non-conductive thin UID GaN layer above the GaN:Si layer (illustrated in Fig. 5-3) involved using oxalic acid without any illumination. In the case of the tiles shown in Fig. 5-3, porosification took place laterally through the non-polar tile sidewalls. Nanopores form when the EC etch begins resulting in a concentrated electric field due to the low radius of curvature in the pore. The high electric field in the region of the pore which has the lowest radius of curvature (i.e. the tip) generates a high density of free holes leading to further oxidation of the tip resulting in deeper etching into the nanopore. This results in finger-like pores which propagate laterally through the tile [173], [175]. This is illustrated in the tile cross-section FIB-SEM taken from a sample after Porosification shown in Fig. 5-5.a-b with a corresponding diagram illustrating how the fingerlike pore morphology occurs (Fig. 5-5.c).

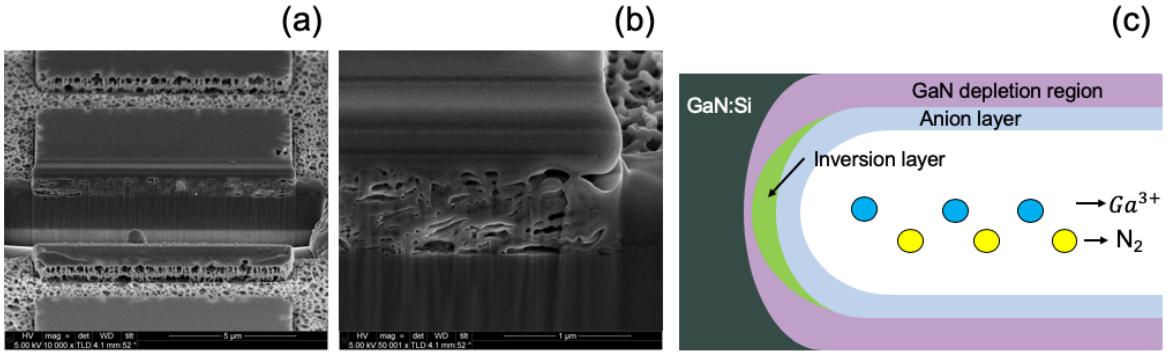

Figure 5-5: (a) FIB SEM cross-section showing the tile after Porosification, (b) close up of tile edge showing fingerlike pores and (c) a schematic showing the proposed EC etching of a nanopore which results in the observed finger-like pore, also described in reference [173].

5.7 Relaxation on Porous GaN tiles

From equation 3.1 in chapter 3, strained InGaN grown on GaN results in a compressively strained pseudomorphic layer with a corresponding strain energy 'E_h' that increases linearly as a function of InGaN thickness 'h'. Increasing the InGaN thickness on

planar GaN increases the strain field until, at some critical thickness, relaxation of misfit strain via plastic flow occurs [114]. However, when a strained film is grown on PS the compliant nature of the porous underlayer leads to elastic relaxation of the InGaN film at thicknesses lower than what is expected for plastic relaxation. Increasing the surface-to-volume ratio of porous GaN has been shown experimentally to reduce the mechanical stiffness and the elastic modulus [163] (or Young's Modulus) [177] thereby increasing compliance. The thin UID GaN layer on top of the porous layer seen in Fig. 5-3 becomes a 'compliant layer' stretching to confirm with the film above it. The increase in relaxation and decrease in lattice mismatch leads to a corresponding increase in In-composition via CPE. These high quality elastically relaxed films are an attractive technology in strain engineering [165].

The compliant nature of 10×10 μm^2 porous tiles was first demonstrated by Pasayat et al. [31] and have already been used as a substrate for red, green and yellow LEDs [178], [179]. Using MOCVD grown InGaN on porous GaN tiles, Pasayat et al., achieved a new in-plane lattice constant of 3.216 Å [180] corresponding fully relaxed $In_{0.076}Ga_{0.924}N$ [181, p.]. 6 μm x 6 μm micro-LEDs were fabricated on PS which had an on-wafer EQE of 0.2% for a wavelength of 632 nm at 10 A cm^{-2}. At the time this was the highest reported EQE for a red micro-LED [179].

5.8 Conclusion

This chapter was meant to give a high-level understanding of porosification and how it can be used to make compliant substrates. Porosification of tiles is carried out via a well-

controlled EC-etch of a GaN:Si underlayer which enables the compliance of the top UID GaN layer. Past work by MOCVD grown InGaN on PS has demonstrated that this technology has the potential to disrupt current display technology by making nitride-based red micro-LEDs available. Because of this, RGB monolithic integration may be possible which will severely disrupt the growing micro-LED mass-transfer startup community. Before this can take place, however, drastic improvements need to be made to increase the efficiency of the current proof-of-concept devices that have been demonstrated using PS. For this to happen films with higher in-plane lattice constants and smooth surface morphology must be achieved.

6 PAMBE InGaN Growth on Porous GaN Tiles (PS)

Mentioned previously, a major advantage MBE has over MOCVD is its ability to grow thicker and higher In-composition InGaN layers without generating V-defects on the surface. Although optoelectronic devices with MBE-grown active regions have been demonstrated with some success [84], [182], producing films with superior optical and electrical properties by MBE is not the focus of this study. Instead, this work will present a joint effort by both MOCVD and MBE to create relaxed InGaN pseudo-substrates on which highly efficient, longer-wavelength LED structures can be grown. MBE/MOCVD hybrid devices have already been both speculated [183] and demonstrated with success [184]. Furthermore, MOCVD regrowth on MBE-grown plastically-relaxed InGaN substrates has already been demonstrated [185].

This work focuses on higher In-containing PAMBE-grown elastically relaxed InGaN pseudo-substrates with improved surface morphology and structural film quality compared

to past work by MOCVD. Mentioned in the previous chapter, the highest reported equivalently relaxed In-composition ($x_{In,equiv.}$) achieved for InGaN grown on porous tiles by MOCVD was approximately 7.6% [181]. Considering the current limits possessed by MBE in terms of becoming a scalable growth technology, it is necessary to show a significant increase in the in-plane lattice constant to justify MBE as a method for making InGaN pseudo-substrates. This is especially true for consumer products such as micro-LEDS for display technology. This work demonstrates 125 nm of InGaN grown by PAMBE on PS with an in-plane lattice constant (a_{new}) of 3.231 Å which corresponds to an $x_{In,equiv.}$ equal to 12%. Using a temperature-controlled In-composition step-grade, higher values of $x_{In,equiv.}$ were achieved (up to 15.8%), however, it was found that dislocations had formed in these InGaN layers. When combining all of the data from this study, a saturation in $x_{In,equiv.}$ as a function of thickness was observed around 16%. Not only do these results exceed past work by MOCVD in terms of $x_{In,equiv.}$, these MBE-grown films exhibit surfaces free of V-defects making them attractive for red and amber micro-LEDs.

6.1 Experimental Details

Control samples in this study were all grown on MOCVD grown Ga-polar GaN-on-sapphire templates which will be referred to as 'planar GaN'. MBE growth of InGaN was conducted on both planar GaN, and on high fill factor GaN-on-porous-GaN tile arrays, using identical growth conditions. The process flow to obtain the final relaxed InGaN layers grown on PS (illustrated in Fig. 5-3) is laid out as such: MOCVD growth of GaN:UID/GaN:Si/GaN:UID stack (~2 μm/0.8 μm /0.1 μm respectively) on sapphire;

patterning of 10x10 μm^2 tiles; porosification of GaN:Si layer by EC etch; and PAMBE growth of GaN/InGaN. Si doping in the 0.8 μm porosified layer was ~5e18 cm^{-3}. 10×10 μm^2 tiles were defined by photolithography and RIE etching using a 100 watt BCl_3/Cl_2 etch chemistry; each tile was spaced 2 μm apart. The RIE etch defining the tiles went through the top 0.1 μm GaN:UID layer and approximately 0.45 μm into the GaN:Si layer. Porosification of the GaN:Si layers was done in a 0.3 M oxalic acid solution, where the GaN:Si layer acted as the anode and a Pt wire in the solution acted as the cathode. It is important to note that the top 100 nm UID GaN layers are not porosified as they are meant to provide a smooth surface for subsequent regrowth. Doping and electro-chemical etch conditions in this study were identical to past work from reference [180] which resulted in 50-60% porosification of the GaN:Si layer. Following porosification, the samples were subjected to a solvent clean and HF dip prior to PAMBE growth. All samples were outgassed at 400 °C for one hour in a high vacuum buffer chamber prior to being transferred into the main chamber for growth. Planar GaN control samples were either co-loaded with the PS samples, or grown in succession.

GaN and InGaN growth by PAMBE was carried out in a Varian Gen 2 system with conventional high-flux Ga and In effusion cells. The background pressure of the growth chamber was in the low 10^{-10} torr in the absence of cell-flux and N_2 gas. Active nitrogen was supplied by 1 sccm of 99.9995% pure N_2 via a VEECO Unibulb RF plasma source powered at 300 watts. Background pressure in the chamber during growth was approximately 1×10^{-5} torr. InGaN growths were carried out under In-rich conditions so to achieve the best possible film quality and surface morphology [35]. Like in the previous

study of InGaN growth on planar GaN, the growth temperature was recorded from a thermocouple mounted behind the substrate heater which is referred to as T_c. The growth surface was monitored in-situ by RHEED prior to, during and at the end of growth. To separate the InGaN from the regrowth interface all growths in this study were initiated with a thin layer of GaN grown at 720 °C under Ga-rich conditions**.** For the initial high-temperature GaN growth, a Ga-flux of approximately $1.7x10^{-6}$ torr was used. Prior to the start of growth, the samples were brought up to the GaN growth temperature and the surfaces were exposed to Ga-flux for 30 seconds and then thermally desorbed, as observed by RHEED intensity. For both planar and PS samples, the Ga desorption time was approximately 25 seconds indicating surface temperature between planar and PS samples were approximately the same. For growth on porous GaN tiles, approximately 30 nm of GaN was grown before lowering T_c for InGaN growth. Following InGaN growth, the sample was capped with a thin layer of GaN grown at the same temperature as the InGaN followed by thermal desorption of excess In. For thermal desorption of excess In, T_c was increased to 630 °C until a saturation in the RHEED intensity was observed indicating all of the In had desorbed.

The surface morphology of every sample was characterized post-growth by AFM using an Asylum MFP3D. Off-axis, $\{\bar{1}\bar{1}24\}$ reflection XRD $(\omega - 2\theta) - \omega$ RSM scans were carried out on every sample. Composition and relaxation were determined from the experimental XRD RSM data using X-Pert Epitaxy software. a_{new} was calculated from Vegard's law taken from reference [186]:

$$\boldsymbol{a_{new} = 3.1893\text{Å} \times \left\{1 - \left(x_{In} \times \frac{R}{100}\right)\right\} + 3.538\text{Å} \times x_{In} \times \frac{R}{100}} \quad 6.1$$

Where 3.1893 Å and 3.538 Å are the relaxed in-plane lattice constants for GaN and InN respectively. x_{In} and R refer to the In-composition and relaxation values extracted from the RSM scans respectively. In determining a_{new} from equation 1 using the R and x_{In} values extracted from XRD-RSM data, $x_{In,equiv}$ can be determined by setting R=100%, x_{In} = $x_{In,equiv.}$ in equation 6.1 and solving for $x_{In,equiv.}$.

Cross-sectional and planar specimen for scanning transmission electron microscopy (STEM) was carried out on some samples using an in-situ focused ion beam (FIB) lift-out method performed in a Thermo-Fisher Helios G4 Xe plasma FIB/SEM at the Michigan Center for Materials Characterization (MCMC) at University of Michigan by Dr. Kai Sun. A JEOl-JEM-3100R05 transmission electron microscope at MCMC equipped with double-aberration correctors was used for imaging the microstructures of the specimen. The microscope was operated at 300 keV in STEM mode with lens settings that define a probe smaller than 0.1 nm. High-angle annular dark-field (HAADF) imaging was performed together with bright-field (BF) imaging simultaneously.

RT PL was also carried out on certain samples to observe emission peaks coming from the InGaN layers so to determine if a red-shift had occurred as a result of growing on PS. The PL setup used in this study utilized a 325 nm laser in the UCSB Nanofab.

A summary of the experimental results from this study are shown in table 6-1 below.

6.2 InGaN Grown at T_c = 550 ℃ (PA)

The chapter 4 demonstrated that higher temperature growth of InGaN on planar GaN would result in the best possible film quality and surface morphology. It was also shown that growth temperature has a profound impact on In-composition and that higher temperature growth can lead to V-defect formation when the layer thickness surpasses h_c (see Fig. 4-9 from chapter 4). Previous work done by Pasayat et al., demonstarted a strong coorelation between relaxation and InGaN film thickness on PS without increasing In-composition in the gas phase by MOCVD [180]. In this section higher-temperature, lower In-composition InGaN growth on porous tiles was carried out in an attempt to achive maxium relaxation while maintaining the smoothest possible surface morphology and film quality.

For this section two growths were carried out on PS and two growths on planar GaN. For InGaN growth T_c was kept constant at 550 ℃. In and Ga flux was set to 6e-7 torr and 7e-8 torr respectively. Previous calibration runs (shown in appendix A.1) demonstrated that InGaN growth at this temperature, using these fluxes, results in an In-composition of approximatly 9% with a deviation of +/- 1.5 point-%. All samples were capped with approximately 1.5 nm of GaN at the end of growth. For the first two growths, labeled PA1 and PA1A, consisted of 80 nm of InGaN grown on PS and planar GaN respectively. PA2 consisted of 225 nm of InGaN grown on PS. This growth was not repeated on planar GaN as it was already done in a previous study (chapter 4 sample IE3). Therefore sample IE3 (225 nm InGaN on planar GaN) from chapter 4 was used to compare with PA2 (225 nm

InGaN on PS). $\{\bar{1}\bar{1}24\}$ XRD RSM scans are shown in Fig. 6-1 below. In-composition, extracted from the RSMs in Fig. 6-1 for PA1, PA1A, PA2 and IE3 were found to be 13.5%, 7.8%, 19.8% and 9.2% respectively. Relaxation for PA1A, PA1, IE3 and PA2 were found to be 7%, 36.4%, 8% and 80% respetively. Using equation 6.1, $x_{In,equiv.}$ was calculated from In-composition and relaxation to be 0.5%, 4.9%, 0.7% and 15.8% for PA1A, PA1, IE3 and PA2 respectively. Clearly, from these results shown in Fig. 6-1 and in table 6-1 the porous tiles significantly enhance relaxation and In-composition. This increase in In-uptake as a function of relaxation is due to composition pulling. Oddly, however, the InGaN peak for PA2 shown in Fig. 6-1.d appears far less defined compared to the other InGaN peaks in Fig. 6-1. The XRD $FWHM_{(0002),InGaN}$ values for PA1A (80 nm InGaN on planar), PA1 (80 nm InGaN on PS), IE3 (225 nm InGaN on planar) and PA2 (225 nm InGaN on PS) were 325 arcseconds, 480 arcseconds, 351 arcseconds and 602 arcseconds respectively. This clear increase in $FWHM_{(0002),InGaN}$ values for the InGaN on tiled samples suggests some *coorelation between relaxation and a degradation in film quality* due to plastic relaxation. Other factors may include lateral variations in In-composition or spiral height.

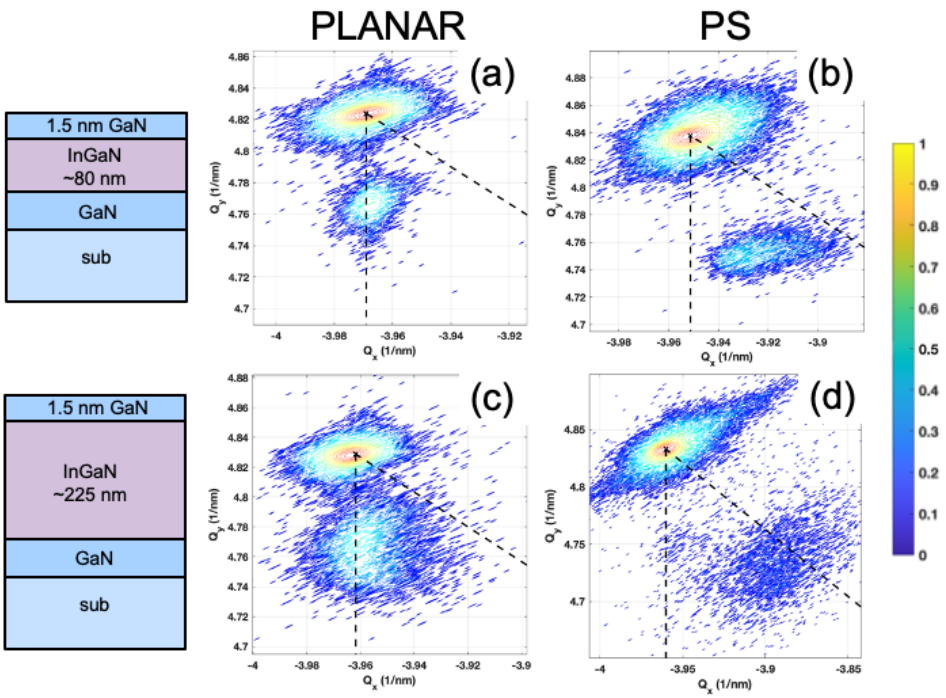

Figure 6-1: $\{\overline{1}\overline{1}24\}$ XRD RSM scans taken for InGaN growth at Tc = 550 ℃ for (a) PA1A (80 nm InGaN grown on planar GaN), (b) PA1 (80 nm InGaN on PS), (c) IE3 (225 nm InGaN on planar GaN) and (d) PA2 (225 nm InGaN on PS). Cooresponding sample structures are shown to the left of the RSMs and the substrate is indicated above the top two RSMs. Extracted In-compositions for PA1, PA1A, PA2 and IE3 were found to be 13.5%, 7.8%, 19.8% and 9.2% respectively. Extracted relaxation values for PA1A, PA1, IE3 and PA2 were found to be 7%, 36.4%, 8% and 80% respectively.

2x2 μm^2 AFMs from this study along with the AFM from IE3 are shown in Fig. 6-2. Surface RMS values for PA1A (80 nm InGaN on planar), PA1 (80 nm InGaN on PS), IE3 (225 nm InGaN on planar) and PA2 (225 nm InGaN on PS) were found to be 1.46, 1.05, 2.03 and 5 nm respectively. The AFM of sample PA1A (80 nm InGaN on planar GaN at T_c = 550 ℃) shows step-flow growth with some craters on the surface approximatly 225 nm in diamater. Just as in the case of IC4 in chpater 4, these craters are believed to come from In-droplets which formed on the surface. This effect has been observed before but it is not known as to why it happens in some cases and not in others. For PA1 (80 nm InGaN on PS at T_c = 550 ℃), the AFM in Fig. 6-2.b shows step-flow growth, however there are some mall pin-holes on the surface which may be associated with dislocation networks from the GaN-on-

sapphire substrate. As was discussed in chapters 1 and 4, the V-defects on the surface of IE3 (shown again in Fig. 4-9) likely generate to relieve strain, leading to the observed 8% relaxation, and are associated with the higher growth temperature. This effect is exacerbated in the case of PA2 (225 nm InGaN on PS at T_c = 550 ℃) which is an order of magnitude more relaxed than the planar sample IE3. PA2 appears to have larger V-defects which coalesce forming large trenches. It is likely that the poor InGaN peak observed in the RSM shown in Fig. 6-1 for PA2 is related to these surface features which may contribute to the high amount of relaxation. Past work by Pasayat et al., showed that the highest elastic relaxation achieved for InGaN grown on 10x10 μm^2 porous GaN tiles was only 65% with an In-composition of 11.76% for an InGaN thickness of 200 nm [180]. Knowing this, in conjunction with the surface morphology and poor InGaN peak seen in the RSM, it can be concluded that the 80% relaxation observed for PA2 is both plastic and elastic.

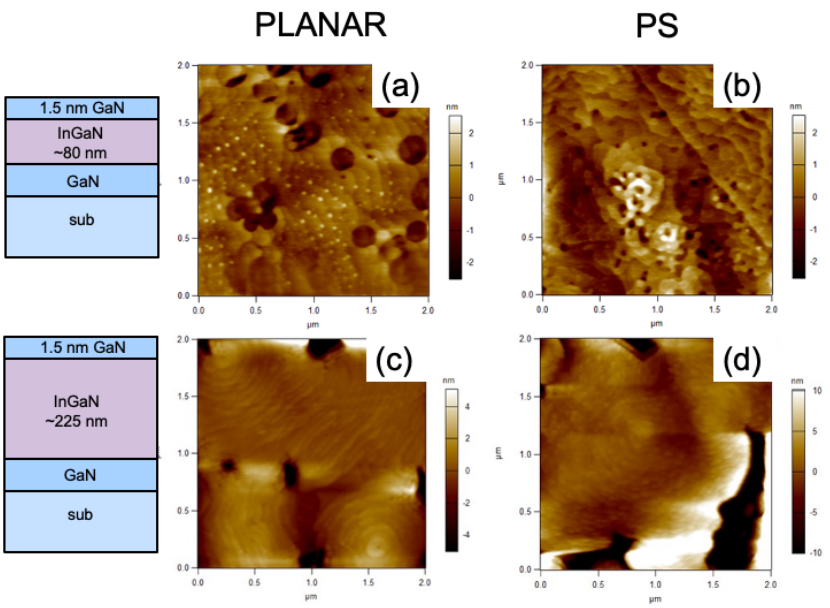

Figure 6-2: AFM micrographs taken for InGaN growth at Tc = 550 °C for (a) PA1A (80 nm InGaN grown on planar GaN),(b) PA1 (80 nm InGaN on PS), (c) IE3 (225 nm InGaN on planar GaN) and (d) PA2 (225 nm InGaN on PS). Cooresponding sample structures are shown to the left of the AFMs and the substrate is indicated above the top two AFMs. Surface RMS values for PA1A, PA1, IE3 and PA2 were found to be 1.46, 1.05, 2.03 and 5 nm respectively.

Although the surface morphology of PA2 is not considered 'device-quality' it is important to note the enhanced relaxation facilitated by growth on PS and the corresponding increase in In-composition. Comparing 80 nm of InGaN on planar GaN and PS, relaxation went from 7% to 36.4%. This clearly demonstrating the compliance of the porous tiles just as had been done in past with MOCVD InGaN [31], [180], [181], [187], [187]. The enhanced relaxation also leads to an increase in In-composition as in the case of PA2 where the In-uptake doubled compared to the same InGaN thickness on planar GaN. As was discussed in chapter 4, although higher temperature growth leads to enhanced step-flow growh and film quality, the lower lateral growth rate tends to enhance V-defect formation.

6.3 InGaN Grown at T_c = 530 ℃ (PB)

From chapter 4, decreasing the InGaN growth temperature is an obvious way to prevent the formation of V-defects when growing thick InGaN by PAMBE. Furthermore, the higher In-compositions which result from lower temperature InGaN growth can lead to a larger $x_{In,equiv.}$ for a given amount of relaxation. However, initiating growth with higher composition InGaN puts significant strain on the UID GaN compliant layer as the InGaN layer starts to relax. This could result in the generation of dislocations in the GaN compliant layer which may propogate into the InGaN layer thereby degrading film quality. In the following study, InGaN growth at T_c = 530 ℃ on PS is explored to see if a higher $x_{In,equiv.}$ can be achieved without degrading film quality and surface morphology.

Because the higher In-composition which results from lower temperature InGaN growth will result in more strain for a given thickness, the InGaN layer thickness was reduced compared to the previous study. Four growths were carried in this study: PB1A, 60 nm of InGaN grown on planar GaN; PB1, 60 nm InGaN grown on PS; PB2, 120 nm InGaN grown on PS; and PB3, 60 nm of InGaN grown on PB1 (60 nm InGaN on PS). For PB3, 3 nm of GaN was grown at 720 ℃ before lowering the temperature for InGaN growth resulting in a total GaN interlayer (IL) thickness of 4.5 nm. Growth temperature of the InGaN layers were all kept constant at 530 ℃ with an In and Ga-flux of approximately 7.7e-7 torr and 6.8e-8 torr respectively. All samples were capped with approximately 1.5 nm of GaN at the end of growth. Previous calibration runs (shown in appendix A.1) demonstrated that InGaN

growth at 530 ℃ under these conditions results in an In-composition of approximately 16% with a deviation of +/- 2 point-%.

Fig. 6-3 below shows the $\{\bar{1}\bar{1}24\}$ RSM scans for this study. The extracted relaxation values for PB1A (60 nm InGaN on planar), PB1 (60 nm InGaN on PS), PB2 (120 nm InGaN on PS) and PB3 (60 nm InGaN on PB1) were found to be 0 (fully strained), 13%, 60% and 50% respectively. Extracted In-composition for PB1A (60 nm InGaN on planar), PB1 (60 nm InGaN on PS), PB2 (120 nm InGaN on PS) and PB3 (60 nm InGaN on PB1) were found to be 11.6%, 17%, 20.3% and 18.3%. The calculated $x_{In,equiv.}$ values for PB1A (60 nm InGaN on planar), PB1 (60 nm InGaN on PS), PB2 (120 nm InGaN on PS) and PB3 (60 nm InGaN on PB1) were found to be 0%, 2.2%, 12% and 9.1%. Two InGaN peaks are observed in Fig. 6-3.d for PB3 (60 nm InGaN on PB1). The peak which is closest to the 100% strain line segment is likely from the initial 60 nm of InGaN growth (PB1) as it is in almost the same position as the peak observed in the RSM for PB1 (Fig. 6-3.b). The second, more elongated peak in PB3 which is centered approximately half-way between the 100% strained line segment and the 100% relaxed line segment is likely top 60 nm InGaN layer (PB3 growth). Thus the top layer relaxes more than the bottom InGaN layer when the two layers are seperated by a GaN IL. Furthermore, considering the higher relaxation and In-uptake observed in PB2, which has the same net InGaN thickness, the GaN interlerlayer in PB3 appears to restrict relaxation – PB3 is only 50% relaxed compared to PB2 (no GaN IL) which is 60% relaxed. The XRD (0002) InGaN $FWHM_{(0002),InGaN}$ values for PB1A (60 nm InGaN on planar), PB1 (60 nm InGaN on PS), PB2 (120 nm InGaN on PS) and PB3 (60 nm InGaN on PB1) were 237 arcseconds, 384 arcseconds, 731 arcseconds and 875 arcseconds respectively. The higher

$FWHM_{(0002),InGaN}$ for the thicker InGaN layers (PB2 and PB3) on PS may be related to the high amount of relaxation either by deformation (plastic) or by a strain gradient due to elastic relaxation.

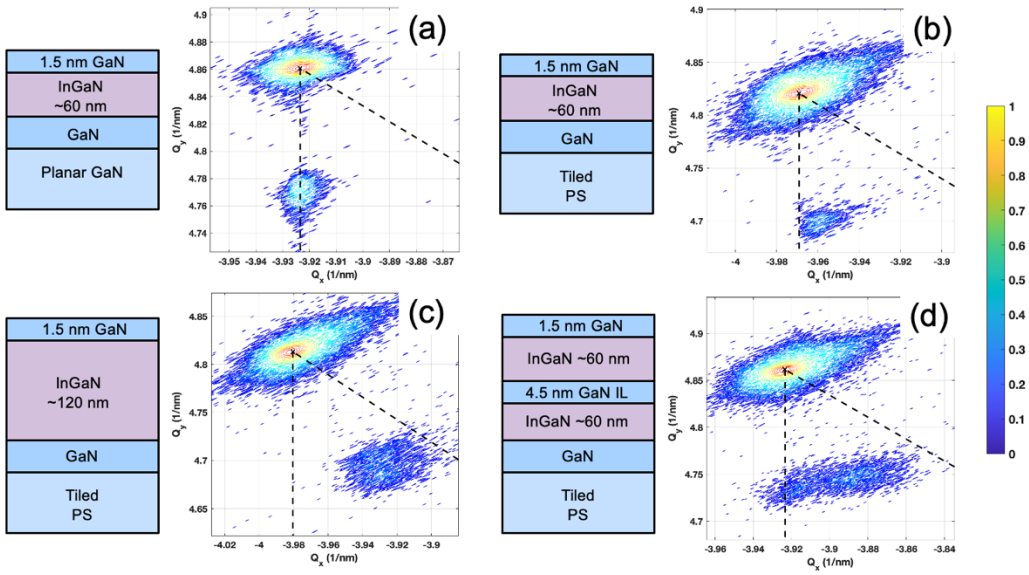

Figure 6-3: $\{\overline{11}24\}$ XRD RSM scans taken for (a) PB1A (60 nm InGaN grown on planar GaN), (b) PB1 (60 nm InGaN on PS), (c) PB2 (120 nm InGaN grown on PS) and (d) PB3 (60 nm InGaN grown on PB1 with a GaN IL). RSM color scale bar is shown on the far right. Corresponding sample structures are shown to the left of each RSM. In-composition extracted from these RSMs were found to be 11.6%, 17%, 20.3% and 18.3% for PB1A, PB1, PB2 and PB3 respectively. Extracted relaxation values for PB1A, PB1, PB2 and PB3 were found to be 0 (fully strained), 13%, 60% and 50% respectively.

2x2 μm^2 AFM scans were taken after each growth in this study which are shown in Fig. 6-4 below. Extracted RMS values for PB1A, PB1, PB2 and PB3 were found to be 0.796 nm, 1.167 nm, 2.038 nm and 1.515 nm respectively. The AFM for PB1A (Fig. 6-4.a), 60 nm of InGaN grown on planar GaN at at 530 ℃, exhibits spiral step-flow growth with a large number of small pin-holes on the surface, which like PA1, are likley related to dislocation networks from the underlying GaN-on-sapphire substrate – it is unlikely that dislocations were generated in the InGaN layer for this sample as the InGaN layer is fully strained to the GaN. The surface of PB1, 60 nm of InGaN grown on PS at 530 ℃, also has some pin-holes

but as in the case of PB1A, they also likely come from the underlying GaN and do not generate in the InGaN given the low $FWHM_{(0002),InGaN}$ values for these two growths. The surface morphology for PB2 (Fig. 6-4.c) posseses obvious step-flow spiral morphology however the step-terraces are not as defined as in the case of PB3 (Fig. 6-4.d). As was observed for the 530 ℃ InGaN growth study on planar GaN (chapter 4 Fig. 4-9), the lower growth temperature results in grainer surface morphology for thick layers (thicknesses significantly higher than h_c) which appears to carryover for InGaN growth on PS.

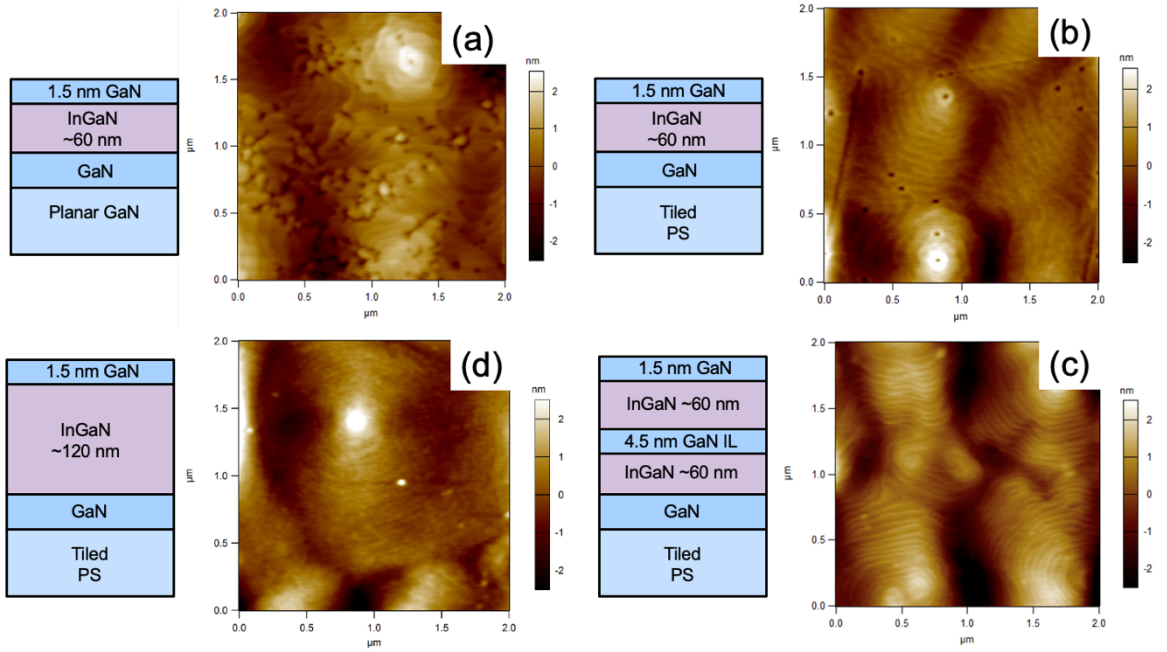

Figure 6-4: AFM micrographs for (a) PB1A, 60 nm InGaN grown on planar GaN, (b) PB1, 60 nm InGaN on PS, (c) PB2, 120 nm InGaN on PS and (d) PB3, 60 nm InGaN grown on PB1 (net InGaN thickness of 120 nm with GaN IL). Cooresponding sample structures are shown to the left of each AFM image. RMS values extracted from these AFMs were found to be 0.796 nm, 1.167 nm, 2.038 nm and 1.515 nm for PB1A, PB1, PB2 and PB3 respectively.

RT PL measurements were performed on PB2 and PB3 to see how the wavelength of the InGaN on PS shifted when compared to the standard GaN templates. RT PL scans shown in Fig. 6-5 were performed at a set stage position (i.e. not normalized to a set

intensity). The peak wavelegth of PB2 and PB3 were found to be 415 nm and 405 nm respectively. Clearly the sample with the higher $x_{In,equiv.}$ had the longest emission wavelength of 415 nm (PB2, $x_{In,equiv.}$ = 12%), however, the PL intensities were significantly lower than that of the GaN template (blue curve in Fig. 6-5). Taking that into consideration, these samples are meant to serve as substrates to grow MQW structures which would hopefully lead to significantly better emission. Therefore the broad, low intensity peaks seen in these two samples may not necessarly be deterimental to the device epi which would be grown on top of them.

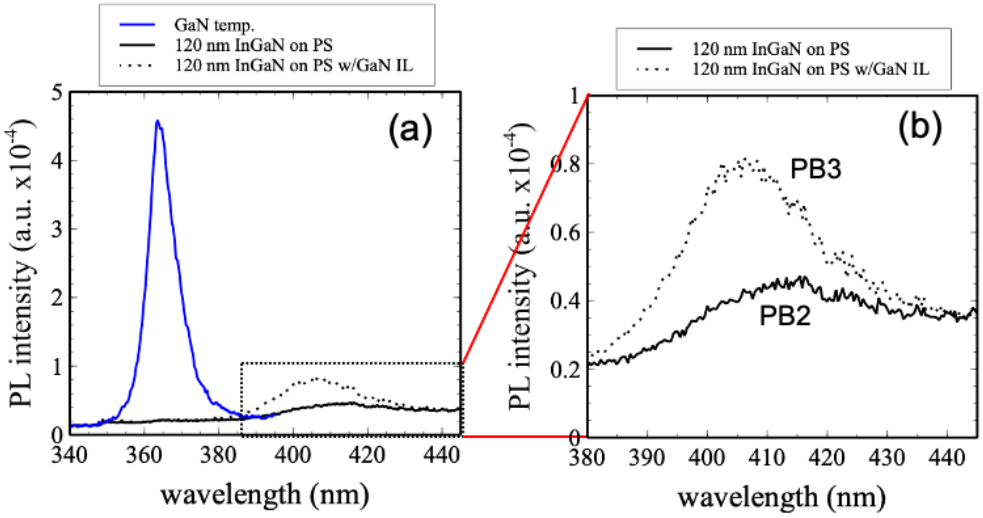

Figure 6-5: RT PL spectras using a 325 nm laser showing (a) PB2, 120 nm InGaN on PS (solid black curve); PB3, 60 nm InGaN grown on PB1 with a GaN IL (120 nm InGaN total – dotted black curve); and the peak from a standard MOCVD grown GaN template (blue curve). (b) close up of the PB2 and PB3 peaks. The PB2 peak is at approximatly 415 nm and the PB3 peak is at approximatly 405 nm

To better understand the quality of the relaxed InGaN layers in samples PB2 (120 nm InGaN on PS) and PB3 (60 nm InGaN on PB1), both samples were sent out for cross-section STEM imaging at the Univeristy of Michigan. Fig. 6-6 shows cross-sectional low angular annular dark-field (LAADF) STEM images, which show diffraction contrast with dislocations showing bright contrast, taken from the $[11\bar{2}0]$ zone axis for sample PB2 (Fig.

6-6.b) and PB3 (Fig. 6-6.a). In both cases no new dislocations were observed in the InGaN layers suggesting the relaxation facilitated by the porous underlayer was elastic. The vertical lines observed in PB3 (Fig. 6-6.a) originate from a curtaining effect which occurs during FIB milling of the cross-sections used for STEM imaging.

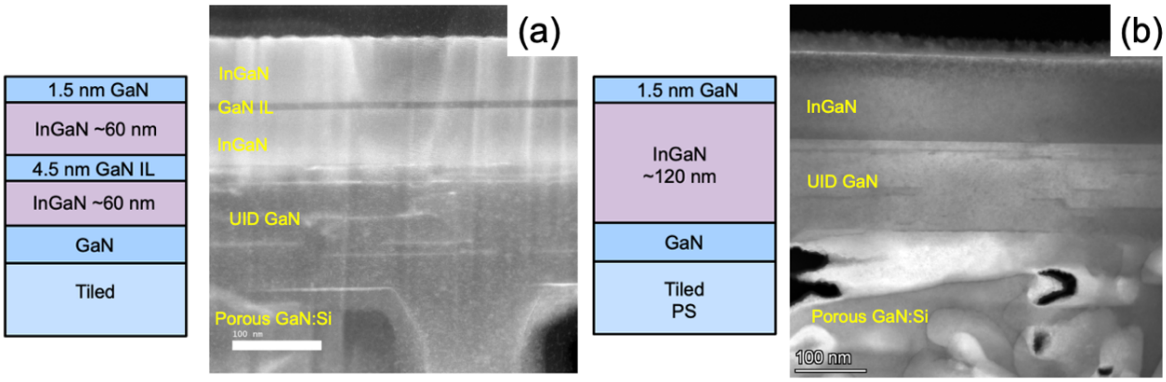

Figure 6-6: cross-section dark-field STEM images take one the [11$\bar{2}$0] zone axis for (a) sample PB3 (60 nm InGaN on PB1) and (b) sample PB2 (120 nm InGaN on PS) with corresponding sample structures to the left of each STEM image. STEM analysis done by Dr. Kai Sun at the University of Michigan.

Although we believe elastic relaxation to be the dominant relaxation mechanism for InGaN grown on PS in this study, the STEM images shown in Fig. 6-6 also suggest some plastic deformation in PB2 and PB3. The horizontal lines observed in the UID GaN layer between the porous layer and the InGaN layer were found to be pure edge component dislocations. These horizontal features appear to be both in the MOCVD grown UID GaN (100 nm) and the MBE grown UID GaN (30 nm) and may have formed during InGaN growth to relieve strain in the UID GaN layer. Although dislocations are not desirable for ultra-high-quality films, particularly for optoelectronics where they can act as leakage paths and recombination centers, these dislocations are confined to an area far from where the active regions of such devices will be and will likely not be detrimental to device performance. The dislocation lines seen in the STEM images in Fig. 6-6 do not appear to propagate into

the InGaN layer. Rather, they may be traveling along the basal plane until they terminate at the edge of the tile. Note that no defect formation in the GaN layers was observed in previous MOCVD experiments where the In-composition did not exceed 12%, posing less stress on the GaN compliant layer. We believe that the defect formation in the GaN layers observed in this study can be prevented through further process optimization, by for example grading the In-composition similar to past work by Däubler and Hestroffer et al., [150], [188].

In agreement with past work demonstrated by Pasayat et al., [31], [180], [187], samples PB2 and PB3 show promise as a pseudo-substrate. This work already demonstrates a higher corresponding $x_{In,equiv.}$ compared with past work by MOCVD (7.6% [181] compared to 12%). The spiral growth observed in Fig. 6-4 is common for MBE grown InGaN and although the spiral height observed in these samples is generally higher than what is observed for MOCVD grown InGaN, it has been shown that smoother surface morphology can be obtained by subsequent MOCVD regrowth [185]. V-defects, on the other hand, are far more difficult to eliminate by regrowth making MBE relaxed InGaN advantageous for pseudo-substrates.

6.4 In-Composition Step Grade (PC & PD)

Up to this point the highest $x_{In,equiv.}$ achieved without V-defects on the surface, or new dislocations in the InGaN layers is 12%. Although this is a significant improvement compared to past work by MOCVD it believed that a higher in-plane lattice constant can be achieved on PS. Mentioned previously, InGaN composition step-grades have been utilized

in the past by MBE InGaN on planar GaN to achieve relaxed InGaN substrates [188]. Although these films had a high density of dislocations it was shown that using the composition step-grade led to a reduction in pure edge-component dislocations compared to InGaN layers of a set composition [188]. This section will demonstrate a temperature-tuned compositional step grade on PS. The initial study presented here will demonstrate an evolution of relaxation and In-composition for subsequent layers grown on a two-step composition grade. In the later part, a 4-step composition grade, grown without interruption, will be shown.

Step-Grade with Characterization Between Steps (PC Study):

In the following study a two-step temperature-controlled composition grade is grown on PS and planar samples co-loaded in the same run. For the first run, PC1A and PC1 (planar and PS respectively), two InGaN layers are grown, 80 nm each, at 530 ℃ and 550 ℃ coorespoding to an x_{In} of 9% and 16% respectively and capped with 1.5 nm of GaN grown at 530 ℃. Following growth, both samples were characterized by XRD. The samples then underwent a solvent clean (3 min/2 min sonication in acetone/isopropal) followed by a 2 minute HF dip and 2 minute DI dip. The samples were then mounted and loaded back into the MBE buffer chamber, baked at 400 ℃ for an hour before being transferred to the main growth chamber. Following 3 nm of GaN growth at 720 ℃, the growth temperature was lowered to 530 ℃ for 60 nm of InGaN growth and then capped with 1.5 nm of GaN. These samples, named PC2A and PC2 cooresponding to growth on PC1A (planar) and PC1 (PS) respectively, were again characterized by XRD, cleaned using the same process described above, and again loaded back into the chamber and the same process used for PC2A and

PC2 was repeated (3 nm GaN + 60 nm InGaN at 530 ℃ + 1.5 nm GaN). This final growth, labeled PC3A and PC3 (growth on PC2A and PC2 respectively) was then characterized by XRD and AFM. The XRD RSM scans and the sample structure for PC(1-3)A and PC(1-3) are shown in Fig. 6-7 below. In-composition and relaxation values were extracted from the top InGaN layer (lowest peak in the RSMs). 2x2 μm^2 AFM micrographs for PC3A and PC3 are shown in Fig. 6-8 below.

For PC1A (planar) and PC1 (PS) the extracted In-composition values were found to be 15.3% and 21.2% respectively; relaxation values were found to be 7.6% and 51% respectively giving $x_{In,equiv.}$ values of 1.2% and 10.8% respectively. For PC2A (planar) and PC2 (PS) the extracted In-composition values were found to be 14.4% and 22.1% respectively; relaxation values were found to be 12.7% and 63% respectively giving $x_{In,equiv.}$ values of 1.8% and 13.8% respectively. For PC3A (planar) and PC3 (PS) the extracted In-composition values were found to be 14.4% and 22.3% respectively; relaxation values were found to be 11.8% and 68% respectively giving $x_{In,equiv.}$ values of 1.7% and 15.1% respectively.

Considering just the RSMs for the InGaN layers grown on planar GaN (PC(1-3)A), the higher composition top layers appear slightly more relaxed compared to the bottom higher composition InGaN layers. This is what had been previously reported by Hestroffer et al., for InGaN composition step-grades on planar GaN [188]. The layers further from the initial GaN/InGaN hetero-interface will always be more relaxed compared to the film closest to the hetero-interface. It can be assumed, however, that this incremental relaxation of the

top InGaN layers on planar GaN is facilitated by some plastic deformation. However, this is not the case for the InGaN step-grade on PS. Looking at Fig. 6-7.b, InGaN step-grade on PS (PC1) the initial lower In-composition layers relax fully (~100%) whereas the top (higher In-composition) InGaN layer relaxes 51%. For the subsequent InGaN regrowths on PS (PC2-3) there is an incremental increase in relaxation for the top InGaN layer, however, the lower InGaN layer goes past 100% relaxation becoming tensile strained to the top InGaN layers. It can be observed Fig. 6-7 that the initial InGaN layer in the step grade sits on the same horizontal reciprocal lattice position (Q_x) as the top InGaN layers. *This demonstrates that the initial InGaN layer in the step-grade becomes a 'secondary compliant layer' stretching to conform with the top InGaN layers*. This secondary-compliant effect was also observed in past work by Pasayat et al., for InGaN layers of different composition grown on PS by MOCVD [31].

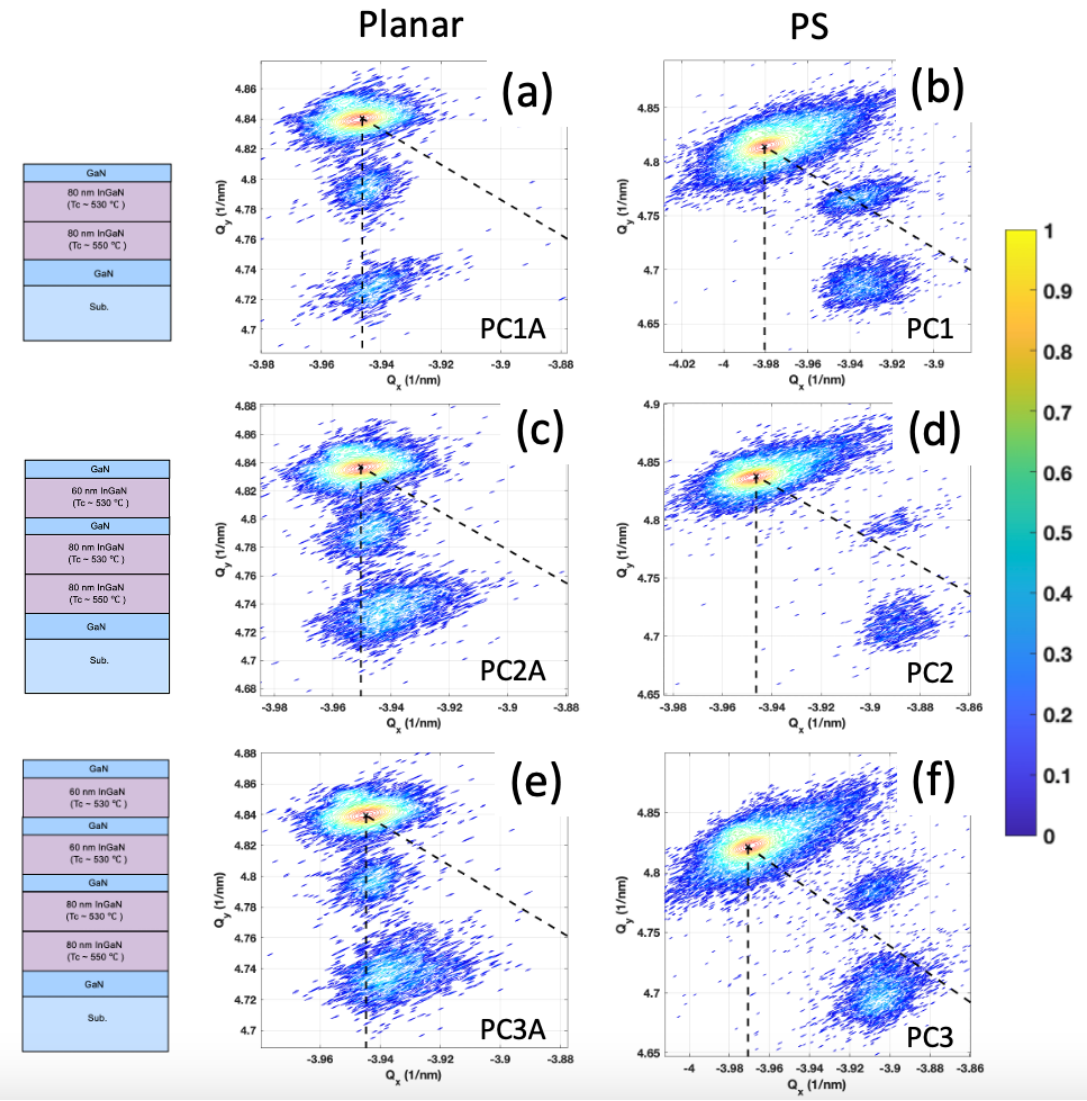

Figure 6-7: $\{\overline{1}\overline{1}24\}$ XRD RSM scans taken for (a) PC1A (planar) (b) PC1 (PS), (c) PC2A (planar) (d) PC2 (PS), (e) PC3A (planar) and (f) PC3 (PS). RSM color scale baris shown on the far right. Cooresponding sample structures are shown on the left. Extracted relaxation and In-composition values are shown in table 6-1.

From the 2x2 μm^2 AFM micrographs for PC3A and PC3 shown in Fig. 6-8 below, both the planar and PS samples show step-flow spiral growth. The step-terraces, however, are less defined than the other samples in this study which is characteristic of thick InGaN grown at 530 ℃. PC3A (step-grade on planar GaN) has a high density of pin-holes on the surface which may be associated with dislocations generated to relieve strain. The surface

RMS values extracted from the AFMs were 1.55 nm and 1.43 nm for PC3A and PC3 respectively.

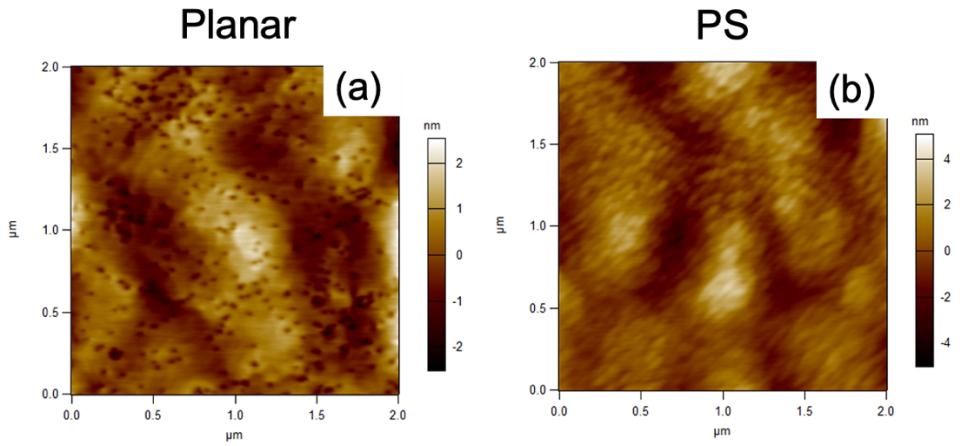

Figure 6-8: AFM micrographs for the temperature controlled In-composition step-grade on (a) PC3A (planar GaN), (b) PC3 (PS). RMS vales extracted from these scans were found to be 1.55 nm and 1.43 nm for PC3A and PC3 respectively.

Fig. 6-9.a and Fig. 6-9.b below shows a zoomed out (5x5 μm^2) AFM and an SEM image of the tiled surface at ~5000x magnification. From these figures there appears to be V-defects on the surface of the sample that were not seen in the first 2x2 μm^2 AFM scan shown in Fig. 6-8.b. These V-defects can be detrimental to device performance and make the justification for using MBE over MOCVD moot.

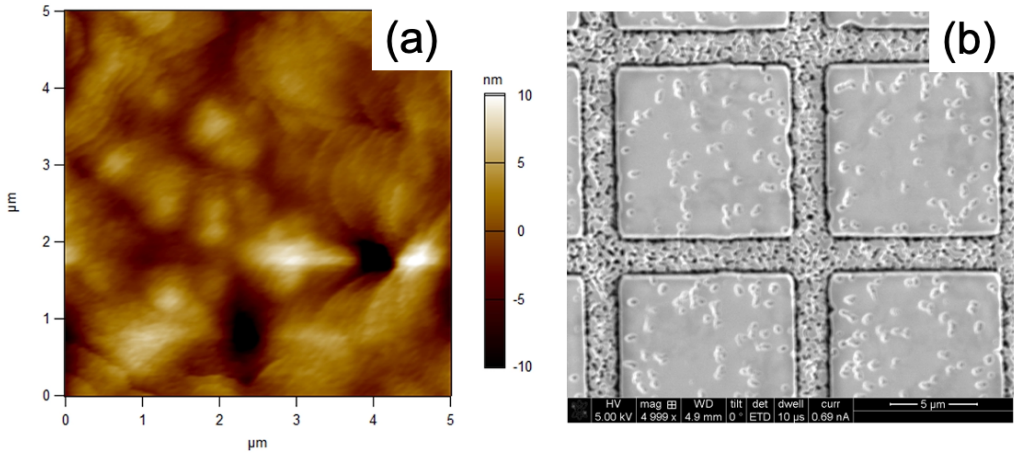

Figure 6-9: AFM micrographs for PC3 (temp controlled In-composition step-grade on PS) showing two V-defects in the bottom region of the image, and (b) 5000x magnification SEM image taken of the tiles showing multiple V-defects across multiple tiles.

Step-Grade Grown Without Interruption (PD Study):

It can be speculated that the formation of these defects is strictly due to strain relief from the thick composition step grade. This would imply that the highest $x_{In,equiv.}$ for InGaN on 10x10 μm^2 PS without generating V-defects is somewhere between 12% and 15% based on the results of PB2 and PC3. However, going back to chapter 2, where we see V-defects form during homoepitaxy of N-polar GaN-on-GaN (zero lattice mismatch) the generation of V-defects in this case was attributed to issues with the regrowth interface. In the case of PC3, there are three MBE regrowth interfaces. Each of these regrowth interfaces could potentially be the culprit behind the V-defects. This could be verified by cross-section TEM imaging of the tile, however, given the time and cost associsted with TEM an alternative method to test this theory would be to grow another step-grade without interrupting the growth between layers for ex-situ characterization (i.e. growing an entire step grade in one shot).

For sample PD1A and PD1, a 4-step temperature controlled composition step grade was grown on planar and co-loaded PS GaN respectively. The step-grade consisted of 50 nm of InGaN grown at 565 ℃, 50 nm of InGaN grown at 550 ℃, 50 nm of InGaN grown at 540 ℃, a 4 nm GaN IL grown to thermally desorb excess In, followed by two 50 nm InGaN layers sepperated by a 4 nm GaN IL grown at 535 ℃. The total InGaN thickness was 250 nm (not including the 5 nm GaN cap and two 4 nm GaN ILs). Using the aformentioned growth temperatures the corresponding In-compositions of each layer (based on the study done in chapter 4) starting with the bottom would be 6.2%, 11.2%, 14.5% and 16.2% (top two InGaN layers).

RSM scans for PD1A and PD1 are given in Fig. 6-10 along with the cooresponding structure. For PD1A (growth on planar GaN), the top InGaN peak had an In-commposition and relaxation of 20.3% and 13.5% respectively resulting in an $x_{In,equiv.}$ ~ 2.7%. For PD1 (growth on PS), the top InGaN peak had a In-commposition and relaxation of 24.8% and 64.4% respectively resulting in an $x_{In,equiv.}$ ~ 15.8%. Just as in the case of PC3, it can be seen from Fig. 6-10 that the bottom, lower In-compositon, layers act as secondary compliant layers stretching to conform with the top (higher In-composition) InGaN layers.

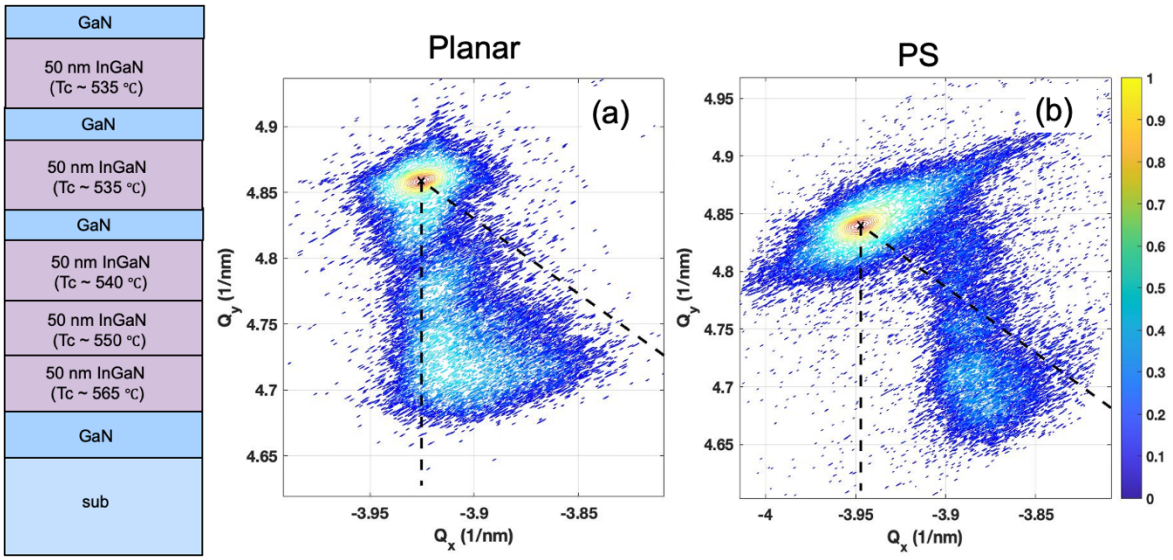

Figure 6-10: $\{\overline{1}\overline{1}24\}$ XRD RSM scans taken for (a) PD1A (step grade on planar) (b) PD1 (step grade on PS). RSM color scale bar is shown on the far right. Sample structures shown on the left. Extracted relaxation and In-composition values are shown in table 6-1.

2x2 μm^2 AFM micrographs for PD1A (step-grade on planar) and PD1 (step-grade on PS) shown in Fig. 6-11 below give surface RMS values of 1.84 nm and 2.48 nm for PD1A and PD1 respectively. As in the case of PA2 (225 nm InGaN on PS), PB2 (120 nm InGaN on PS) and PB3 (60 nm InGaN on PB1 – 120 nm net InGaN thickness with GaN IL), the spiral height is considerable high in PD1 (step-grade on PS) which has the highest $x_{In,equiv.}$ of any other sample in this study. This trend is reflected in Fig. 6-12 which shows. Surface RMS extracted from AFM as a function of x_{In}, relaxation, $x_{In,equiv}$ and net InGaN thickness. In the case of relaxation, x_{In} and $x_{In,equiv.}$, there is an obvious increase in surface RMS roughness, however surface RMS appears less dependnt on net InGaN thickness (Fig. 6-12.c). From this it can be speculated that the tall spiral height is associated with the higher In-composition, however this is subject to further study. The application of these pseudo-substrates for optoelectronics is dependent upon the ability to grow thick InGaN layers and MQWs by MOCVD. The tall spiral height resulting in surface RMS values >2 nm could impede MOCVD

regrowth. Furthermore, considering the growth temperatures used by MOCVD InGaN (>700 °C) the high In-compositions (>20%) of these PAMBE grown InGaN pseudo-substrates may result in decomposition of the PAMBE InGaN on the surface which in turn will negatively affect MOCVD regrowth. This is something that must be considered for future work.

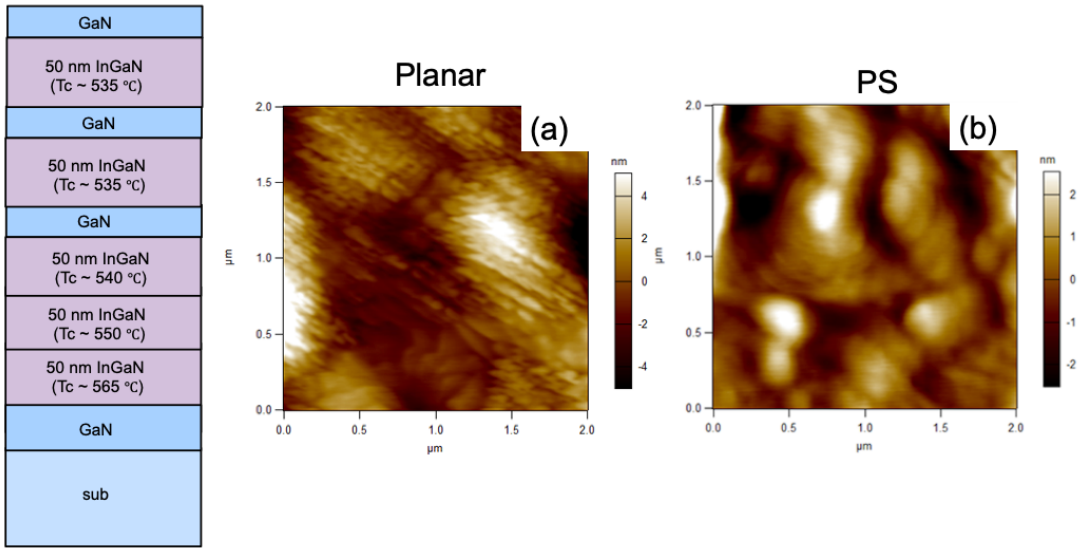

Figure 6-11: AFM micrographs for the temperature controlled In-composition step-grade grown in a single run for (a) PD1A (step-grade on planar) and (b) PD1 (step-grade on PS). RMS values extracted from these scans were found to be 1.84 nm and 2.48 nm for PD1A and PD1 respectively.

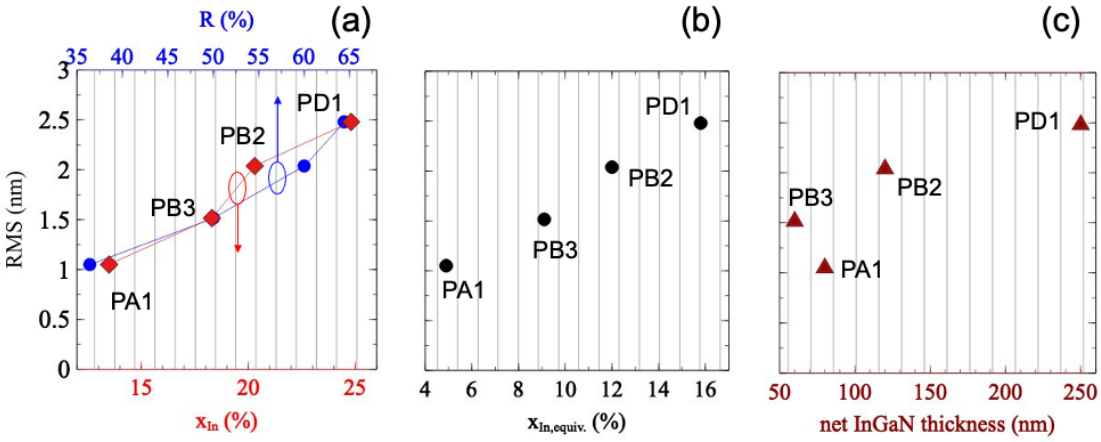

Figure 6-12: Surface RMS values extracted from AFMs as a function of (a) x_{In} (red diamond data points) and relaxation (blue circle data points), (b) $x_{In,equiv.}$ and (c) InGaN net thickness.

Fig. 6-13 below shows a 8000x magnification SEM image of one of the tiles showing no V-defects on the surface. These results make a compelling case for the previously stated theory in that the V-defects seen in PC3 were generated at one or more of the regrowth interfaces and not necessarily from dislocations created to relieve strain.

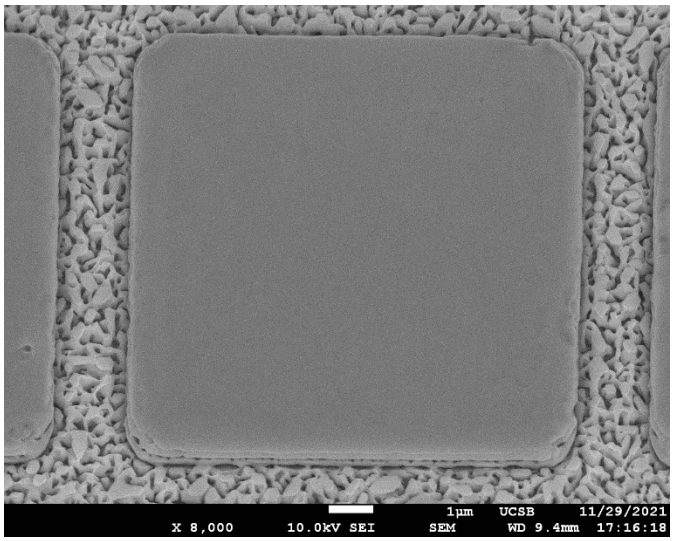

Figure 6-13: 8000x magnification SEM image of a tile from sample PD1 showing no V-defects on the surface. SEM imaging done by Boyu Wang.

RT PL was carried out on PD1A and PD1 (InGaN step-grade on planar and PS respectively). Fig. 6-14 below shows the RT PL scans for PD1A (step-grade on planar), PD1 (step-grade on PS) and the GaN template peak. Also included in Fig. 6-14 is the approximate location of where the yellow YL peak would be. As in the case of PB2 and PB3, the peaks for PD1A and PD1 are broad compared to the GaN substrate peak. As in the case of PB2-3, this broadness in the PL peaks may be attributed to an increase in In-uptake as a function of thickness due to relaxation of the InGaN on PS. It is our hope that growing MQWs on PD1 (step-grade on PS) may result in narrower MQW emission peak. The large intensity of the PD1 PL peak compared to the PD1A and the GaN template peak suggests that PD1 may be device quality, however further characterization needs to be performed.

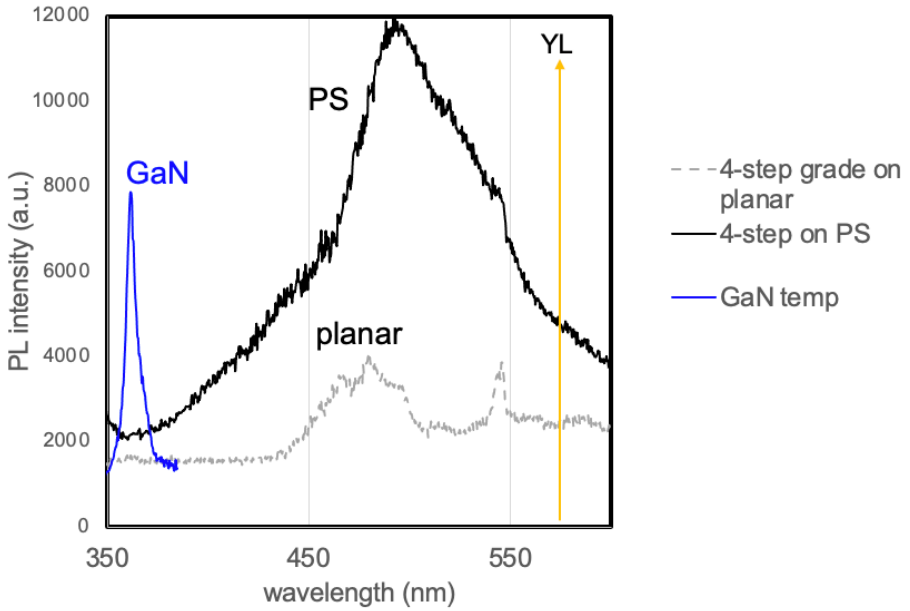

Figure 6-14: RT PL for the PD series: 4-step composition grade on planar GaN (PD1A - shown at the dotted grey curve) and on PS (PD1 - shown as the solid black curve). GaN peak from a standard MOCVD grown template is shown in solid blue. The yellow arrow indicates the approximate location of where the YL defect peak would be. Peak wavelegths for PD1 and PD1A are approximatly 497 nm and 482 nm respectively.

Cross-section STEM imaging was carried out on PD1 (step-grade on PS) to see if any new dislocations formed in the PAMBE grown InGaN. Fig. 6-15.a and 6-15.b below show a STEM bright-field (BF) cross-section image and a high angle annular dark-field (HAAFD) cross-section image respectively of a PD1 tile. The HAADF image in Fig. 6-15.b clearly differentiates the different InGaN layers grown in PD1 and shows the same edge-component dislocation in the UID GaN compliant layer which were observed in PB2 (120 nm InGaN on PS) and PB3 (120 nm InGaN with GaN IL). From Fig. 6-15.a a TD traveling from the substrate is seen propogating through the InGaN which is to be expected. More concerning, however, is the dislocation which appears to start at the interface between the 2nd and 3rd InGaN layers and propogates through the top two InGaN layers terminating at the surface. This, unfortunatly could be detrimental to device performance in terms of leakage current.

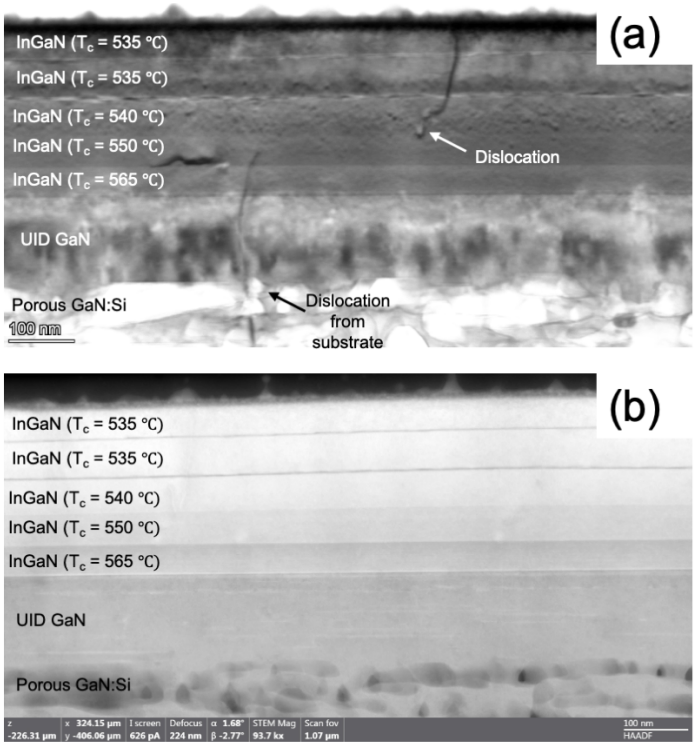

Figure 6-15: Cross-section STEM image taken one the $[\overline{1}\overline{1}20]$ zone axis for sample PD1 (4-step grade grown on PS). (a) STEM Bright-field (BF) image which shows a dislocation generated in the InGaN and (b) STEM HAADF image which shows the different layers more clearly and also shows the pure-edge component dislocations in the UID GaN layer under the tiles. STEM analysis done by Dr. Kai Sun at the University of Michigan.

To more accuratly understand the dislocation density is in PD1, plane-view STEM BF imaging was carried out on PD1 along with sample PB2 which has an $x_{In,equiv.}$ ~ 12%. For anlayzing dislocations and dislocation density, plane-view STEM is considered supperior to cross-section STEM. Fig. 6-16 below shows plane-view STEM BF images taken for sample PB2 (120 nm $In_{0.2}Ga_{0.8}N$ on PS – Fig. 6-16.a) and sample PD1 (4-step grade on PS – Fig. 6-16.b). From Fig. 6-16, clearly PD1 is heavily dislocated compared to PB2.

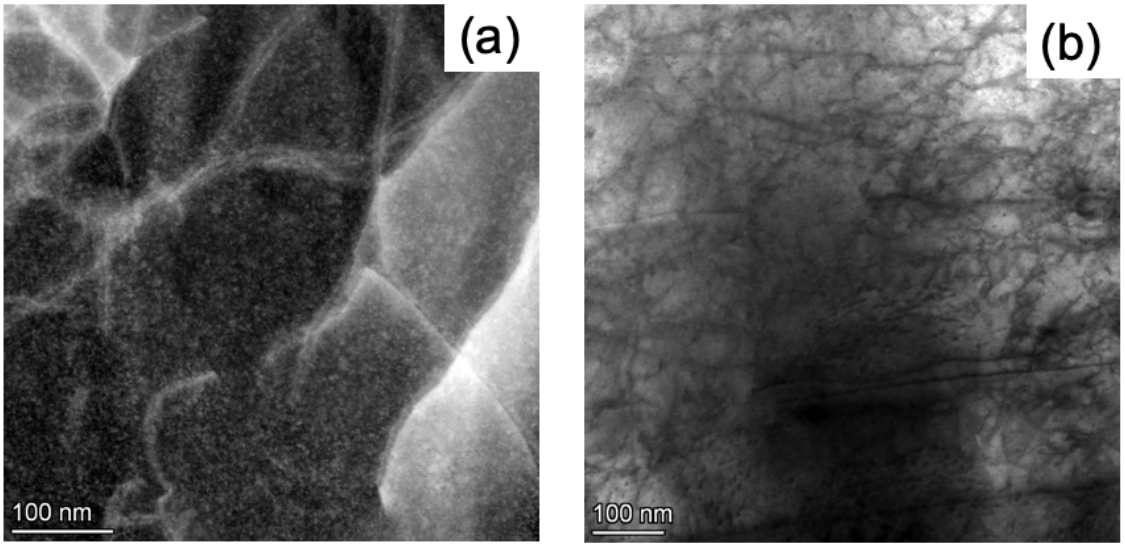

Figure 6-16: Plane-view STEM BF images using a ~200 nm foil thickness for (a) sample PB2 (120 nm $In_{0.2}Ga_{0.8}N$ on PS) and (b) sample PD1 (4-step grade on PS). From this, PD1 is highly dislocated compared to PB2. STEM analysis done by Dr. Kai Sun at the University of Michigan.

Table 6-1: Summary of experimental results from every study in this chapter on both PS and planar GaN. t_{InGaN} refers to the total InGaN thickness of the sample, including InGaN layers from previous runs as in the case of PB3, PC2, PC2A, PC3 and PC3A which were InGaN regrowths on previously grown InGaN layers. PB2 which had the highest $x_{In,equiv.}$ and was free of new dislocations in the InGaN is in bold.

sample name	substrate	T_c (℃)	t_{InGaN} (nm)	$FWHM_{(0002),InGaN}$ (arcsec.)	x_{In} (%)	R (%)	$x_{In,equiv.}$ (%)
PA1	PS	550	80	480	13.5	36.4	4.9
PA1A	planar	550	80	325	7.8	7	0.5
PA2	PS	550	225	602	19.8	80	15.8
IE3	planar	550	225	351	9.2	8	0.7
PB1	PS	530	60	384	17	13	2.2
PB1A	planar	530	60	237	11.6	0	0
PB2	**PS**	**530**	**120**	**731**	**20.3**	**60**	**12**
PB3 (GaN IL)	PB1 (PS)	530	120	875	18.3	50	9.1
PC1	PS	550/530	160	573	21.2	51	10.8
PC1A	planar	550/530	160	-	15.3	7.6	1.2
PC2	PC1 (PS)	530	220	394	22.1	63	13.8
PC2A	PC1A (planar)	530	220	559	14.4	12.7	1.8
PC3	PC2 (PS)	530	280	591	22.3	68	15.1
PC3A	PC2A (planar)	530	280	831	14.4	11.8	1.7
PD1	PS	550/530	250	644	24.8	64.4	15.8
PD1A	Planar	550/530	250	455	20.3	13.5	2.7

6.5 16% $x_{In,equiv.}$ Ceiling

Fig. 6-17 below gives a plot of $x_{In,equiv.}$ as a function of InGaN thickness for every sample in this study. The dotted black line in Fig. 6-17, shows an obvious saturation (or ceiling) in $x_{In,equiv.}$ as a function of InGaN thickness. The chief motivator behind using PAMBE

in lieu of MOCVD was in its ability to grow very thick InGaN layers without generating V-defects enabling MBE InGaN to push beyond the maximum $x_{In,equiv.}$ of 7.6% previously achieved by MOCVD [181]. Given the different growth conditions and layer architecture used in this study, this saturation in $x_{In,equiv.}$ appears independent of growth conditions and layer architecture suggesting the saturation in $x_{In,equiv.}$ is related to the pseudo-substrate itself. Clearly from the SEM image in Fig. 6-13 there is no significant sidewall growth of PAMBE InGaN using the growth conditions in this study. It is believed that to get beyond this ~16% $x_{In,equiv.}$ ceiling some change in the structure and/or growth conditions of the InGaN would have to occur. This, however, is subject to further study.

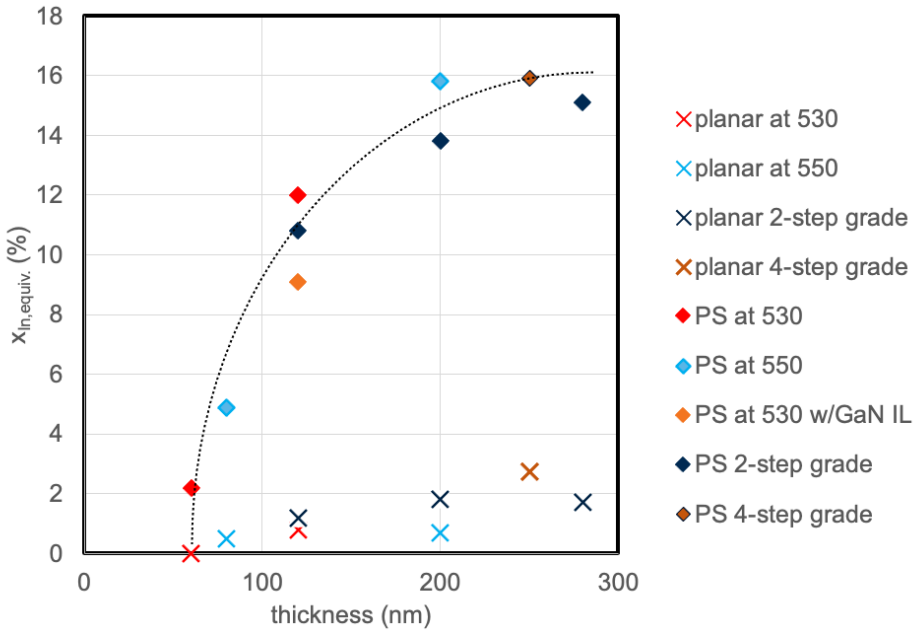

Figure 6-17: $x_{In,equiv.}$ as a function of InGaN thickness for growth on PS (represented as diamonds) and planar GaN (represented as x's). The black dotted line shows the overall $x_{In,equiv.}$ trend of the InGaN grown on PS which appears to have an approximate ceiling of 16% $x_{In,equiv.}$ under the explored experimental conditions.

6.6 Conclusion

In summary, this work demonstrates high-quality elastically relaxed PAMBE-grown InGaN on PS can be achieved with a surface morphology free of V-defects. For 120 nm of InGaN grown directly on PS a corresponding $x_{In,equiv.}$ = 12% was achieved far exceeding previous work by MOCVD which reported a $x_{In,equiv.}$ = 7.6%. STEM results confirmed that no dislocations were generated at the GaN/InGaN interface for samples grown on PS suggesting these films may be suitable for optoelectronic applications. An $x_{In,equiv.}$ = 15.8% was achieved using a temperature-controlled composition step-grade with a total thickness of 250 nm that was also free of V-defects, however cross-section and plane-view STEM imaging confirmed the presence of new dislocations in the InGaN layer. This relaxation of InGaN on PS is owed in-part to the compliant nature facilitated by the underlying porous GaN layer. When combining all the work done in this study, an $x_{In,equiv.}$ ceiling of approximately 16% was observed when plotting $\mathrm{x_{In,equiv.}}$ as a function of InGaN thickness. It was concluded that some change in growth conditions or structure would be necessary to break through this ceiling. The tall spiral height on the surface of PAMBE grown InGaN on PS is of concern for future regrowth of MOCVD layers and is subject to further study. Where past work by MOCVD grown InGaN on PS has already demonstrated the compliance of porous GaN, MBE offers thicker, higher In-composition InGaN without V-defects on the surface thus offering substrates with higher in-plane lattice constants which can be utilized for red and amber micro-LEDs.

7 Conclusion & Future Work

This work highlighted the advantages PAMBE has over more commercially acceptable nitride growth methods. Where MOCVD grown N-polar GaN must be grown on vicinal substrates, PAMBE grown N-polar GaN can be grown on on-axis GaN substrates. Although initial attempts of PAMBE N-polar GaN growth on bulk GaN resulted in the generation of V-defects on the surface, this was easily remedied by initiating growth with a thin layer of AlN thereby decoupling the substrate from the PAMBE-grown epi. Experimental evidence suggested that these V-defects were generated at the regrowth interface. For metal-polar InGaN, PAMBE enables thicker, and higher In-composition films compared to MOCVD without generating V-defects. Using PAMBE grown InGaN on PS an in-plane lattice constant equivalent to 12% In-composition InGaN was achieved which was significantly higher than what had been demonstrated by MOCVD. Using a composition step-grade on PS an in-plane lattice constant of 15.8% was achieved, however STEM imaging revealed new dislocations in the InGaN layer. With the knowledge acquired in the

N-polar GaN-on-GaN study, it was discovered that having multiple growth interrupts, for ex-situ characterization, when growing a composition-step grade led to a resurgence of V-defects. Growing a composition step-grade without interrupting growth in-between layers for post-situ characterization suppressed V-defects. Comparing the two studies it can be concluded that V-defects in PAMBE grown nitrides generate at "unclean" regrowth interfaces.

7.1 PAMBE for High-Frequency Power Amplifiers

The demonstration of high-quality N-polar GaN-on-GaN by PAMBE using the AlN initiation layer has already been utilized by other groups for growing HEMT structures which show record high 2DEG channel mobility [75]. It is believed that growing on low TDD GaN substrates will greatly improve efficiency in mm-wave power amplifiers. PAMBE has also been utilized for source-drain n+ GaN regrowth in the N-polar HEMT work done by UCSB which showed record high output power at 94 GHz [7]. Although the actual HEMT epi is grown by MOCVD, MOCVD grown source-drain contacts are not yet ideal for N-polar deep recess technology due to the high amount of lateral growth on the SiO_2 mask sidewalls resulting in a build-up of GaN at the edges of the channel [189]. Therefor PAMBE may yet play a pivotal role in the future of mm-wave communications.

7.2 PAMBE for Optoelectronics

Highlighted in Chapter 6, two obstacles exist for growing LED MQWs on PAMBE grown InGaN on PS: The high In-compositions (>20%) needed to attain the desired in-plane lattice constants for red micro-LEDs will be a challenge for MOCVD regrowth. MOCVD

regrowth requires growth temperatures well above the temperatures which would lead to thermal decomposition of the PAMBE grown high In-composition InGaN. This would require significant changes in the MOCVD growth recipes. Secondly, the tall spiral hillocks inherent in PAMBE grown InGaN will also be challenging for MOCVD regrowth. Both issues, however, could be remedied by growing the full LED structure by PAMBE. PAMBE, however, is not considered ideal for optoelectronics due to vertical leakage arising from metal-decorated TDs. Despite this, some groups have successfully grown LEDs by PAMBE [190].

The saturation in $x_{In,equiv.}$ at approximately 16%, which was shown in Fig. 6-17 in chapter 6, is another obstacle which may need to be addressed. Getting a higher in-plane lattice constant, free of new dislocations, will significantly improve LED efficiency. Mentioned earlier, this may be remedied by either making some novel adjustment to the InGaN layer structure or growth conditions. Pasayat et al., demonstrated that the relaxation could be tuned by scaling the tile size [178]. Thus smaller tiles may lead to a higher $x_{In,equiv.}$.

The future of porous GaN tiles being used in micro-LED display technology will likely be dependent on whether it can be utilized for monolithic integration of RGB (all three colors on one substrate). Although micro-LED mass-transfer technology has matured over the last decade, many companies are already demonstrating monolithic integration of RGB [191]. One such company, Plessey in Devon U.K., which claimed full RGB monolithic integration [192], announced in 2020 that they would be partnering with Facebook to develop their future AR/VR display technology [193]. Lumiode, a New York based startup

working in micro-LED display technology has also demonstrated monolithic integration of RGB [194]. The Cambridge-based startup, Porotech, claims full RGB integration on a single wafer using their porous GaN technology [195], however it is not known if they are utilizing porous GaN for relaxation.

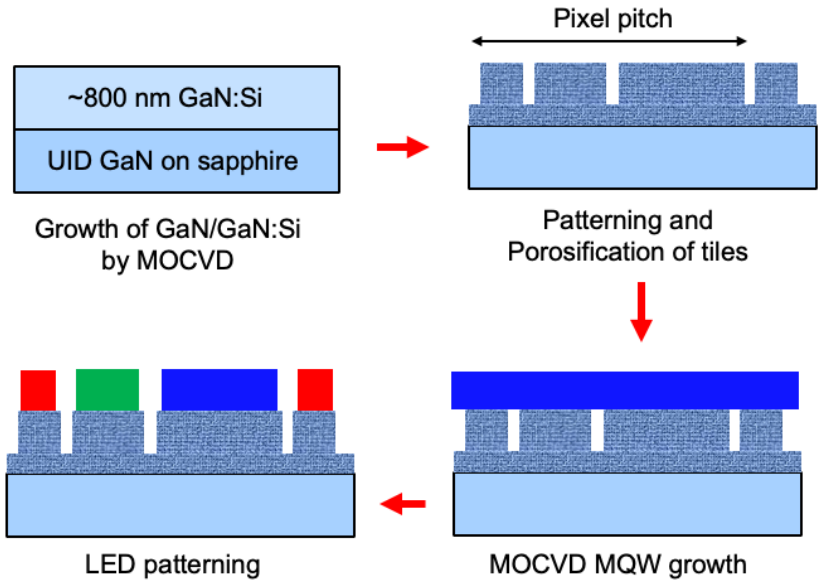

Figure 7-1: Proposed process flow for obtaining RGB monolithic integration using a single MOCVD MQW growth on tiles with varying sizes.

Monolithic integration of RGB using porous tiles may be achieved by doing a single MOCVD MQW growth on a substrate with varying tile sizes (i.e. increasing the aspect ratio thereby increasing the free-surface to promote relaxation) such as what is illustrated in Fig. 7-1. Discussed earlier, Pasayat et al., demonstrated a red-shift in EL wavelength when decreasing the tile width from 20 μm to 8 μm corresponding to an EL wavelength of approximately 525 nm and 560 nm respectively at a current density of 10 A/cm^2. This small of a red-shift as a function of tile size, however, may not be sufficient to get RGB from a single MQW growth. Not considering how small the red micro-LED tile would have to be, the width of the blue micro-LED may have to be significant which would result in a pixel

pitch too large for AR/VR applications. Doing multiple growths with different MQW conditions may also work, however, this would require multiple lithography and MOCVD growth steps which greatly increase the cost of processing. Furthermore, the MOCVD lateral growth rate on an SiO2 mask for multiple growth and lithography steps would pose a challenge to LED processing.

Although commercial MBE systems are still far from achieving the same throughput as current production MOCVD systems, there has been significant progress in production MBE systems. VEECO's Gen 2000 and the Riber MBE 6000 systems are both capable of running multiple 4" or 6" wafers in a single run [196], [197]. The work presented in this thesis highlighting the benefits of PAMBE nitride growth may engender a ramp-up in production MBE technology.

Appendices

The purpose of the following sections are for the reader to better understand the Varian Gen 2 PAMBE system used in this thesis. Future growers using this system will benefit greatly from these appendices. PAMBE growth does vary from system to system and knowing results from previously unpublished studies will greatly reduce the probability of re-repeating redundant experiments. For more information pertaining to GaN growth rate calibrations (GRCs), Al-composition studies and C-doping studies performed with this system, the author suggests to review the appendix section of reference [8]. A more comprehensive overview of the Varian Gen 2 system used for nitride growth at UCSB can also be found in the thesis by B. McSkimming [198].

A.1: InGaN Composition Repeatability

When considering changes in composition due to CPE for InGaN on PS compared to InGaN on planar GaN, the In-composition repeatability should be known. Not knowing the run-to-run deviation in In-composition for a given system may lead to false conclusions regarding how relaxation affects changes in In-uptake. 12 InGaN growths on planar GaN were carried out over a period of 18 days. Every growth was characterized by (0002) $\omega -$

2θ XRD scans to obtain In-composition. Using the plasma conditions and cell fluxes described in section 4.6, five growths were performed at a growth temperature of 530 ℃, and six growths were carried out at 550 ℃ all at different thicknesses ranging from 30 nm to 225 nm. Fig. A-1.a below shows In-composition as a function of time (i.e. date of growth) and Fig. A-1.b gives In-composition as a function of thickness.

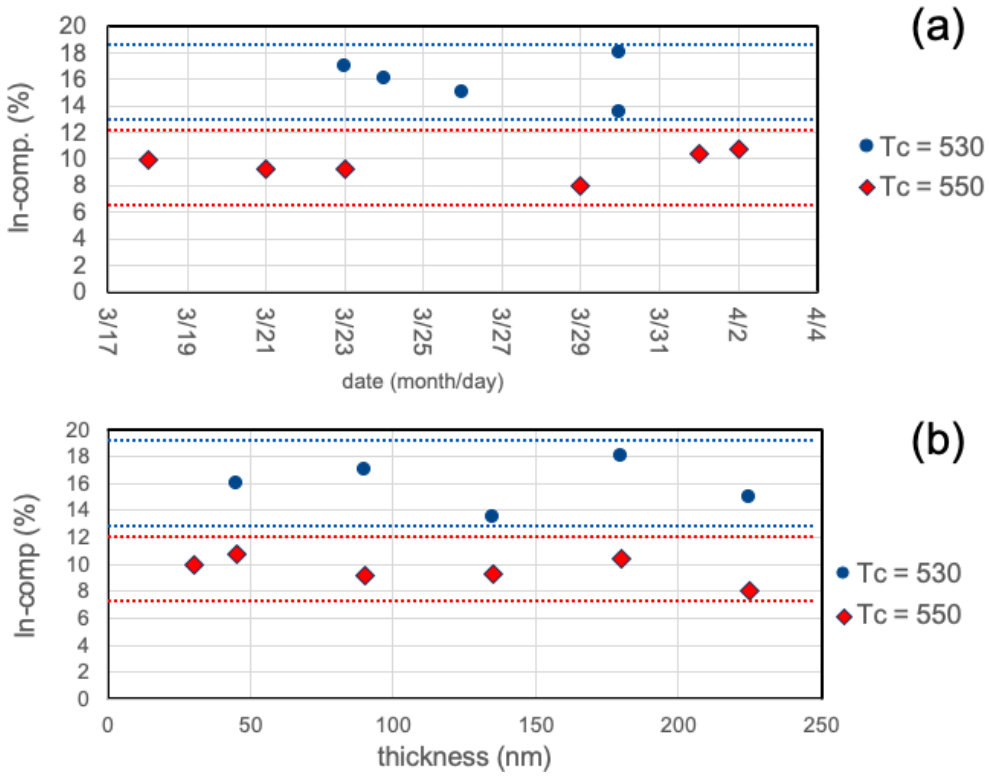

Figure A-1: (a) Plot of In-composition over time (18 days) and (b) plot of In-compositions as a function of thickness. Data in plot (a) is the same data in plot (b). Blue circles represent samples grown at 530 ℃ and the red diamonds represent samples grown at 550 ℃.

From both plots in Fig. A-1 it can be concluded that there is no visible trend in In-composition as a function of time or thickness. From this data it was found the average In-composition at a growth temperature of 530 ℃ was 16% with a +/- 2 point-% deviation, and at a growth temperature of 550 ℃ the average In-composition was 9% with a +/- 1.5 point-% deviation. Give the fluxes were constant for each growth, these deviations may be

attributed to incremental changes in the plasma source or possibly changes in growth temperature. It should also be re-emphasized that the substrate temperature was taken from the car (T_c) and not from a pyrometer.

A. 2: Sidewall Growth on PS Using Ultra-Low Growth Temperatures

Early work of InGaN grown on PS was carried out at significantly lower growth temperatures. In this study 200 nm of InGaN was grown on PS at a T_c of 485 ℃ (see Fig. A-2.a). At these low growth temperatures, cell fluxes also had to be adjusted. A Ga-flux and In-flux of 1.15e-7 torr and 5.75e-7 torr were used respectively. Just as in chapters 4 and 6, 300 watt, 1 sccm N_2 plasma conditions were used which resulted in an InGaN growth rate of approximately 1.9 nm/min. While the relaxation, In-composition and $x_{In,equiv.}$ extracted from the RSM (shown in Fig. A-2.b) was significant (92%, 28% and 26% respectively) the InGaN was found to be heavily dislocated as shown in the cross-section STEM image in Fig. A-2.c.

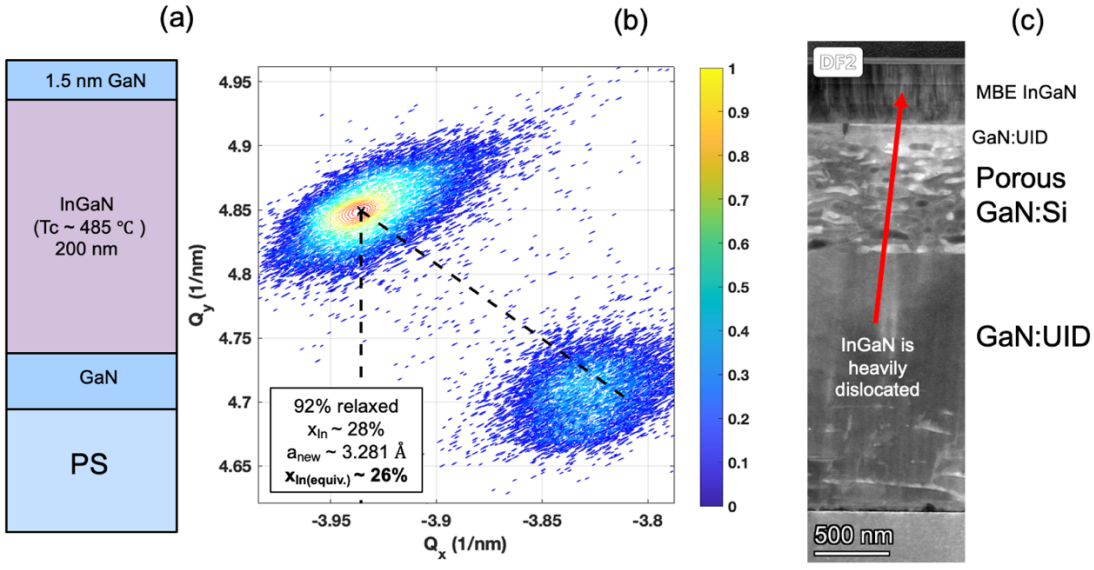

Figure A-2: (a) sample structure (b) $\{\overline{1}\overline{1}24\}$ XRD RSM plot and (c) cross-section STEM image of LT InGaN grown on PS. Inset in the RSM shows relaxation, x_{In}, a_{new} and $x_{In,equiv.}$ extracted from the RSM. STEM analysis was done by Dr. Kai Sun at the University of Michigan.

Although the InGaN was heavily dislocated, the AFM micrographs taken of the sample revealed a large amount of growth on the a-plane tile sidewall which is shown in Fig. A-3.a. A $2x2\ \mu m^2$ AFM was also taken of the tile (see Fig. A-3.b) which showed spiral growth and a surface RMS value of 2.05 nm. Mentioned previously in chapter 4, the lower growth temperature facilitates enhanced lateral growth which led to suppression of V-defects. In this case, the a-plane side of the tile exhibited a high amount of material buildup at the edges in addition to sidewall growth. This enhanced growth on the a-plane compared to the m-plane was also demonstrated by Pasayat et al., for coalesced AlGaN on PS grown by MOCVD [199].

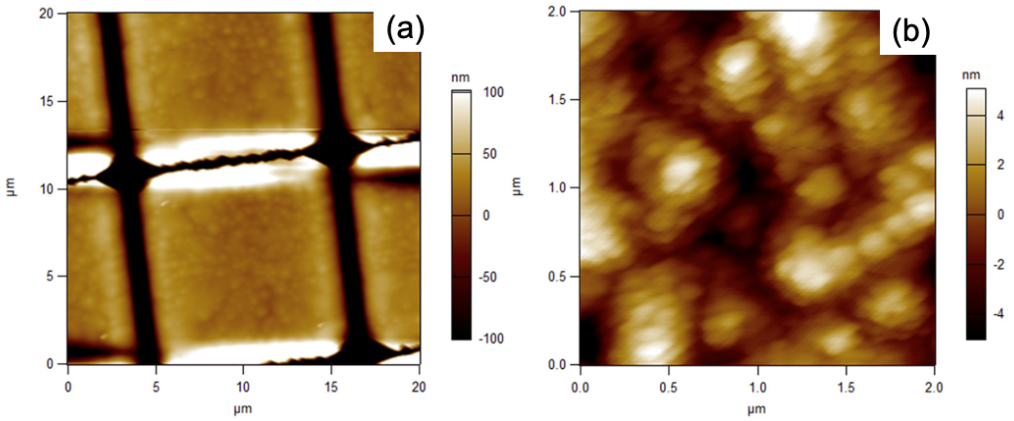

Figure A-3: (a) AFM micrograph showing significant growth on the a-plane sidewalls and (b) AFM micrograph of the tile surface. Surface RMS roughness extracted from the AFM was approximately 2.05 nm.

Although this sample was heavily dislocated (significantly more than sample PD1) and is therefore unfit for device applications, the lateral sidewall growth provokes some interest for future work. Suppressing the dislocations seen in Fig. A-2.c at this low of a growth temperature would require significant adjustments to the active N-flux and the Ga-

flux. Fully coalesced tiles would indeed be advantageous for making substrates for commercial applications.

A. 3: AlN Homoepitaxy Study

A significant amount of time and resources were spent on developing high quality metal-polar AlN grown on low-dislocation density AlN substrates. Instead of growing AlN at GaN growth temperatures using Ga as a surfactant, such as what was demonstrate in chapter 2 using the AIL for N-polar growth, this study utilized high temperature AlN growth without any Ga-flux. In the first study, Al-flux was varied to determine metal-rich conditions. In the next part, an Al-polishing treatment was performed on the AlN substrate to prior to growth to further improve film quality and surface morphology.

Al-Flux Study:

Plasma conditions for this study were 300 watts, 1 sccm N_2 which resulted in an AlN growth rate of approximately 4.8 nm/min. In the first study, the growth temperature was set to 780 ℃, measured by an optical pyrometer. Al-flux for samples AI1, AI2 and AI3 were 1.05e-7 torr, 2e-7 torr and 4.8e-7 torr respectively. Approximately 100 nm of AlN was regrown on AlN-on-SiC. Substrates used in this initial study were MOCVD grown AlN on SiC provided by Chris Zollner of Prof. Steve DenBaar's Group at UCSB. Table A-1 below shows the details of each growth including (0002) XRD $\omega - scan$ FWHM ($FWHM_{(0002),AlN}$) values measured for each sample after growth. Fig. A-4 below shows the $2x2\ \mu m^2$ AFM micrographs for AI1-3. The $FWHM_{(0002),AlN}$ values for AI1-3 were found to be 444 arcseconds,

640 arcseconds and 380 arcseconds respectively. The bare substrate had a $FWHM_{(0002),AlN}$ value of 244 arcseconds. Post-growth optical microscope (OM) analysis reviled no metal droplets on AI1, however AI2 and AI3 did have some droplets on the surface indicating that AI1 was perhaps grown under slightly N-rich conditions. The AFMs in Fig. A-4 clearly show tall spiral features for AI1. AI2 had a high density of spirals, however the spiral height is significantly lower compared to AI1. AI3 has more than an order of magnitude lower spiral density with very well defined long step terraces. The surface morphology and small $FWHM_{(0002),AlN}$ for AI3 suggests that 4.8e-7 torr is adequate Al-flux for AlN growth at these temperatures. The presence of droplets on the surface of samples AI3 and AI2 suggests Al-flux could be reduced below 4.8e-7 torr slightly and/or growth temperature could be increased slightly while still maintaining good film quality and surface morphology.

Table A-1: Growth conditions and experimental results for AI1-3

Sample	BEP_{Al} (torr)	$FWHM_{(0002)}$ (arcseconds)	RMS (nm)	Droplets (Y/N)
Substrate	-	244	0.239	-
AI1	1.1e-7	444	0.670	N
AI2	2e-7	640	0.437	Y
AI3	4.8e-7	380	0.391	Y

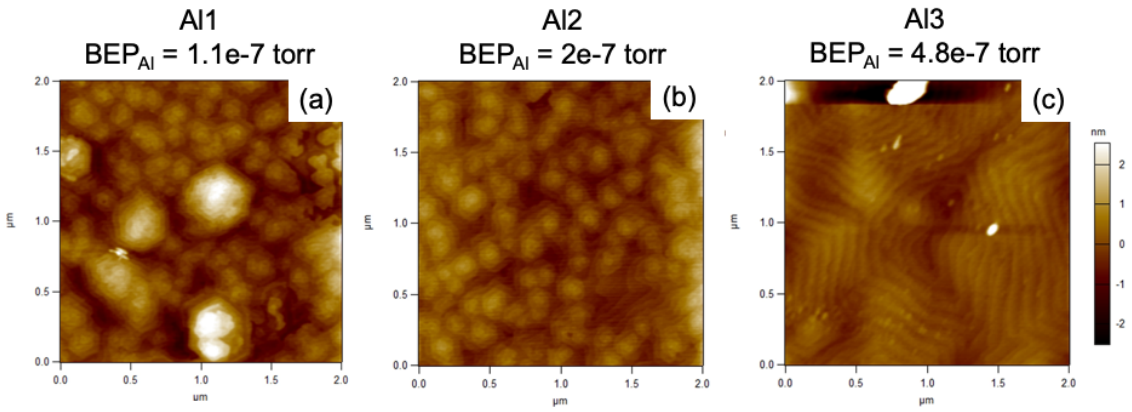

Figure A-4: AFM micrographs taken for (a) AI1, BEP$_{Al}$ = 1.1e-7 torr, (b) AI2 BEP$_{Al}$ = 2e-7 torr and (c) AI3 BEP$_{Al}$ = 2e-7 torr. RMS values extracted from the AFMs were found to be 0.67 nm, 0.437 nm, and 0.391 nm for AI1, AI2 and AI3 respectively.

Al-Polishing:

A major issue with bare AlN surfaces is oxidation. Chemical cleaning of AlN prior to growth can help, however the surface can still oxidize when loading into the MBE chamber before starting a growth. K. Lee et al., demonstrated an Al-polishing step prior to AlN regrowth that greatly improved surface morphology and film quality [200]. In this second study, low dislocation (<1e5 cm^{-2}) AlN substrates were used to demonstrate how Al-polishing improves surface morphology. To reduce the probability of the samples slipping during the high temperature growth, 500 nm of Ti by electron-beam evaporation was deposited on the backside of these substrates prior to growth to improve adhesion to the In. Sample AI4 was transferred into the main chamber and heated up to 930 ℃ and baked for 10 minutes for an in-situ bake. Following the in-situ bake, the substrate temperature was reduced to 900 ℃ and exposed to an Al-flux of 3.17e-7 torr for 30 second intervals and allowed to thermally desorb. This was repeated 10 times. The sample was removed from the chamber and characterized by AFM. A second sample, AI5, underwent the same Al-polishing step, however, following the Al-polishing the sample was cooled down to 800 ℃

and 100 nm of AlN was grown on it using a BEP_{Al} ~ 3.17e-7 torr. The RHEED intensity profile for one of the Al-polishing steps is shown in Fig. A-5 which shows a clear drop in intensity as a function of time when the Al-shutter is open and a corresponding increase in intensity approximately 28 seconds after the Al-shutter was closed indicating a complete thermal desorb of the Al from the surface.

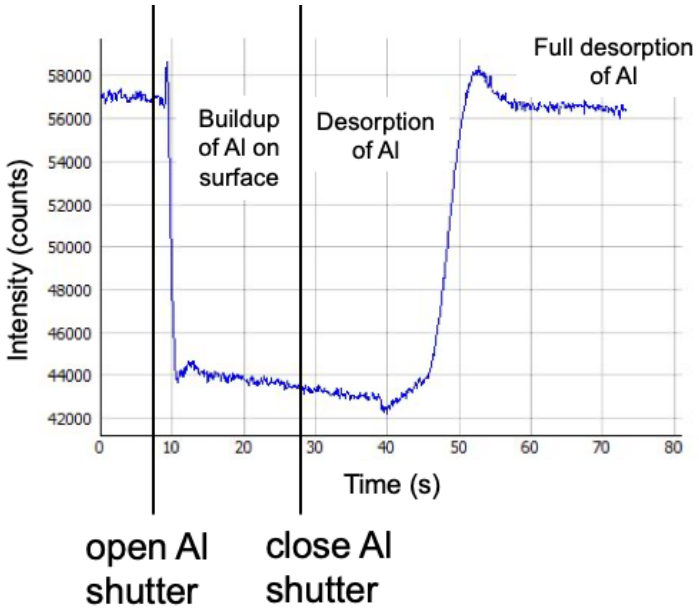

Figure A-5: RHEED intensity as a function of time showing one of the Al-polishing cycles. Vertical lines running through the graph indicate when the Al-shutter was opened and closed.

AFM images were taken on AI4, AI5 and the bare substrate which are all shown in Fig. A-6 below. Surface RMS values extracted from the AFMs for the substrate, AI4 and AI5 were 0.12 nm, 0.10 nm and 0.25 nm respectively. The small features on the surface of the bare substrate (Fig. A-6.a) may be attributed to surface oxides and hydroxides such as what was observed by Lee at al., [200]. Clearly from Fig. A-6.b these features are eliminated as a result of the in-situ Al-polishing revealing smooth periodic step-terraces. The surface of

AI5, 100 nm of PAMBE grown AlN on AlN, following in-situ Al-polishing, revealed smooth undulated step-flow morphology.

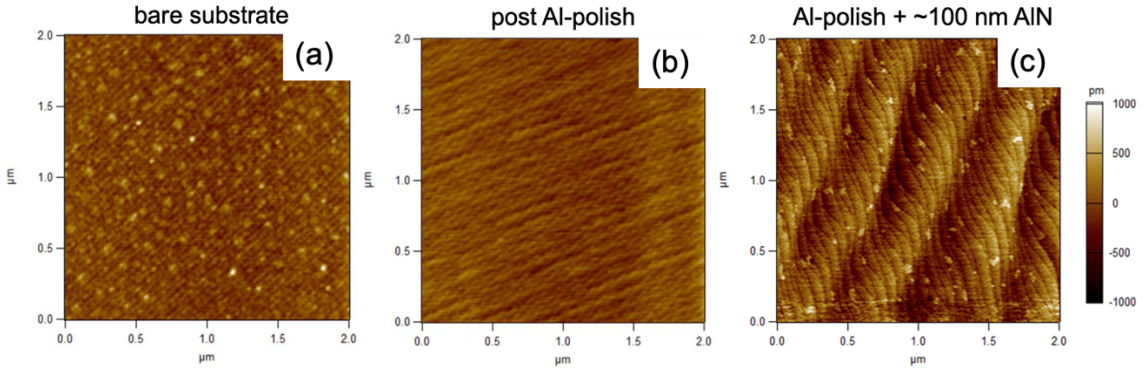

Figure A-6: AFM micrographs taken for (a) bare low TDD bulk AlN substrate (b) AI4, substrate after in-situ bake and Al-polishing and (c) AI5, sample subjected to in-situ bake and Al-polishing followed by 100 nm of AlN growth. Surface RMS values extracted from the AFMs for the substrate, AI4 and AI5 were 0.12 nm, 0.10 nm and 0.25 nm respectively.

The results of this study show how high-temperature growth using excess Al instead of Ga can be utilized for high-quality AlN growth. It was also demonstrated that performing an Al-polishing step at 900 ℃ can improve surface morphology by stripping the surface of any oxides which may accumulate while exposed to atmosphere. These results should be very helpful for those who wish to grow AlN on bulk AlN by PAMBE.

A. 4: N-polar InN Growth on Vicinal GaN-on-Sapphire Templates

In a separate study, not previously discussed in this thesis, growth of N-polar InN on miscut GaN-on-sapphire substrates was explored. The following growth of N-polar InN grown on a miscut GaN-on-sapphire template was carried out at a T_c of 440 ℃ using an In-flux of 4.5e-7 torr. Plasma conditions used were 300 watts 1 sccm N_2 which resulted in an InN growth rate of approximately 4.1 nm/min. Approximately 41 nm of InN was grown; thickness was verified by an (0002) XRD $\omega - 2\theta$ scan shown in Fig. A-7.b. Fig. A-7.a shows

a $5x5\ \mu m^2$ AFM micrograph taken of the sample after growth which had a surface RMS value of 2.22 nm. An (0002) ω –scan was taken for the InN which had a FWHM of 620 arcseconds (see Fig. A-7.c).

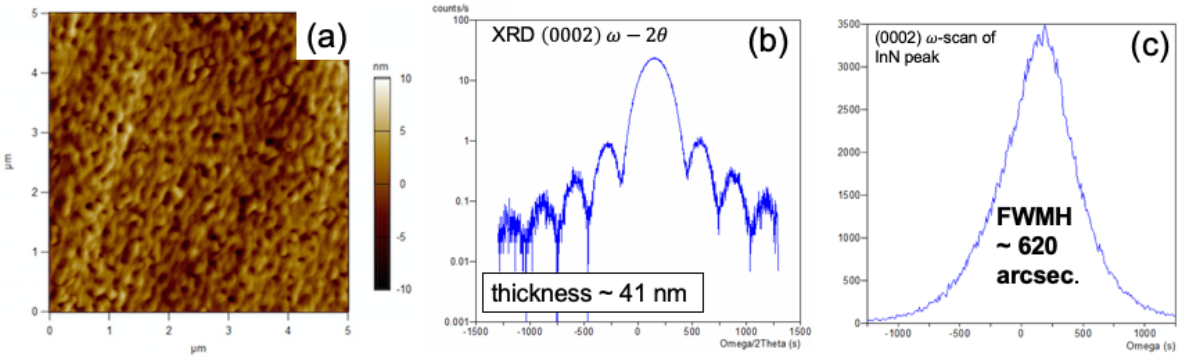

Figure A-7: (a) AFM micrograph taken for 41 nm of InN grown on a MOCVD grown miscut GaN-on-sapphire template along with corresponding (b) (0002) XRD $\boldsymbol{\omega - 2\theta}$ scan and (c) (0002) InN $\boldsymbol{\omega}$ –scan. Surface RMS extracted from AFM was found to be 2.22 nm.

The low temperatures needed for InN growth limits how smooth the surface morphology can be. Furthermore, given the InN critical thickness for relaxation is less than a few monolayers when grown on GaN, it can be well assumed that this 41 nm of InN is relaxed and heavily dislocated. Despite this, the rocking-curve FWHM value of only 620 arcseconds and the defined thickness fringes observed in the XRD scan indicate the film quality may not be unusable for device applications. This better-than-expected film quality and surface morphology may be assisted by the polarity and miscut of the GaN-on-sapphire template. In-incorporation is enhanced when growing N-polar InN or InGaN [43]. Also, the short terrace lengths and periodic steps which are present in miscut templates may lead to improved surface morphology such as what is seen in Fig. A-7.a. The author hopes this work will help those who wish to grow pure InN by PAMBE for device applications.

A. 5: Mg doping Using Titan Valved Effusion Cell

The Nitride Gen 2 system at UCSB is equipped with a Titan Valved effusion cell for Mg-doping. A significant amount of time was devoted to calibrating this Mg source. Using this cell, Mg-doping can be controlled via cell temperature and valve position. The cell contains two heaters (base and tip). To avoid a buildup of material on the valve tip, the tip heater should always be 100+ ℃ warmer than the base temperature.

Fig. A-8 below shows a GaN:Mg SIMS stack that was grown at 650 ℃ (measured by pyrometer) using 300 watts plasma power and 0.5 sccm N_2 which resulted in a GaN growth rate of approximately 3.5 nm/min. A Ga-flux of approximately 3.8e-7 torr was used for this growth. All samples in this study were grown on Ga-polar MOCVD grown GaN-on-sapphire templates. These growth conditions were used for virtually all GaN:Mg doping studies. For the growth in Fig. A-8 the cell tip temperature was set to 565 ℃ and the base temperature was floating at 400 ℃. The valve position was varied from 10 mm to 200 mm. Fig. A-9 shows Mg-concentration as a function of valve position extracted from SIMS for different cell temperatures. It should be noted that some of these runs have a cell/base temperature difference that is less than 100 ℃. Mentioned previously, this is not advisable and is no longer practiced. Clearly from figure A-9 Mg-concentration increases linearly as a function of valve position followed by saturation.

To verify actual hole concentration, 600 nm of GaN:Si at a Mg-concentration of 3e19 cm^{-3} was grown on a Ga-polar semi-insulating GaN-on-sapphire template and measured by 4-point Van-Der-Pauw Hall. From Hall, sheet resistance, hole concentration and hole mobility were found to be 15.3 $k\Omega$/sqr., 8.67e17 cm^{-3} and 7.5 $cm^2\ V^{-1}s^{-1}$ respectively.

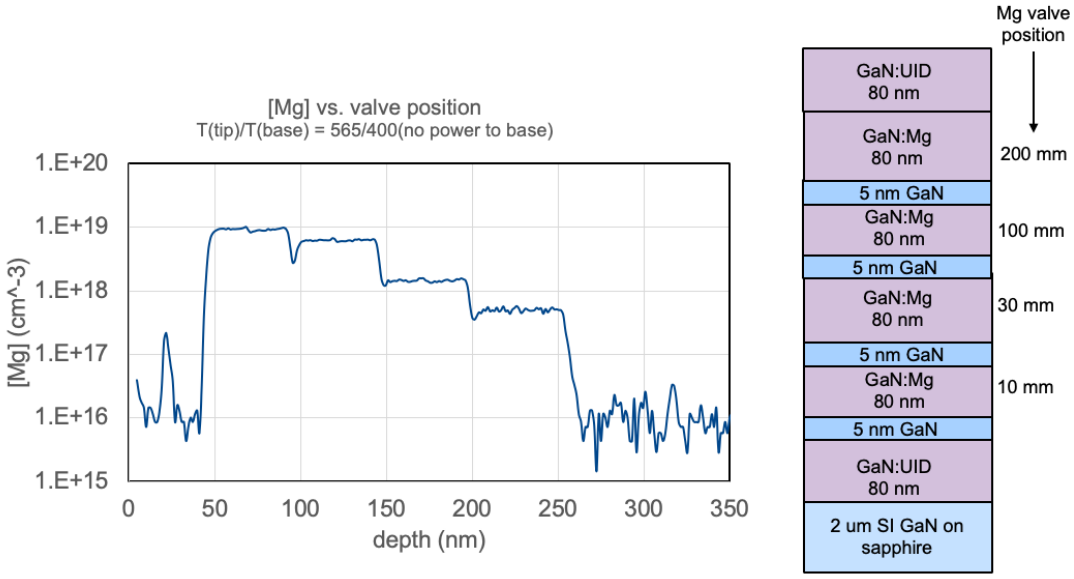

Figure A-8: SIMS profile showing Mg-concentration as a function of depth from the growth which corresponds to the structure on the right-hand side of the plot.

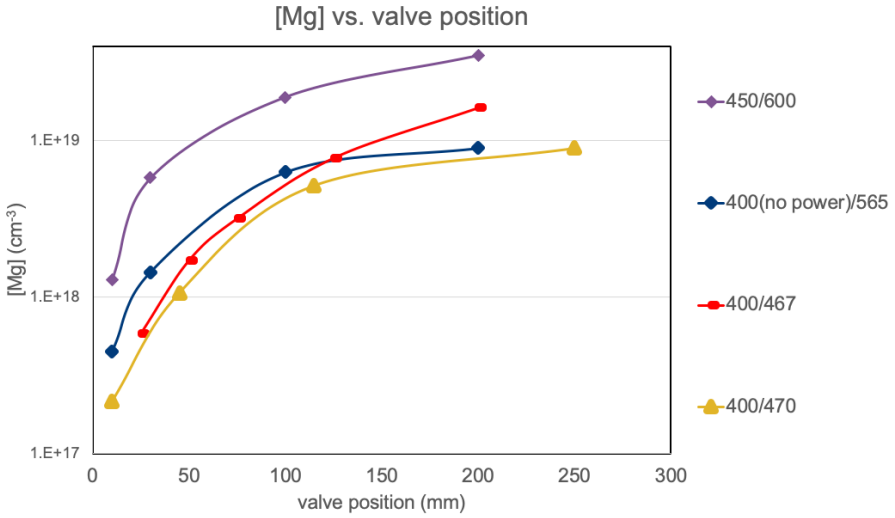

Figure A-9: Mg-concentration as a function of cell valve position for four growths performed at different base/tip temperatures using the growth conditions stated above. Base/tip temperatures are shown on the legend to the right of the plot.

As can be seen from Fig. A-9, the highest doping levels achieved were approximately 3e19 cm^{-3}. Instead of going to higher cell temperatures which ran the risk of the Mg charge in the cell melting and falling out of the cell (this Mg cell is downward facing), an alternative method to achieve high Mg-doping was pursued. Metal-modulated-epitaxy (MME),

mentioned in chapter 4, can be used to achieve ultra-high Mg-doping by growing in a pseudo-N-rich growth regime which enhances Mg-incorporation [201]. In the following study, using the same growth conditions stated above except for N_2 flow being set to 1 sccm instead of 0.5 sccm, approximately 90 nm of GaN:Mg was grown on a GaN-on-sapphire template using MME. The Mg cell temp base/tip temperatures were set to 450/600 ℃ and the cell valve was set to 200 mm giving a Mg-flux of approximately 4.2e-8 torr. For this growth the N-shutter was kept open throughout the whole growth, however the Ga shutter was kept open only for the first 1 minute of growth, closed for 30 seconds to desorb excess Ga, followed by opening the Mg shutter for 5 seconds. Then the Mg-shutter was closed, the Ga-shutter opened and the cycle repeated. 15 cycles were performed at an average growth rate of 5.7 nm/cycle. This shutter cycle is shown in Fig. A-10.c. The SIMS results, RHEED intensity profile and shutter cycle are shown in Fig. A-10.a-c respectively.

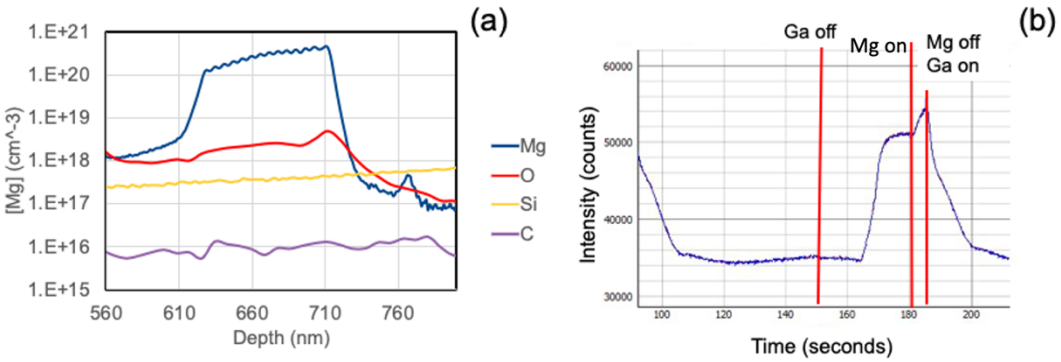

Shutter			
N	Open	Open	Open
Ga	Open	Closed	closed
Mg	Closed	Closed	Open
time →	1:00	0:30	0:05

(c)

Figure A-10: (a) SIMS profile of an MME layer showing Mg, Si, O, and C concentrations, (b) RHEED profile showing one MME cycle and (c) cell shutter table for one MME cycle

The RHEED intensity profile shown in Fig. A-10.b shows a drop in intensity during the GaN growth (as would be expected from the Ga-adlayer). After the Ga shutter is closed at 1 minute the intensity stays low for approximately 15 seconds and then rapidly spikes up to saturation indicating desorption of Ga. A higher spike is seen when the Mg shutter is opened for 5 seconds and drops when the Mg shutter is closed and the Ga shutter is opened. It is believed that the RHEED intensity spike during the time when Mg shutter is opened is due to heat coming from the Mg cell however this is not for certain and subject to further investigation. The MME Mg-doped layer shown in the SIMS profile in Fig. A-10.a shows the Mg concentration jumps up to approximately 3e20 cm^{-3} and then falls to approximately 1.5e20 cm^{-3} after about 90 nm of growth. The cause of this drop in concentration is unknown, however since this high of doping would only be utilized for thin contact layers (<50nm) it is not a major concern. A major concern however is the high O concentration in the MME layer. At the lower growth temperature used for GaN:Mg growth (~650 °C) there will always be slightly higher O-concentration, however this is usually <1e18 cm^{-3}. It is believed that the high O-concentration in the MME layer comes from the time that the Ga-adlayer evaporated and the surface is exposed. This may be remedied by adjusting the time at which the Mg-shutter is opened to coincide at the precise time at which the Ga-adlayer is completely desorbed. This however would require significant optimization or building a program to detect the peak in intensity when the Ga-adlayer is desorbed. This problem will be left for future growers to solve.

References

[1] "Gallium Nitride Semiconductor Devices Market Size, Share & Trends Analysis Report By Product, By Component, By Wafer Size, By End Use, By Region, And Segment Forecasts, 2022 - 2030." Grand View Research, 2022. [Online]. Available: https://www.grandviewresearch.com/industry-analysis/gan-gallium-nitride-semiconductor-devices-market

[2] S.-H. Park and S.-L. Chuang, "Spontaneous polarization effects in wurtzite GaN/AlGaN quantum wells and comparison with experiment," *Appl. Phys. Lett.*, vol. 76, no. 15, pp. 1981–1983, Apr. 2000, doi: 10.1063/1.126229.

[3] U. K. Mishra and J. Singh, *Semiconductor device physics and design*. Dordrecht: Springer, 2008.

[4] O. Ambacher, "Growth and applications of Group III-nitrides," *J. Phys. Appl. Phys.*, vol. 31, no. 20, pp. 2653–2710, Oct. 1998, doi: 10.1088/0022-3727/31/20/001.

[5] F. Bernardini and V. Fiorentini, "Nonlinear macroscopic polarization in III-V nitride alloys," *Phys. Rev. B*, vol. 64, no. 8, p. 085207, Aug. 2001, doi: 10.1103/PhysRevB.64.085207.

[6] M. Asif Khan, A. Bhattarai, J. N. Kuznia, and D. T. Olson, "High electron mobility transistor based on a GaN-Al $_x$ Ga $_{1-x}$ N heterojunction," *Appl. Phys. Lett.*, vol. 63, no. 9, pp. 1214–1215, Aug. 1993, doi: 10.1063/1.109775.

[7] B. Romanczyk *et al.*, "Demonstration of Constant 8 W/mm Power Density at 10, 30, and 94 GHz in State-of-the-Art Millimeter-Wave N-Polar GaN MISHEMTs," *IEEE Trans. Electron Devices*, vol. 65, no. 1, pp. 45–50, Jan. 2018, doi: 10.1109/TED.2017.2770087.

[8] C. Wurm, "Growth of high-quality N-polar (000-1) GaN on bulk GaN by plasma-assisted molecular beam epitaxy for high electron mobility transistors," UCSB, 2019.

[9] C. Skierbiszewski *et al.*, "Role of dislocation-free GaN substrates in the growth of indium containing optoelectronic structures by plasma-assisted MBE," *J. Cryst. Growth*, vol. 305, no. 2, pp. 346–354, Jul. 2007, doi: 10.1016/j.jcrysgro.2007.04.002.

[10] E. C. H. Kyle, S. W. Kaun, P. G. Burke, F. Wu, Y.-R. Wu, and J. S. Speck, "High-electron-mobility GaN grown on free-standing GaN templates by ammonia-based molecular beam epitaxy," *J. Appl. Phys.*, vol. 115, no. 19, p. 193702, May 2014, doi: 10.1063/1.4874735.

[11] N. Grandjean, M. Leroux, J. Massies, M. Mesrine, and M. Laügt, "Molecular Beam Epitaxy of GaN under N-rich Conditions using NH $_3$," *Jpn. J. Appl. Phys.*, vol. 38, no. Part 1, No. 2A, pp. 618–621, Feb. 1999, doi: 10.1143/JJAP.38.618.

[12] E. J. Tarsa, B. Heying, X. H. Wu, P. Fini, S. P. DenBaars, and J. S. Speck, “Homoepitaxial growth of GaN under Ga-stable and N-stable conditions by plasma-assisted molecular beam epitaxy,” *J. Appl. Phys.*, vol. 82, no. 11, pp. 5472–5479, Dec. 1997, doi: 10.1063/1.365575.

[13] S. W. Kaun, M. H. Wong, U. K. Mishra, and J. S. Speck, “Molecular beam epitaxy for high-performance Ga-face GaN electron devices,” *Semicond. Sci. Technol.*, vol. 28, no. 7, p. 074001, Jul. 2013, doi: 10.1088/0268-1242/28/7/074001.

[14] T. Zywietz, J. Neugebauer, and M. Scheffler, “Adatom diffusion at GaN (0001) and (000$\bar{1}$) surfaces,” *Appl. Phys. Lett.*, vol. 73, no. 4, pp. 487–489, Jul. 1998, doi: 10.1063/1.121909.

[15] B. Heying, R. Averbeck, L. F. Chen, E. Haus, H. Riechert, and J. S. Speck, “Control of GaN surface morphologies using plasma-assisted molecular beam epitaxy,” *J. Appl. Phys.*, vol. 88, no. 4, pp. 1855–1860, Aug. 2000, doi: 10.1063/1.1305830.

[16] N. Takeuchi, A. Selloni, T. H. Myers, and A. Doolittle, “Adsorption and diffusion of Ga and N adatoms on GaN surfaces: Comparing the effects of Ga coverage and electronic excitation,” *Phys. Rev. B*, vol. 72, no. 11, Sep. 2005, doi: 10.1103/PhysRevB.72.115307.

[17] J. Neugebauer, T. K. Zywietz, M. Scheffler, J. E. Northrup, H. Chen, and R. M. Feenstra, “Adatom Kinetics On and Below the Surface: The Existence of a New Diffusion Channel,” *Phys. Rev. Lett.*, vol. 90, no. 5, Feb. 2003, doi: 10.1103/PhysRevLett.90.056101.

[18] E. Monroy *et al.*, “Growth kinetics of N-face polarity GaN by plasma-assisted molecular-beam epitaxy,” *Appl. Phys. Lett.*, vol. 84, no. 18, pp. 3684–3686, May 2004, doi: 10.1063/1.1739511.

[19] G. Koblmüller, J. Brown, R. Averbeck, H. Riechert, P. Pongratz, and J. S. Speck, “Ga Adlayer Governed Surface Defect Evolution of (0001)GaN Films Grown by Plasma-Assisted Molecular Beam Epitaxy,” *Jpn. J. Appl. Phys.*, vol. 44, no. No. 28, pp. L906–L908, Jul. 2005, doi: 10.1143/JJAP.44.L906.

[20] F. A. Ponce, D. P. Bour, W. Götz, and P. J. Wright, “Spatial distribution of the luminescence in GaN thin films,” *Appl. Phys. Lett.*, vol. 68, no. 1, pp. 57–59, Jan. 1996, doi: 10.1063/1.116756.

[21] R. Armitage *et al.*, “Contributions from gallium vacancies and carbon-related defects to the ‘yellow luminescence’ in GaN,” *Appl. Phys. Lett.*, vol. 82, no. 20, pp. 3457–3459, May 2003, doi: 10.1063/1.1578169.

[22] B. Heying, E. J. Tarsa, C. R. Elsass, P. Fini, S. P. DenBaars, and J. S. Speck, “Dislocation mediated surface morphology of GaN,” *J. Appl. Phys.*, vol. 85, no. 9, pp. 6470–6476, May 1999, doi: 10.1063/1.370150.

[23] G. B. Stringfellow, *Organometallic vapor-phase epitaxy: theory and practice*, 2. ed. San Diego, Calif.: Acad. Press, 1999.

[24] F. C. Frank, "Capillary equilibria of dislocated crystals," *Acta Crystallogr.*, vol. 4, no. 6, pp. 497–501, Nov. 1951, doi: 10.1107/S0365110X51001690.

[25] F. C. Frank, *Discuss Faraday Soc*, vol. 5, p. 67, 1949.

[26] W. K. Burton, N. Cabrera, and F. C. Frank, *Philos Trans R Soc Lond.*, vol. 243, p. 299, 1951.

[27] W. K. Burton, N. Cabrera, and F. C. Frank, "The growth of crystals and the equilibrium structure of their surfaces," *Philos. Trans. R. Soc. Lond. Ser. Math. Phys. Sci.*, vol. 243, no. 866, pp. 299–358, Jun. 1951, doi: 10.1098/rsta.1951.0006.

[28] T. L. Song, "Strain relaxation due to V-pit formation in InxGa1−xN⁄GaN epilayers grown on sapphire," *J. Appl. Phys.*, vol. 98, no. 8, p. 084906, Oct. 2005, doi: 10.1063/1.2108148.

[29] J. E. Northrup and J. Neugebauer, "Indium-induced changes in GaN(0001) surface morphology," *Phys. Rev. B*, vol. 60, no. 12, pp. R8473–R8476, Sep. 1999, doi: 10.1103/PhysRevB.60.R8473.

[30] J. E. Northrup, L. T. Romano, and J. Neugebauer, "Surface energetics, pit formation, and chemical ordering in InGaN alloys," *Appl. Phys. Lett.*, vol. 74, no. 16, pp. 2319–2321, Apr. 1999, doi: 10.1063/1.123837.

[31] S. S. Pasayat *et al.*, "Compliant Micron-Sized Patterned InGaN Pseudo-Substrates Utilizing Porous GaN," *Materials*, vol. 13, no. 1, p. 213, Jan. 2020, doi: 10.3390/ma13010213.

[32] X. H. Wu *et al.*, "Structural origin of V-defects and correlation with localized excitonic centers in InGaN/GaN multiple quantum wells," *Appl. Phys. Lett.*, vol. 72, no. 6, pp. 692–694, Feb. 1998, doi: 10.1063/1.120844.

[33] S. Zhang *et al.*, "Efficient emission of InGaN-based light-emitting diodes: toward orange and red," *Photonics Res.*, vol. 8, no. 11, p. 1671, Nov. 2020, doi: 10.1364/PRJ.402555.

[34] B. Heying, R. Averbeck, L. F. Chen, E. Haus, H. Riechert, and J. S. Speck, "Control of GaN surface morphologies using plasma-assisted molecular beam epitaxy," *J. Appl. Phys.*, vol. 88, no. 4, pp. 1855–1860, Aug. 2000, doi: 10.1063/1.1305830.

[35] H. Chen, R. M. Feenstra, J. E. Northrup, T. Zywietz, J. Neugebauer, and D. W. Greve, "Surface structures and growth kinetics of InGaN(0001) grown by molecular beam epitaxy," *J. Vac. Sci. Technol. B Microelectron. Nanometer Struct.*, vol. 18, no. 4, p. 2284, 2000, doi: 10.1116/1.1306296.

[36] K. M. Bui, M. Boero, K. Shiraishi, and A. Oshiyama, “A two-dimensional liquid-like phase on Ga-rich GaN (0001) surfaces evidenced by first principles molecular dynamics,” *Jpn. J. Appl. Phys.*, Dec. 2019, doi: 10.7567/1347-4065/ab650b.

[37] C. Chèze *et al.*, “Step-flow growth mode instability of N-polar GaN under N-excess,” *Appl. Phys. Lett.*, vol. 103, no. 7, p. 071601, Aug. 2013, doi: 10.1063/1.4818322.

[38] S. S. Pasayat *et al.*, “First demonstration of RF N-polar GaN MIS-HEMTs grown on bulk GaN using PAMBE,” *Semicond. Sci. Technol.*, vol. 34, no. 4, p. 045009, Apr. 2019, doi: 10.1088/1361-6641/ab0761.

[39] H. Turski *et al.*, “Unusual step meandering due to Ehrlich-Schwoebel barrier in GaN epitaxy on the N-polar surface,” *Appl. Surf. Sci.*, Apr. 2019, doi: 10.1016/j.apsusc.2019.04.082.

[40] S. Wienecke *et al.*, “N-Polar GaN Cap MISHEMT With Record Power Density Exceeding 6.5 W/mm at 94 GHz,” *IEEE Electron Device Lett.*, vol. 38, no. 3, pp. 359–362, Mar. 2017, doi: 10.1109/LED.2017.2653192.

[41] M. H. Wong *et al.*, “N-polar GaN epitaxy and high electron mobility transistors,” *Semicond. Sci. Technol.*, vol. 28, no. 7, p. 074009, Jul. 2013, doi: 10.1088/0268-1242/28/7/074009.

[42] *Power GaN devices*. New York, NY: Springer Berlin Heidelberg, 2016.

[43] S. Keller *et al.*, “Recent progress in metal-organic chemical vapor deposition of (000-1) N-polar group-III nitrides,” *Semicond. Sci. Technol.*, vol. 29, no. 11, p. 113001, Nov. 2014, doi: 10.1088/0268-1242/29/11/113001.

[44] S. W. Kaun, M. H. Wong, U. K. Mishra, and J. S. Speck, “Correlation between threading dislocation density and sheet resistance of AlGaN/AlN/GaN heterostructures grown by plasma-assisted molecular beam epitaxy,” *Appl. Phys. Lett.*, vol. 100, no. 26, p. 262102, Jun. 2012, doi: 10.1063/1.4730951.

[45] D. C. Look and J. R. Sizelove, “Dislocation Scattering in GaN,” *Phys. Rev. Lett.*, vol. 82, no. 6, pp. 1237–1240, Feb. 1999, doi: 10.1103/PhysRevLett.82.1237.

[46] S. Dayeh, A. Tanaka, W. Choi, and R. Chen, “(Invited) Strain Engineered Crack-Free GaN on Si for Integrated Vertical High Power GaN Devices with Si CMOS,” *ECS Trans.*, vol. 75, no. 8, pp. 711–723, Sep. 2016, doi: 10.1149/07508.0711ecst.

[47] S. Y. Ren and J. D. Dow, “Lattice-matching SiC substrates with GaN,” p. 4.

[48] P. Waltereit *et al.*, “Influence of AlN nucleation layers on growth mode and strain relief of GaN grown on 6H–SiC(0001),” *Appl. Phys. Lett.*, vol. 74, no. 24, pp. 3660–3662, Jun. 1999, doi: 10.1063/1.123214.

[49] B. Heying, E. J. Tarsa, C. R. Elsass, P. Fini, S. P. DenBaars, and J. S. Speck, “Dislocation mediated surface morphology of GaN,” *J. Appl. Phys.*, vol. 85, no. 9, pp. 6470–6476, May 1999, doi: 10.1063/1.370150.

[50] C. Gupta, Y. Enatsu, G. Gupta, S. Keller, and U. K. Mishra, “High breakdown voltage p-n diodes on GaN on sapphire by MOCVD: High breakdown voltage p-n diodes,” *Phys. Status Solidi A*, vol. 213, no. 4, pp. 878–882, Apr. 2016, doi: 10.1002/pssa.201532554.

[51] N. G. Weimann, L. F. Eastman, D. Doppalapudi, H. M. Ng, and T. D. Moustakas, “Scattering of electrons at threading dislocations in GaN,” *J. Appl. Phys.*, vol. 83, no. 7, pp. 3656–3659, Apr. 1998, doi: 10.1063/1.366585.

[52] B. S. Simpkins, E. T. Yu, P. Waltereit, and J. S. Speck, “Correlated scanning Kelvin probe and conductive atomic force microscopy studies of dislocations in gallium nitride,” *J. Appl. Phys.*, vol. 94, no. 3, pp. 1448–1453, Aug. 2003, doi: 10.1063/1.1586952.

[53] D. G. Zhao *et al.*, “Effects of edge dislocations and intentional Si doping on the electron mobility of n-type GaN films,” *Appl. Phys. Lett.*, vol. 89, no. 11, p. 112106, Sep. 2006, doi: 10.1063/1.2348740.

[54] S. W. Kaun, M. H. Wong, U. K. Mishra, and J. S. Speck, “Correlation between threading dislocation density and sheet resistance of AlGaN/AlN/GaN heterostructures grown by plasma-assisted molecular beam epitaxy,” *Appl. Phys. Lett.*, vol. 100, no. 26, p. 262102, Jun. 2012, doi: 10.1063/1.4730951.

[55] D. F. Storm *et al.*, “Microwave performance and structural characterization of MBE-grown AlGaN/GaN HEMTs on low dislocation density GaN substrates,” *J. Cryst. Growth*, vol. 305, no. 2, pp. 340–345, Jul. 2007, doi: 10.1016/j.jcrysgro.2007.04.003.

[56] T. K. Zywietz, J. Neugebauer, and M. Scheffler, “The adsorption of oxygen at GaN surfaces,” *Appl. Phys. Lett.*, vol. 74, no. 12, pp. 1695–1697, Mar. 1999, doi: 10.1063/1.123658.

[57] Z. P. Guan, A. L. Cai, J. S. Cabalu, H. L. Porter, and S. Huang, “Molecular beam epitaxy growth of GaN on C-terminated 6H–SiC (0001¯) surface,” *Appl. Phys. Lett.*, vol. 77, no. 16, pp. 2491–2493, Oct. 2000, doi: 10.1063/1.1318723.

[58] E. Ahmadi *et al.*, “N-face GaN/AlN/GaN/InAlN and GaN/AlN/AlGaN/GaN/InAlN high-electron-mobility transistor structures grown by plasma-assisted molecular beam epitaxy on vicinal substrates,” *Semicond. Sci. Technol.*, vol. 30, no. 5, p. 055012, May 2015, doi: 10.1088/0268-1242/30/5/055012.

[59] C. Wurm *et al.*, "Growth of high-quality N-polar GaN on bulk GaN by plasma-assisted molecular beam epitaxy," *Solid State Commun.*, vol. 305, p. 113763, Jan. 2020, doi: 10.1016/j.ssc.2019.113763.

[60] D. S. Green, U. K. Mishra, and J. S. Speck, "Carbon doping of GaN with CBr4 in radio-frequency plasma-assisted molecular beam epitaxy," *J. Appl. Phys.*, vol. 95, no. 12, pp. 8456–8462, Jun. 2004, doi: 10.1063/1.1755431.

[61] M. A. Moram and M. E. Vickers, "X-ray diffraction of III-nitrides," *Rep. Prog. Phys.*, vol. 72, no. 3, p. 036502, Mar. 2009, doi: 10.1088/0034-4885/72/3/036502.

[62] C. Gupta *et al.*, "In Situ Oxide, GaN Interlayer-Based Vertical Trench MOSFET (OG-FET) on Bulk GaN substrates," *IEEE Electron Device Lett.*, vol. 38, no. 3, pp. 353–355, Mar. 2017, doi: 10.1109/LED.2017.2649599.

[63] J. Ibbetson, "Electrical Characterization of Nonstoichiometric GaAs Grown at Low Temperature by Molecular Beam Epitaxy," UCSB, 1997.

[64] S. W. Kaun, M. H. Wong, U. K. Mishra, and J. S. Speck, "Molecular beam epitaxy for high-performance Ga-face GaN electron devices," *Semicond. Sci. Technol.*, vol. 28, no. 7, p. 074001, Jul. 2013, doi: 10.1088/0268-1242/28/7/074001.

[65] S. Rajan, M. Wong, Y. Fu, F. Wu, J. S. Speck, and U. K. Mishra, "Growth and Electrical Characterization of N-face AlGaN/GaN Heterostructures," *Jpn. J. Appl. Phys.*, vol. 44, no. No. 49, pp. L1478–L1480, Nov. 2005, doi: 10.1143/JJAP.44.L1478.

[66] L. Ravikiran, M. Agrawal, N. Dharmarasu, and K. Radhakrishnan, "Effect of Stress Mitigating Layers on the Structural Properties of GaN Grown by Ammonia Molecular Beam Epitaxy on 100 mm Si(111)," *Jpn. J. Appl. Phys.*, vol. 52, no. 8S, p. 08JE05, Aug. 2013, doi: 10.7567/JJAP.52.08JE05.

[67] M. Agrawal, K. Radhakrishnan, N. Dharmarasu, and S. S. Pramana, "Effect of III/V ratio on the polarity of AlN and GaN layers grown in the metal rich growth regime on Si(111) by plasma assisted molecular beam epitaxy," *Jpn. J. Appl. Phys.*, vol. 54, no. 6, p. 065701, Jun. 2015, doi: 10.7567/JJAP.54.065701.

[68] M. Stutzmann *et al.*, "Playing with Polarity," *Phys. Status Solidi B*, vol. 228, no. 2, pp. 505–512, Nov. 2001, doi: 10.1002/1521-3951(200111)228:2<505::AID-PSSB505>3.0.CO;2-U.

[69] P. Sohi, D. Martin, and N. Grandjean, "Critical thickness of GaN on AlN: impact of growth temperature and dislocation density," *Semicond. Sci. Technol.*, vol. 32, no. 7, p. 075010, Jul. 2017, doi: 10.1088/1361-6641/aa7248.

[70] A. Adikimenakis *et al.*, “Effect of AlN interlayers in the structure of GaN-on-Si grown by plasma-assisted MBE,” *J. Cryst. Growth*, vol. 311, no. 7, pp. 2010–2015, Mar. 2009, doi: 10.1016/j.jcrysgro.2008.10.085.

[71] I. P. Smorchkova *et al.*, “Two-dimensional electron-gas AlNÕGaN heterostructures with extremely thin AlN barriers,” p. 3.

[72] H. Li, “New aspect in MOCVD of metal- and N-polar (Al,Ga)N and its device applications,” UCSB, 2018.

[73] C. Poblenz, P. Waltereit, S. Rajan, S. Heikman, U. K. Mishra, and J. S. Speck, “Effect of carbon doping on buffer leakage in AlGaN/GaN high electron mobility transistors,” *J. Vac. Sci. Technol. B Microelectron. Nanometer Struct.*, vol. 22, no. 3, p. 1145, 2004, doi: 10.1116/1.1752907.

[74] J. L. Lyons, A. Janotti, and C. G. Van de Walle, “Carbon impurities and the yellow luminescence in GaN,” *Appl. Phys. Lett.*, vol. 97, no. 15, p. 152108, Oct. 2010, doi: 10.1063/1.3492841.

[75] S. Diez, S. Mohanty, C. Kurdak, and E. Ahmadi, “Record high electron mobility and low sheet resistance on scaled-channel N-polar GaN/AlN heterostructures grown on on-axis N-polar GaN substrates by plasma-assisted molecular beam epitaxy,” *Appl. Phys. Lett.*, vol. 117, no. 4, p. 042102, Jul. 2020, doi: 10.1063/5.0014460.

[76] S. Nakamura *et al.*, “InGaN Multi-Quantum-Well-Structure Laser Diodes with Cleaved Mirror Cavity Facets,” *Jpn. J. Appl. Phys.*, vol. 35, no. Part 2, No. 2B, pp. L217–L220, Feb. 1996, doi: 10.1143/JJAP.35.L217.

[77] S. Nakamura, M. Senoh, N. Iwasa, S. Nagahama, T. Yamada, and T. Mukai, “Superbright Green InGaN Single-Quantum-Well-Structure Light-Emitting Diodes,” *Jpn. J. Appl. Phys.*, vol. 34, no. Part 2, No. 10B, pp. L1332–L1335, Oct. 1995, doi: 10.1143/JJAP.34.L1332.

[78] F. Hide, P. Kozodoy, S. P. DenBaars, and A. J. Heeger, “White light from InGaN/conjugated polymer hybrid light-emitting diodes,” *Appl. Phys. Lett.*, vol. 70, no. 20, pp. 2664–2666, May 1997, doi: 10.1063/1.118989.

[79] J. K. Sheu *et al.*, “White-light emission from InGaN-GaN multiquantum-well light-emitting diodes with Si and Zn codoped active well layer,” *IEEE Photonics Technol. Lett.*, vol. 14, no. 4, pp. 450–452, Apr. 2002, doi: 10.1109/68.992574.

[80] J. K. Sheu *et al.*, “White-light emission from near UV InGaN-GaN LED chip precoated with blue/green/red phosphors,” *IEEE Photonics Technol. Lett.*, vol. 15, no. 1, pp. 18–20, Jan. 2003, doi: 10.1109/LPT.2002.805852.

[81] I. Ho and G. B. Stringfellow, “Solid phase immiscibility in GaInN,” *Appl. Phys. Lett.*, vol. 69, no. 18, pp. 2701–2703, Oct. 1996, doi: 10.1063/1.117683.

[82] S. Valdueza-Felip *et al.*, “High In-content InGaN layers synthesized by plasma-assisted molecular-beam epitaxy: Growth conditions, strain relaxation, and In incorporation kinetics,” *J. Appl. Phys.*, vol. 116, no. 23, p. 233504, Dec. 2014, doi: 10.1063/1.4903944.

[83] G. B. Stringfellow, “Microstructures produced during the epitaxial growth of InGaN alloys,” *J. Cryst. Growth*, vol. 312, no. 6, pp. 735–749, Mar. 2010, doi: 10.1016/j.jcrysgro.2009.12.018.

[84] M. Siekacz *et al.*, “Growth of InGaN and InGaN/InGaN quantum wells by plasma-assisted molecular beam epitaxy,” *J. Cryst. Growth*, vol. 310, no. 17, pp. 3983–3986, Aug. 2008, doi: 10.1016/j.jcrysgro.2008.06.011.

[85] H. Turski *et al.*, “Growth mechanism of InGaN by plasma assisted molecular beam epitaxy,” *J. Vac. Sci. Technol. B Nanotechnol. Microelectron. Mater. Process. Meas. Phenom.*, vol. 29, no. 3, p. 03C136, May 2011, doi: 10.1116/1.3590932.

[86] M. Moseley, B. Gunning, J. Greenlee, J. Lowder, G. Namkoong, and W. Alan Doolittle, “Observation and control of the surface kinetics of InGaN for the elimination of phase separation,” *J. Appl. Phys.*, vol. 112, no. 1, p. 014909, Jul. 2012, doi: 10.1063/1.4733347.

[87] G. T. Thaler, D. D. Koleske, S. R. Lee, K. H. A. Bogart, and M. H. Crawford, “Thermal stability of thin InGaN films on GaN,” *J. Cryst. Growth*, vol. 312, no. 11, pp. 1817–1822, May 2010, doi: 10.1016/j.jcrysgro.2010.03.008.

[88] O. Ambacher, “Thermal stability and desorption of Group III nitrides prepared by metal organic chemical vapor deposition,” *J. Vac. Sci. Technol. B Microelectron. Nanometer Struct.*, vol. 14, no. 6, p. 3532, Nov. 1996, doi: 10.1116/1.588793.

[89] T. Böttcher *et al.*, “Incorporation of indium during molecular beam epitaxy of InGaN,” *Appl. Phys. Lett.*, vol. 73, no. 22, pp. 3232–3234, Nov. 1998, doi: 10.1063/1.122728.

[90] R. A. Oliver, M. J. Kappers, C. J. Humphreys, and G. A. D. Briggs, “Growth modes in heteroepitaxy of InGaN on GaN,” *J. Appl. Phys.*, vol. 97, no. 1, p. 013707, Jan. 2005, doi: 10.1063/1.1823581.

[91] S. Keller, S. F. Chichibu, M. S. Minsky, E. Hu, U. K. Mishra, and S. P. DenBaars, “Effect of the growth rate and the barrier doping on the morphology and the properties of InGaN/GaN quantum wells,” *J. Cryst. Growth*, vol. 195, no. 1–4, pp. 258–264, Dec. 1998, doi: 10.1016/S0022-0248(98)00680-0.

[92] W. Seifert, R. Franzheld, E. Butter, H. Sobotta, and V. Riede, “On the origin of free carriers in high-conducting n-GaN,” *Cryst. Res. Technol.*, vol. 18, no. 3, pp. 383–390, 1983, doi: 10.1002/crat.2170180314.

[93] K. Binder, “Theory of first-order phase transitions,” *Rep. Prog. Phys.*, vol. 50, no. 7, pp. 783–859, Jul. 1987, doi: 10.1088/0034-4885/50/7/001.

[94] S. Yu. Karpov, “Suppression of phase separation in InGaN due to elastic strain,” *MRS Internet J. Nitride Semicond. Res.*, vol. 3, p. e16, 1998, doi: 10.1557/S1092578300000880.

[95] C. Tessarek *et al.*, “Strong phase separation of strained In x Ga 1 − x N layers due to spinodal and binodal decomposition: Formation of stable quantum dots,” *Phys. Rev. B*, vol. 83, no. 11, p. 115316, Mar. 2011, doi: 10.1103/PhysRevB.83.115316.

[96] J. Neugebauer, “Surfactants and antisurfactants on group-III-nitride surfaces,” *Phys. Status Solidi C*, no. 6, pp. 1651–1667, Sep. 2003, doi: 10.1002/pssc.200303132.

[97] O. Brandt, P. Waltereit, U. Jahn, S. Dhar, and K. H. Ploog, “Impact of In Bulk and Surface Segregation on the Optical Properties of (In,Ga)N/GaN Multiple Quantum Wells,” *Phys. Status Solidi A*, vol. 192, no. 1, pp. 5–13, Jul. 2002, doi: 10.1002/1521-396X(200207)192:1<5::AID-PSSA5>3.0.CO;2-B.

[98] S. Yu. Karpov and Yu. N. Makarov, “Surface Segregation in Group-III Nitride MBE,” *Phys. Status Solidi A*, vol. 188, no. 2, pp. 611–614, Dec. 2001, doi: 10.1002/1521-396X(200112)188:2<611::AID-PSSA611>3.0.CO;2-Z.

[99] S. Choi *et al.*, “Indium adlayer kinetics on the gallium nitride (0001) surface: Monitoring indium segregation and precursor-mediated adsorption,” *Phys. Rev. B*, vol. 77, no. 11, p. 115435, Mar. 2008, doi: 10.1103/PhysRevB.77.115435.

[100] N. Grandjean and M. Ilegems, “Visible InGaN/GaN Quantum-Dot Materials and Devices,” *Proc. IEEE*, vol. 95, no. 9, pp. 1853–1865, Sep. 2007, doi: 10.1109/JPROC.2007.900970.

[101] A. Bansal, J. M. Redwing, and Z. Y. Al Balushi, “Cathodoluminescence spatially resolves optical transitions in thick group-III and N-polar InGaN films,” *J. Appl. Phys.*, vol. 128, no. 17, p. 175305, Nov. 2020, doi: 10.1063/5.0025361.

[102] E. A. Clinton *et al.*, “A review of the synthesis of reduced defect density InxGa1−xN for all indium compositions,” *Solid-State Electron.*, vol. 136, pp. 3–11, Oct. 2017, doi: 10.1016/j.sse.2017.06.020.

[103] K. Khan, M. Biswas, and E. Ahmadi, “Growth of high quality (In,Ga)N films on O-face ZnO substrates by plasma-assisted molecular beam epitaxy,” *AIP Adv.*, vol. 10, no. 7, p. 075120, Jul. 2020, doi: 10.1063/5.0012854.

[104] L. Zhou, D. J. Smith, M. R. McCartney, D. S. Katzer, and D. F. Storm, “Observation of vertical honeycomb structure in InAlN⁄GaN heterostructures due to lateral phase separation,” *Appl. Phys. Lett.*, vol. 90, no. 8, p. 081917, Feb. 2007, doi: 10.1063/1.2696206.

[105] E. Ahmadi, “Growth Optimization of III-N Electronic Devices by Plasma-Assisted Molecular Beam Epitaxy,” p. 146.

[106] S. M. Hu, “Stress-related problems in silicon technology,” *J Appl Phys*, vol. 70, no. 6, p. 29, 1991.

[107] A. Fischer and H. Richter, “Elastic misfit stress relaxation in heteroepitaxial SiGe/Si mesa structures,” *Appl. Phys. Lett.*, vol. 61, no. 22, pp. 2656–2658, Nov. 1992, doi: 10.1063/1.108099.

[108] A. Fischer, H. Kuhne, B. Roos, and H. Richter, “Elastic strain relaxation in patterned heteroepitaxial structures,” *Semicond. Sci. Technol.*, vol. 9, no. 12, pp. 2195–2198, Dec. 1994, doi: 10.1088/0268-1242/9/12/005.

[109] P. Chavarkar, “Lattice Engineered Substrates Using Lateral Oxidation of AlAs,” Thesis, UCSB, 2000.

[110] J. Matthews, “Defects in epitaxial multilayers I. Misfit dislocations,” *J. Cryst. Growth*, vol. 27, pp. 118–125, Dec. 1974, doi: 10.1016/0022-0248(74)90424-2.

[111] R. People and J. C. Bean, “Calculation of critical layer thickness versus lattice mismatch for Ge_xSi_{1-x}/Si strained-layer heterostructures,” *Appl. Phys. Lett.*, vol. 47, no. 3, pp. 322–324, Aug. 1985, doi: 10.1063/1.96206.

[112] J. C. Bean, L. C. Feldman, A. T. Fiory, S. Nakahara, and I. K. Robinson, “Ge_xSi_{1-x}/Si strained-layer superlattice grown by molecular beam epitaxy,” *J. Vac. Sci. Technol. Vac. Surf. Films*, vol. 2, no. 2, pp. 436–440, Apr. 1984, doi: 10.1116/1.572361.

[113] A. Fischer, H. Kühne, and H. Richter, “New Approach in Equilibrium Theory for Strained Layer Relaxation,” *Phys. Rev. Lett.*, vol. 73, no. 20, pp. 2712–2715, Nov. 1994, doi: 10.1103/PhysRevLett.73.2712.

[114] D. Holec, P. M. F. J. Costa, M. J. Kappers, and C. J. Humphreys, “Critical thickness calculations for InGaN/GaN,” *J. Cryst. Growth*, vol. 303, no. 1, pp. 314–317, May 2007, doi: 10.1016/j.jcrysgro.2006.12.054.

[115] R. Liu *et al.*, “Misfit Dislocation Generation in InGaN Epilayers on Free-Standing GaN,” *Jpn. J. Appl. Phys.*, vol. 45, no. No. 22, pp. L549–L551, Jun. 2006, doi: 10.1143/JJAP.45.L549.

[116] L. B. Freund and S. Suresh, *Stress, Defect Formation, and Surface Evolution*. Cambridge University Press, 2003.

[117] S. Srinivasan, L. Geng, R. Liu, F. A. Ponce, Y. Narukawa, and S. Tanaka, "Slip systems and misfit dislocations in InGaN epilayers," *Appl. Phys. Lett.*, vol. 83, no. 25, pp. 5187–5189, Dec. 2003, doi: 10.1063/1.1633029.

[118] P. R. Berger, K. Chang, P. Bhattacharya, J. Singh, and K. K. Bajaj, "Role of strain and growth conditions on the growth front profile of $In_x Ga_{1-x} As$ on GaAs during the pseudomorphic growth regime," *Appl. Phys. Lett.*, vol. 53, no. 8, pp. 684–686, Aug. 1988, doi: 10.1063/1.99850.

[119] M. Shiojiri, C. C. Chuo, J. T. Hsu, J. R. Yang, and H. Saijo, "Structure and formation mechanism of V defects in multiple InGaN⁄GaN quantum well layers," *J. Appl. Phys.*, vol. 99, no. 7, p. 073505, Apr. 2006, doi: 10.1063/1.2180532.

[120] C. Bazioti *et al.*, "Defects, strain relaxation, and compositional grading in high indium content InGaN epilayers grown by molecular beam epitaxy," *J. Appl. Phys.*, vol. 118, no. 15, p. 155301, Oct. 2015, doi: 10.1063/1.4933276.

[121] H. Wang *et al.*, "Investigation on the strain relaxation of InGaN layer and its effects on the InGaN structural and optical properties," *Phys. B Condens. Matter*, vol. 405, no. 22, pp. 4668–4672, Nov. 2010, doi: 10.1016/j.physb.2010.08.058.

[122] S. Mahanty *et al.*, "V-shaped defects in InGaNrGaN multiquantum wells," p. 5, 1999.

[123] K. Hestroffer, C. Lund, H. Li, S. Keller, J. S. Speck, and U. K. Mishra, "Plasma-assisted molecular beam epitaxy growth diagram of InGaN on (0001) GaN for the optimized synthesis of InGaN compositional grades: PAMBE growth diagram for optimized synthesis of InGaN compositional grades," *Phys. Status Solidi B*, vol. 253, no. 4, pp. 626–629, Apr. 2016, doi: 10.1002/pssb.201552550.

[124] K. Hestroffer *et al.*, "Relaxed *c* -plane InGaN layers for the growth of strain-reduced InGaN quantum wells," *Semicond. Sci. Technol.*, vol. 30, no. 10, p. 105015, Oct. 2015, doi: 10.1088/0268-1242/30/10/105015.

[125] Q. T. Li, A. Minj, M. P. Chauvat, J. Chen, and P. Ruterana, "Interface dislocations in $In_x Ga_{1-x}$ N/GaN heterostructures: Interface dislocations in $In_x Ga_{1-x}$ N/GaN," *Phys. Status Solidi A*, vol. 214, no. 4, p. 1600442, Apr. 2017, doi: 10.1002/pssa.201600442.

[126] Z. Lv, H. Wang, and H. Jiang, "Surface Evolution of Thick InGaN Epilayers with Growth Interruption Time," *J. Phys. Chem. C*, vol. 125, no. 30, pp. 16643–16651, Aug. 2021, doi: 10.1021/acs.jpcc.0c11414.

[127] C. Poblenz, “Growth of (In,Al)GaN alloys by RF-plasma assisted molecular beam epitaxy for application in high electron mobility transistor structures,” UCSB, 2005.

[128] C. Adelmann, R. Langer, G. Feuillet, and B. Daudin, “Indium incorporation during the growth of InGaN by molecular-beam epitaxy studied by reflection high-energy electron diffraction intensity oscillations,” *Appl. Phys. Lett.*, vol. 75, no. 22, pp. 3518–3520, Nov. 1999, doi: 10.1063/1.125374.

[129] S. Kaun, “Growth optimization of metal-polar III-nitride high-electron-mobility transistor structures by molecular beam epitaxy,” UCSB, 2014.

[130] S.-N. Lee *et al.*, “Characterization of optical and crystal qualities in InxGa1–xN/InyGa1–yN multi-quantum wells grown by MOCVD,” *J. Cryst. Growth*, vol. 250, no. 1–2, pp. 256–261, Mar. 2003, doi: 10.1016/S0022-0248(02)02247-9.

[131] A. K. Tan, N. A. Hamzah, M. A. Ahmad, S. S. Ng, and Z. Hassan, “Recent advances and challenges in the MOCVD growth of indium gallium nitride: A brief review,” *Mater. Sci. Semicond. Process.*, vol. 143, p. 106545, Jun. 2022, doi: 10.1016/j.mssp.2022.106545.

[132] C. W. Snyder, B. G. Orr, D. Kessler, and L. M. Sander, “Effect of strain on surface morphology in highly strained InGaAs films,” *Phys. Rev. Lett.*, vol. 66, no. 23, pp. 3032–3035, Jun. 1991, doi: 10.1103/PhysRevLett.66.3032.

[133] H. Gao and W. D. Nix, “SURFACE ROUGHENING OF HETEROEPITAXIAL THIN FILMS,” p. 38, 1999.

[134] K. A. Bulashevich and S. Yu. Karpov, “Impact of surface recombination on efficiency of III-nitride light-emitting diodes,” *Phys. Status Solidi RRL - Rapid Res. Lett.*, vol. 10, no. 6, pp. 480–484, Jun. 2016, doi: 10.1002/pssr.201600059.

[135] P. Royo, R. P. Stanley, M. Ilegems, K. Streubel, and K. H. Gulden, “Experimental determination of the internal quantum efficiency of AlGaInP microcavity light-emitting diodes,” *J. Appl. Phys.*, vol. 91, no. 5, pp. 2563–2568, Mar. 2002, doi: 10.1063/1.1433938.

[136] M. Boroditsky *et al.*, “Surface recombination measurements on III–V candidate materials for nanostructure light-emitting diodes,” *J. Appl. Phys.*, vol. 87, no. 7, pp. 3497–3504, Apr. 2000, doi: 10.1063/1.372372.

[137] P. Dalapati, N. B. Manik, and A. N. Basu, “Influence of temperature on the performance of high power AlGaInP based red light emitting diode,” *Opt. Quantum Electron.*, vol. 47, no. 5, pp. 1227–1238, May 2015, doi: 10.1007/s11082-014-9980-5.

[138] M. Funato *et al.*, “Blue, Green, and Amber InGaN/GaN Light-Emitting Diodes on Semipolar {11-22} GaN Bulk Substrates,” *Jpn. J. Appl. Phys.*, vol. 45, no. No. 26, pp. L659–L662, Jun. 2006, doi: 10.1143/JJAP.45.L659.

[139] J.-I. Hwang, R. Hashimoto, S. Saito, and S. Nunoue, “Development of InGaN-based red LED grown on (0001) polar surface,” *Appl. Phys. Express*, vol. 7, no. 7, p. 071003, Jul. 2014, doi: 10.7567/APEX.7.071003.

[140] D. Iida, K. Niwa, S. Kamiyama, and K. Ohkawa, “Demonstration of InGaN-based orange LEDs with hybrid multiple-quantum-wells structure,” *Appl. Phys. Express*, vol. 9, no. 11, p. 111003, Nov. 2016, doi: 10.7567/APEX.9.111003.

[141] P. Li *et al.*, “Demonstration of ultra-small 5 × 5 μ m ^{2} 607 nm InGaN amber micro-light-emitting diodes with an external quantum efficiency over 2%,” *Appl. Phys. Lett.*, vol. 120, no. 4, p. 041102, Jan. 2022, doi: 10.1063/5.0078771.

[142] Y. Kawaguchi, M. Shimizu, K. Hiramatsu, and N. Sawaki, “The Composition Pulling Effect in InGaN Growth on the GaN and AlGaN Epitaxial Layers Grown by MOVPE,” *MRS Proc.*, vol. 449, p. 89, 1996, doi: 10.1557/PROC-449-89.

[143] K. Hiramatsu *et al.*, “The Composition Pulling Effect in MOVPE Grown InGaN on GaN and AlGaN and its TEM Characterization,” *MRS Internet J. Nitride Semicond. Res.*, vol. 2, p. e6, 1997, doi: 10.1557/S1092578300001320.

[144] S. Pereira *et al.*, “Compositional pulling effects in In x Ga 1 − x N / G a N layers: A combined depth-resolved cathodoluminescence and Rutherford backscattering/channeling study,” *Phys. Rev. B*, vol. 64, no. 20, p. 205311, Nov. 2001, doi: 10.1103/PhysRevB.64.205311.

[145] J. Seo Im, H. Kollmer, J. Off, A. Sohmer, F. Scholz, and A. Hangleiter, “Reduction of oscillator strength due to piezoelectric fields in GaN/AlxGa1−xN quantum wells,” *Phys. Rev. B*, vol. 57, no. 16, pp. R9435–R9438, Apr. 1998, doi: 10.1103/PhysRevB.57.R9435.

[146] S.-H. Park, T.-H. Chung, J. H. Baek, and D. Ahn, “Reduction of efficiency droop in green strain-compensated InGaN/InGaN light-emitting diodes grown on InGaN substrate,” *Jpn. J. Appl. Phys.*, vol. 54, no. 2, p. 022101, Feb. 2015, doi: 10.7567/JJAP.54.022101.

[147] A. der M. Matthias, A. Pecchia, G. Penazzi, W. Rodrigues, and A. Di Carlo, “Efficiency Drop in Green InGaN=GaN Light Emitting Diodes: The Role of Random Alloy Fluctuations,” *Phys. Rev. Lett.*, vol. 116, p. 027401, 2016, doi: 10.1103/PhysRevLett.116.027401.

[148] D. Schiavon, M. Binder, P. Matthias, B. Galler, P. Drechsel, and F. Scholz, “Wavelength-dependent determination of the recombination rate coefficients in single-quantum-well GaInN/GaN light emitting diodes,” *Phys Status Solidi*, vol. B 250, no. 2, pp. 283–290, 2013, doi: 10.1002/pssb.201248286.

[149] M. R. Islam, Y. Ohmura, A. Hashimoto, A. Yamamoto, K. Kinoshita, and Y. Koji, "'Step-graded interlayers' for the improvement of MOVPE InxGa1-xN (x ∼ 0.4) epi-layer quality," *Phys. Status Solidi C*, vol. 7, no. 7–8, pp. 2097–2100, Jun. 2010, doi: 10.1002/pssc.200983586.

[150] J. Däubler *et al.*, "Long wavelength emitting GaInN quantum wells on metamorphic GaInN buffer layers with enlarged in-plane lattice parameter," *Appl. Phys. Lett.*, vol. 105, no. 11, p. 111111, Sep. 2014, doi: 10.1063/1.4895067.

[151] K. Hestroffer *et al.*, "Compositionally graded InGaN layers grown on vicinal N-face GaN substrates by plasma-assisted molecular beam epitaxy," *J. Cryst. Growth*, vol. 465, pp. 55–59, May 2017, doi: 10.1016/j.jcrysgro.2017.02.037.

[152] Y. Liu *et al.*, "High-indium-content InGaN quantum-well structure grown pseudomorphically on a strain-relaxed InGaN template layer," *J. Vac. Sci. Technol. B Nanotechnol. Microelectron. Mater. Process. Meas. Phenom.*, vol. 30, no. 3, p. 030603, May 2012, doi: 10.1116/1.4705375.

[153] S. Keller *et al.*, "InGaN lattice constant engineering via growth on (In,Ga)N/GaN nanostripe arrays," *Semicond. Sci. Technol.*, vol. 30, no. 10, p. 105020, Oct. 2015, doi: 10.1088/0268-1242/30/10/105020.

[154] S. Keller *et al.*, "Optical and structural properties of GaN nanopillar and nanostripe arrays with embedded InGaN⁄GaN multi-quantum wells," *J. Appl. Phys.*, vol. 100, no. 5, p. 054314, Sep. 2006, doi: 10.1063/1.2234812.

[155] T. Ozaki, Y. Takagi, J. Nishinaka, M. Funato, and Y. Kawakami, "Metalorganic vapor phase epitaxy of GaN and lattice-matched InGaN on $ScAlMgO_4$ (0001) substrates," *Appl. Phys. Express*, vol. 7, no. 9, p. 091001, Sep. 2014, doi: 10.7567/APEX.7.091001.

[156] Y. Lei *et al.*, "A GaN-Based LED With Perpendicular Structure Fabricated on a ZnO Substrate by MOCVD," *J. Disp. Technol.*, vol. 9, no. 5, pp. 377–381, May 2013, doi: 10.1109/JDT.2012.2236300.

[157] S.-J. Wang *et al.*, "MOCVD growth of GaN-based materials on ZnO substrates," *Phys. Status Solidi C*, vol. 5, no. 6, pp. 1736–1739, May 2008, doi: 10.1002/pssc.200778614.

[158] A. Kobayashi, J. Ohta, and H. Fujioka, "Low temperature epitaxial growth of In0.25Ga0.75N on lattice-matched ZnO by pulsed laser deposition," *J. Appl. Phys.*, vol. 99, no. 12, p. 123513, Jun. 2006, doi: 10.1063/1.2206883.

[159] Z. Bi *et al.*, "Realization of Ultrahigh Quality InGaN Platelets to be Used as Relaxed Templates for Red Micro-LEDs," *ACS Appl. Mater. Interfaces*, p. acsami.0c00951, Apr. 2020, doi: 10.1021/acsami.0c00951.

[160] A. Tauzin *et al.*, "Transfers of 2-inch GaN films onto sapphire substrates using Smart CutTM technology," *Electron. Lett.*, vol. 41, no. 11, p. 668, 2005, doi: 10.1049/el:20051038.

[161] A. Dussaigne *et al.*, "Full InGaN red (625 nm) micro-LED (10 µm) demonstration on a relaxed pseudo-substrate," *Appl. Phys. Express*, vol. 14, no. 9, p. 092011, Sep. 2021, doi: 10.35848/1882-0786/ac1b3e.

[162] P. Chan *et al.*, "Demonstration of relaxed InGaN-based red LEDs grown with high active region temperature," *Appl. Phys. Express*, Sep. 2021, doi: 10.35848/1882-0786/ac251d.

[163] S. Huang *et al.*, "Mechanical Properties of Nanoporous GaN and Its Application for Separation and Transfer of GaN Thin Films," *ACS Appl. Mater. Interfaces*, vol. 5, no. 21, pp. 11074–11079, Nov. 2013, doi: 10.1021/am4032345.

[164] S. Fakiri, A. Montagne, K. Rahmoun, A. Iost, and K. Ziouche, "Mechanical properties of porous silicon and oxidized porous silicon by nanoindentation technique," *Mater. Sci. Eng. A*, vol. 711, pp. 470–475, Jan. 2018, doi: 10.1016/j.msea.2017.11.013.

[165] C. Wurm *et al.*, "Demonstration of device-quality 60% relaxed $In_{0.2}Ga_{0.8}N$ on porous GaN pseudo-substrates grown by PAMBE," *J. Appl. Phys.*, vol. 131, no. 1, p. 015701, Jan. 2022, doi: 10.1063/5.0075948.

[166] Y. Zhang *et al.*, "A conductivity-based selective etching for next generation GaN devices," *Phys. Status Solidi B*, vol. 247, no. 7, pp. 1713–1716, Jun. 2010, doi: 10.1002/pssb.200983650.

[167] P. H. Griffin and R. A. Oliver, "Porous nitride semiconductors reviewed," *J. Phys. Appl. Phys.*, vol. 53, no. 38, p. 383002, Sep. 2020, doi: 10.1088/1361-6463/ab9570.

[168] P. H. Griffin *et al.*, "The relationship between the three-dimensional structure of porous GaN distributed Bragg reflectors and their birefringence," *J. Appl. Phys.*, vol. 127, no. 19, p. 193101, May 2020, doi: 10.1063/5.0005770.

[169] F. C.-P. Massabuau *et al.*, "Dislocations as channels for the fabrication of sub-surface porous GaN by electrochemical etching," *APL Mater.*, vol. 8, no. 3, p. 031115, Mar. 2020, doi: 10.1063/1.5142491.

[170] T. Zhu *et al.*, "Wafer-scale Fabrication of Non-Polar Mesoporous GaN Distributed Bragg Reflectors via Electrochemical Porosification," *Sci. Rep.*, vol. 7, no. 1, p. 45344, May 2017, doi: 10.1038/srep45344.

[171] R. Anderson, D. Cohen, S. Mehari, S. Nakamura, and S. DenBaars, "Electrical injection of a 440nm InGaN laser with lateral confinement by nanoporous-GaN," *Opt. Express*, vol. 27, no. 16, p. 22764, Aug. 2019, doi: 10.1364/OE.27.022764.

[172] D. Chen, H. Xiao, and J. Han, “Nanopores in GaN by electrochemical anodization in hydrofluoric acid: Formation and mechanism,” *J. Appl. Phys.*, vol. 112, no. 6, p. 064303, Sep. 2012, doi: 10.1063/1.4752259.

[173] C. Zhang, G. Yuan, A. Bruch, K. Xiong, H. X. Tang, and J. Han, “Toward Quantitative Electrochemical Nanomachining of III-Nitrides,” *J. Electrochem. Soc.*, p. 9, 2018.

[174] C. Youtsey, I. Adesida, and G. Bulman, “Highly anisotropic photoenhanced wet etching of n-type GaN,” p. 4.

[175] W. J. Tseng, D. H. van Dorp, R. R. Lieten, P. M. Vereecken, and G. Borghs, “Anodic Etching of n-GaN Epilayer into Porous GaN and Its Photoelectrochemical Properties,” *J Phys Chem C*, p. 7, 2014.

[176] C. B. Soh *et al.*, “Nanopore morphology in porous GaN template and its effect on the LEDs emission,” *Appl Phys*, p. 9, 2013.

[177] R. Nowak *et al.*, “Elastic and plastic properties of GaN determined by nano-indentation of bulk crystal,” *Appl. Phys. Lett.*, vol. 75, no. 14, pp. 2070–2072, Oct. 1999, doi: 10.1063/1.124919.

[178] S. S. Pasayat *et al.*, “Color-tunable < 10 μ m square InGaN micro-LEDs on compliant GaN-on-porous-GaN pseudo-substrates,” *Appl. Phys. Lett.*, vol. 117, no. 6, p. 061105, Aug. 2020, doi: 10.1063/5.0011203.

[179] S. S. Pasayat *et al.*, “Demonstration of ultra-small (<10 μ m) 632 nm red InGaN micro-LEDs with useful on-wafer external quantum efficiency (>0.2%) for mini-displays,” *Appl. Phys. Express*, vol. 14, no. 1, p. 011004, Jan. 2021, doi: 10.35848/1882-0786/abd06f.

[180] S. S. Pasayat *et al.*, “Growth of strain-relaxed InGaN on micrometer-sized patterned compliant GaN pseudo-substrates,” *Appl. Phys. Lett.*, vol. 116, no. 11, p. 111101, Mar. 2020, doi: 10.1063/5.0001480.

[181] S. Keller, S. S. Pasayat, C. Gupta, S. P. DenBaars, S. Nakamura, and U. K. Mishra, “Patterned III-nitrides on porous GaN: extending elastic relaxation from the nano- to the micron-scale,” *Phys. Status Solidi RRL – Rapid Res. Lett.*, p. pssr.202100234, Jul. 2021, doi: 10.1002/pssr.202100234.

[182] E. C. Young *et al.*, “Ultraviolet light emitting diodes by ammonia molecular beam epitaxy on metamorphic (20 2 ¯ 1) AlGaN/GaN buffer layers,” *J. Cryst. Growth*, vol. 425, pp. 389–392, Sep. 2015, doi: 10.1016/j.jcrysgro.2015.02.081.

[183] H. Kroemer, “Speculations about future directions,” *J. Cryst. Growth*, p. 6, 2003.

[184] J. Wang *et al.*, “Hybrid III-Nitride Tunnel Junctions for Low Excess Voltage Blue LEDs and UVC LEDs,” in *2019 Compound Semiconductor Week (CSW)*, Nara, Japan, May 2019, pp. 1–1. doi: 10.1109/ICIPRM.2019.8819252.

[185] C. Lund *et al.*, “Digital growth of thick N-polar InGaN films on relaxed InGaN pseudosubstrates,” *Appl. Phys. Express*, vol. 10, no. 11, p. 111001, Nov. 2017, doi: 10.7567/APEX.10.111001.

[186] S. Pereira *et al.*, “Strain and composition distributions in wurtzite InGaN/GaN layers extracted from x-ray reciprocal space mapping,” *Appl. Phys. Lett.*, vol. 80, no. 21, pp. 3913–3915, May 2002, doi: 10.1063/1.1481786.

[187] S. S. Pasayat *et al.*, “Fabrication of relaxed InGaN pseudo-substrates composed of micron-sized pattern arrays with high fill factors using porous GaN,” *Semicond. Sci. Technol.*, vol. 34, no. 11, p. 115020, Nov. 2019, doi: 10.1088/1361-6641/ab4372.

[188] K. Hestroffer *et al.*, “Relaxed *c* -plane InGaN layers for the growth of strain-reduced InGaN quantum wells,” *Semicond. Sci. Technol.*, vol. 30, no. 10, p. 105015, Oct. 2015, doi: 10.1088/0268-1242/30/10/105015.

[189] Romanczyk, Brian, “Insight into the Design, Fabrication, and mm-Wave Power Performance of N-polar GaN Deep Recess HEMTs,” Thesis, UCSB.

[190] M. Siekacz *et al.*, “Growth of InGaN and InGaN/InGaN quantum wells by plasma-assisted molecular beam epitaxy,” *J. Cryst. Growth*, vol. 310, no. 17, pp. 3983–3986, Aug. 2008, doi: 10.1016/j.jcrysgro.2008.06.011.

[191] Z. Bi, Z. Chen, F. Danesh, and L. Samuelson, “From nanoLEDs to the realization of RGB-emitting microLEDs,” in *Semiconductors and Semimetals*, vol. 106, Elsevier, 2021, pp. 223–251. doi: 10.1016/bs.semsem.2021.01.001.

[192] YouTube. *Plessey microLED GaN-on-Silicon Monolithic 0.7" FHD Bonded Display*, (Jun. 2019). [Online Video]. Available: https://www.youtube.com/watch?v=4PqMQobkUhg

[193] Plessey, “microLED display developer to work with Facebook,” Mar. 30, 2020. http://plesseysemiconductors.com/microled-display-developer-to-work-with-facebook/

[194] V. W. Lee, N. Twu, and I. Kymissis, “Micro-LED Technologies and Applications,” *Inf. Disp.*, vol. 32, no. 6, pp. 16–23, Nov. 2016, doi: 10.1002/j.2637-496X.2016.tb00949.x.

[195] Porotech, “Revolutionary approach for GaN-based RGB MicroLED displays,” 2022. porotech.com

[196] Riber, “MBE 6000 – MULTI 3’’, 4’’, 6’’, 200MM PRODUCTION SYSTEM.” https://www.riber.com/product/mbe-6000/

[197] VEECO, “GEN2000 MBE System.” https://www.veeco.com/products/gen2000-mbe-system/

[198] B. McSkimming, “High Active Nitrogen Flux Growth of (Indium) Gallium Nitride by Plasma Assisted Molecular Beam Epitaxy,” Thesis, UCSB, 2015.

[199] S. S. Pasayat *et al.*, “Method of growing elastically relaxed crack-free AlGaN on GaN as substrates for ultra-wide bandgap devices using porous GaN,” *Appl. Phys. Lett.*, vol. 117, no. 6, p. 062102, Aug. 2020, doi: 10.1063/5.0017948.

[200] K. Lee, Y. Cho, L. J. Schowalter, M. Toita, H. G. Xing, and D. Jena, “Surface control and MBE growth diagram for homoepitaxy on single-crystal AlN substrates,” *Appl. Phys. Lett.*, vol. 116, no. 26, p. 262102, Jun. 2020, doi: 10.1063/5.0010813.

[201] G. Namkoong, E. Trybus, K. K. Lee, M. Moseley, W. A. Doolittle, and D. C. Look, “Metal modulation epitaxy growth for extremely high hole concentrations above 1019cm−3 in GaN,” *Appl. Phys. Lett.*, vol. 93, no. 17, p. 172112, Oct. 2008, doi: 10.1063/1.3005640.